

AD-R163 332

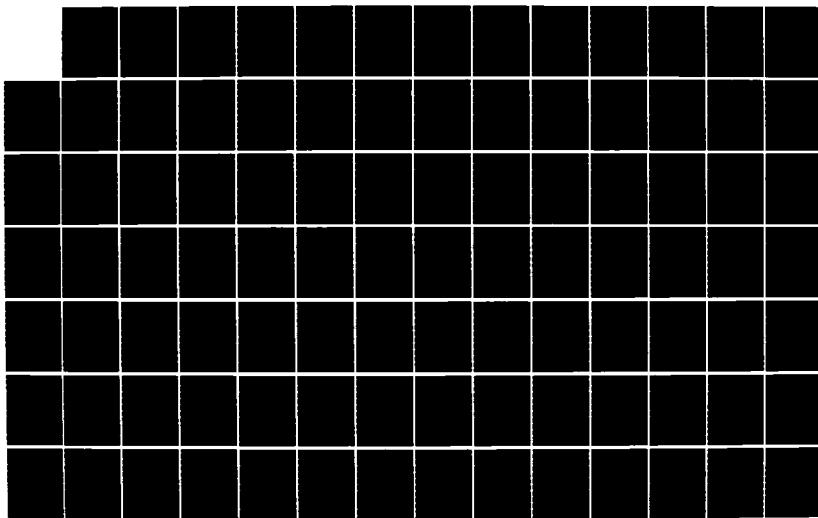
APPLICATION OF FLUX-CORRECTED TRANSPORT TO TTCP JOINT  
LAUNCH BLAST COMPUTATIONAL EFFORT(U) NAVAL RESEARCH LAB  
WASHINGTON DC P S KAMATH ET AL. 31 DEC 85 NRL-MR-5781

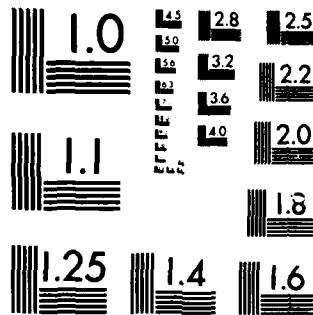
1/2

UNCLASSIFIED

F/G 19/4

NL





MICROCOPY RESOLUTION TEST CHART  
NATIONAL BUREAU OF STANDARDS-1963-A

(2)

NRL Memorandum Report 5701

## Application of Flux-Corrected Transport to TTCP Joint Launch Blast Computational Effort

AD-A163 332

P. S. KAMATH, S. EIDELMAN AND M. A. FRY

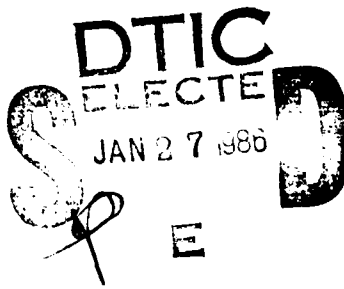
*Science Applications International Corporation  
McLean, VA 22102*

J. D. BAUM AND D. L. BOOK

*Laboratory for Computational Physics*

December 31, 1985

FILE COPY



NAVAL RESEARCH LABORATORY  
Washington, D.C.

Approved for public release; distribution unlimited.

1D A163 332

## REPORT DOCUMENTATION PAGE

1a. REPORT SECURITY CLASSIFICATION UNCLASSIFIED		1b. RESTRICTIVE MARKINGS			
2a. SECURITY CLASSIFICATION AUTHORITY		3. DISTRIBUTION/AVAILABILITY OF REPORT			
2b. DECLASSIFICATION/DOWNGRADING SCHEDULE		Approved for public release; distribution unlimited.			
4. PERFORMING ORGANIZATION REPORT NUMBER(S) NRL Memorandum Report 5701		5. MONITORING ORGANIZATION REPORT NUMBER(S)			
6a. NAME OF PERFORMING ORGANIZATION Naval Research Laboratory	6b. OFFICE SYMBOL (if applicable) Code 4040	7a. NAME OF MONITORING ORGANIZATION Office of Naval Research			
6c. ADDRESS (City, State, and ZIP Code) Washington, DC 20375-5000		7b. ADDRESS (City, State, and ZIP Code) Arlington, VA 22217			
8a. NAME OF FUNDING/SPONSORING ORGANIZATION Office of Naval Research	8b. OFFICE SYMBOL (if applicable)	9. PROCUREMENT INSTRUMENT IDENTIFICATION NUMBER			
8c. ADDRESS (City, State, and ZIP Code) Arlington, VA 22217		10. SOURCE OF FUNDING NUMBERS			
		PROGRAM ELEMENT NO. 61153N	PROJECT NO.	TASK NO. RR011- 09-43	WORK UNIT ACCESSION NO. DN280-069
11. TITLE (Include Security Classification) Application of Flux-Corrected Transport to TTCP Joint Launch Blast Computational Effort					
12. PERSONAL AUTHOR(S) Kamath, P.S., * Eidelman, S., * Fry, M.A., * Baum, J.D. and Book, D.L.					
13a. TYPE OF REPORT Interim	13b. TIME COVERED FROM _____ TO _____	14. DATE OF REPORT (Year, Month, Day) 1985 December 31		15. PAGE COUNT 136	
16. SUPPLEMENTARY NOTATION *Science Applications International Corporation, McLean, VA 22102					
17. COSATI CODES	18. SUBJECT TERMS (Continue on reverse if necessary and identify by block number) Muzzle blast, Shock waves Launch blast, Flux-corrected transport				
19. ABSTRACT (Continue on reverse if necessary and identify by block number) A general-purpose Flux-Corrected Transport (FCT) hydrocode has been used to treat two muzzle blast test problems. Analysis of the results and comparison with data indicates that the results are physically realistic and, within the modeling assumptions, highly accurate. The FCT simulation model used runs on the Cray-1 and on smaller mainframe computers including the VAX and the multitasking array processors in our Graphical and Array Processing System. ✓					
20. DISTRIBUTION/AVAILABILITY OF ABSTRACT <input checked="" type="checkbox"/> UNCLASSIFIED/UNLIMITED <input type="checkbox"/> SAME AS RPT. <input type="checkbox"/> DTIC USERS		21. ABSTRACT SECURITY CLASSIFICATION UNCLASSIFIED			
22a. NAME OF RESPONSIBLE INDIVIDUAL David L. Book		22b. TELEPHONE (Include Area Code) (202) 767-2078	22c. OFFICE SYMBOL Code 4040		

## CONTENTS

INTRODUCTION .....	1
RESULTS .....	4
CONCLUSION .....	9
REFERENCES .....	132

Accession For	
NTIS GRA&I	<input checked="" type="checkbox"/>
DTIC TAB	<input type="checkbox"/>
Unannounced	<input type="checkbox"/>
Justification	
By _____	
Distribution/ _____	
Availability Codes	
Dist	Avail and/or Special
A-1	



## APPLICATION OF FLUX-CORRECTED TRANSPORT TO TTCP JOINT LAUNCH BLAST COMPUTATIONAL EFFORT

### INTRODUCTION

The method of Flux-Corrected Transport (FCT) was developed about ten years ago (Boris and Book, 1973; Book et al., 1975; Boris and Book, 1976) as a means for solving systems of hyperbolic equations in such a way that physically positive quantities like mass and energy density remain positive. Its principal application has been to compressible fluids, i.e., fluids in which some of the flow speeds are comparable with or greater than the local speed of propagation of waves in the medium. Examples include plasmas, combusting systems, and gas-dynamic flows. Applications of FCT to muzzle blast problems were first made by Townend and Edwards (1982).

During the past decade the method has been extended and generalized in a number of important respects. These include the construction of general-purpose algorithms for solving fluid equations on moving nonuniform grids in a curvilinear coordinate system (Boris 1976), strictly multidimensional FCT algorithms (as opposed to timestep-splitting of one-dimensional algorithms, Zalesak 1979), and variants on these. In addition, numerous techniques have been developed by other workers which incorporate the positivity-preserving property in other ways (Harten, 1978; Van Leer, 1979; Collela and Woodward, 1984). The weight of opinion among computational scientists who deal with problems of compressible flow now strongly affirms the superiority of positivity-preserving methods (e.g., Total Variation Diminishing or TVD) over conventional ones. The advantages are improved robustness, flexibility, resolution, and freedom from nonphysical numerical artifacts.

Manuscript approved October 9, 1985.

FAST2D (Boris 1976) is an FCT code for solving the two-dimensional fluid equations in Cartesian or r-z geometry. It employs timestep-splitting to permit the use of JPBFC, a general-purpose one-dimensional convective equation solver for both coordinate sweeps in all of the fluid equations.

To explain what this means, let us describe a class of FCT algorithms which includes JPBFC as a particular case. To advance the one-dimensional continuity equation

$$\frac{\partial \rho}{\partial t} = - \frac{\partial}{\partial x} (\rho v) \quad (1)$$

one timestep on a uniform mesh with a given flow velocity  $v$ , we suppose the old cell-centered values  $\rho_j^0$  and  $v_j$  are known. A three-point conservative finite-difference operator acting on  $\rho_j^0$  can be written in the form

$$\rho_j^T = \rho_j^0 - \epsilon_{j+1/2} \rho_{j+1/2} + \epsilon_{j-1/2} \rho_{j-1/2}, \quad (2)$$

where  $\rho_{j+1/2} = \frac{1}{2} (\rho_j + \rho_{j+1})$ . To obtain a first-order approximation to Eq. (1), we must define  $\epsilon_{j+1/2}$  to be the Courant number  $v_{j+1/2} \delta t / \delta x$ , where  $v_{j+1/2} = \frac{1}{2} (v_j + v_{j+1})$ . In FCT a numerical diffusion is then applied to  $\rho_j^T$  in flux form according to

$$\rho_j^{TD} = \rho_j^T + v_{j+1/2} (\rho_{j+1}^0 - \rho_j^0) - v_{j-1/2} (\rho_j^0 - \rho_{j-1}^0). \quad (3)$$

Next we act to eliminate this excess diffusion. If we simply applied another diffusion operation, this time with the opposite sign, it would cancel the diffusion terms already present in  $\rho_j^{TD}$ . Instead we define new densities  $\rho_j^n$

$$\rho_j^n = \rho_j^{TD} - \phi_{j+1/2}^c + \phi_{j-1/2}^c, \quad (4)$$

where the "corrected" fluxes  $\phi_{j+1/2}^c$  differ from the "raw" fluxes  $\phi_{j+1/2} = \mu_{j+1/2} (\rho_{j+1}^o - \rho_j^o)$  in two ways: we use  $\{\rho_j^T\}$  instead of  $\{\rho_j^o\}$  in the definition of the raw fluxes (this allows us to optimize some property in the difference scheme, as will be seen shortly); and we correct the fluxes, so that the antidiiffusion process (which evidently tends to make all gradients steeper) can enhance no extrema already present in  $\{\rho_j^T\}$ , nor introduce any new ones. The simplest formula for achieving this in all possible situations is that used in "strong flux limiting":

$$\phi_{j+1/2}^c = S \cdot \{ \max[0, \min(|\phi_{j+1/2}|, \Delta_{j-1/2}, \Delta_{j+3/2})] \} , \quad (5)$$

where  $S = \text{sign } \phi_{j+1/2}$  and  $\Delta_{j+1/2} = \rho_{j+1}^T - \rho_j^T$ .

At most points in a gently varying profile no correction is required and  $\phi_{j+1/2}^c = \phi_{j+1/2}$ . In that case we can perform a Von Neumann analysis, calculating the complex propagator or amplification factor  $A = A_r + iA_i = \rho_j^n / \rho_j^o$  for a sinusoidal density profile  $\rho_j^o = \exp(ik\delta x)$ , where  $k$  is the wave number. Writing  $\beta = k\delta x$  and  $\epsilon = v\delta t / \delta x$ , we expand the amplification in powers of  $\beta$

$$A = 1 + A_2 \beta^2 + A_4 \beta^4 + \dots \quad (6)$$

and the relative phase error

$$R = \frac{1}{\beta\epsilon} \tan^{-1} (A_i/A_r) - 1 = R_2 \beta^2 + R_4 \beta^4 + \dots \quad (7)$$

It is easy to show that the condition that  $A_2$  vanish is

$$v - \mu = \frac{1}{2} \epsilon^2 . \quad (8)$$

The condition that  $R_2$  vanish is

$$\mu = \frac{1}{6} - \frac{1}{6} \epsilon^2 . \quad (9)$$

While other choices of  $\nu$  and  $\mu$  are possible, Eqs. (8) and (9) lead to the most useful general-purpose algorithm within this class and have been used in a wide variety of supersonic flow problems. Besides producing small phase and amplitude errors, as shown above, this choice of the diffusion and antidiiffusion coefficients  $\nu$  and  $\mu$  treats shocks very accurately, unlike schemes where  $\nu$  and  $\mu$  are small.

Generalizing this scheme to handle the momentum and energy equations presents no problem as the treatment of the driving terms  $-\nabla p$ , etc., and  $-\nabla \cdot p v$  is not very sensitive. Extension to nonuniform meshes and curvilinear geometry is also straightforward. When fully vectorized and optimized for a particular machine (in the present case, the Cray-1) it runs at about 2  $\mu$ s per zone per timestep per equation per coordinate direction.

## RESULTS

### Case I: Flow From the Open End of a Shock Tube

Figure 1 reproduces the BRL drawings defining the geometry of the shock tube and prescribing the computational domain to be used (Schmidt, 1985). Although it would be of interest to model the entire length of the shock tube (including the 0.673 m driver section and the whole 3.044 m driven section), this would necessitate a calculation with a computational region approximately ten times as long as that specified for the case. In our calculation we used a grid with 200 zones in the radial and 400 zones in the axial direction, with mesh sizes  $\Delta r = \Delta z = 0.228$  cm. Although temperature and density do not deviate too widely from standard conditions and  $\gamma = 1.4$

holds approximately, we used a real-air equation of state. Reflecting boundary conditions were employed at  $r = 0$ , and outflow conditions (valid for supersonic flow) at maximum radial and axial displacement. The conditions at  $z = 0$  were maintained at their initial values, which is valid until disturbances propagating out of the driver region reach the computational domain.

Timesteps were limited to 0.5 times the value imposed by the Courant condition and averaged about a microsecond. The calculation ran 1618 cycles, with dumps being obtained at times  $t = 0.025, 0.05, 0.1, 0.2, 0.5, 1.0$  and  $1.5 \text{ ms}$ . Using these dumps we generated velocity vector plots and contours of constant density, pressure, and Mach number. In addition, time histories of pressure, density, and Mach number were generated at stations situated at a distance of 1.5 times the tube diameter  $D = 0.152 \text{ m}$  from the center of the tube exit along the  $0, 30, 60, 90, 120, 130$ , and  $138.2$  degree rays. These locations are indicated by the dots in Fig. 1c. Since the station along the  $0^\circ$  ray was of particular interest in connection with determining the location of the backward-facing shock, ten additional stations were located in the neighborhood of the station along this ray.

Figures 2-8 show the overall flow at the plotting times specified above. In each figure we have four plots: contours of (a) pressure, (b) density, and (c) Mach number; and (d) velocity vector plots. Note that by  $0.5 \text{ ms}$  (Fig. 6) several well-defined gasdynamic discontinuities have developed. These include a disk-shaped backward-facing shock which terminates at its outer radius in a compression fan. The latter is rolled up into a vortex ring. At a radius of approximately  $0.05 \text{ m}$  a cylindrical slip surface (which shows up as a discontinuity in density but not pressure) intersects this shock, producing a kink. By  $1.5 \text{ ms}$  (Fig. 8), when the primary shock has

reached the end of the mesh, the vortex ring has expanded out to about 0.1 m in radius.

Figures 9 - 16 are station plots, each showing (a) overpressure, (b) density, and (c) Mach number at the prescribed locations. The flow behind the shock is of course subsonic everywhere. All stations show a pressure (and density) peak at shock arrival time, followed by a rarefaction wave. The stations located off the center line (all except no. 1) reach pressures less than ambient. Comparison with digitized traces of pressure measurements (Figs. 17 - 33) shows good agreement between calculated and recorded values except at station no. 1. There the calculated values (labelled with "A") are close to the measured ones (labelled with "B") until about 1 ms. Thereafter the latter peak up above the calculation by about 20 kPa and then drop below by about 60 kPa. We attribute this discrepancy to slight errors in defining the location of the backward-facing shock, probably caused by an increase in the effective flow velocity from the opening of the shock tube as a result of the formation of a boundary layer there. Rather than try to model this boundary layer, we introduced ten additional stations on the axis between 0.662 m and 0.683 m from the opening. The waveform which agrees best with the observed trace is that calculated at station no. 10 (Fig. 26,  $y = 0.667$  m). Nevertheless, the unsteady behavior of the shock in the experimental setup precludes perfect agreement for these features.

#### Case II: 105 mm Muzzle Flow

In this problem the geometry is complicated by the addition of a baffle located downstream from the muzzle, and by the presence of the projectile at early times. No attempt was made to model the latter (although it is not difficult to do) because it has no influence on the flow near the muzzle

except at very early times. Otherwise the same boundary conditions were used as in Case I.

The zone size was  $\Delta r = \Delta z = 0.3$  cm. For this problem two fluid mass densities were propagated according to the continuity equation, using a single flow velocity field. One fluid, air, initially filled the entire grid outside the muzzle and the solid walls. The other fluid, representing detonation products from the propellant, expands out from the muzzle with the prescribed exit velocity of 1050 m/s. Partial pressures were obtained using respectively a real-air equation of state and a constant-gamma law ( $\gamma = 1.25$ ) for the two fields.

Figures 34 - 38 shows contours of (a) pressure, (b) density, and (c) Mach number, and (d) velocity vector plots at the prescribed times  $t = 0.025$ ,  $0.05$ ,  $0.1$ ,  $0.5$ , and  $1.0$  ms, respectively. Note that by  $0.1$  ms part of the shock wave has reached the baffle and been deflected away. The central portion passes through the hole and begins to diffract around to the back of the baffle. By  $0.5$  ms the shock has left the top of the grid. Thereafter the solution quickly relaxes to a steady state, maintained by the propellant gases emerging from the howitzer muzzle.

Figures 39 - 47 show waveforms of (a) pressure, (b) density, and (c) Mach number at the nine prescribed stations. Stations (1) - (3), located on the front of the baffle, show slightly different peak values at shock arrival time and saturate at slightly different values at late times, reflecting their varying distances from the muzzle. The stations in front of, alongside, and behind the muzzle show variations which can readily be interpreted in terms of geometry. It is seen that although the flow is deflected by the baffle, beyond it (at distances  $\gtrsim D$ ) the baffle has little effect on most features in either contour or station plots.

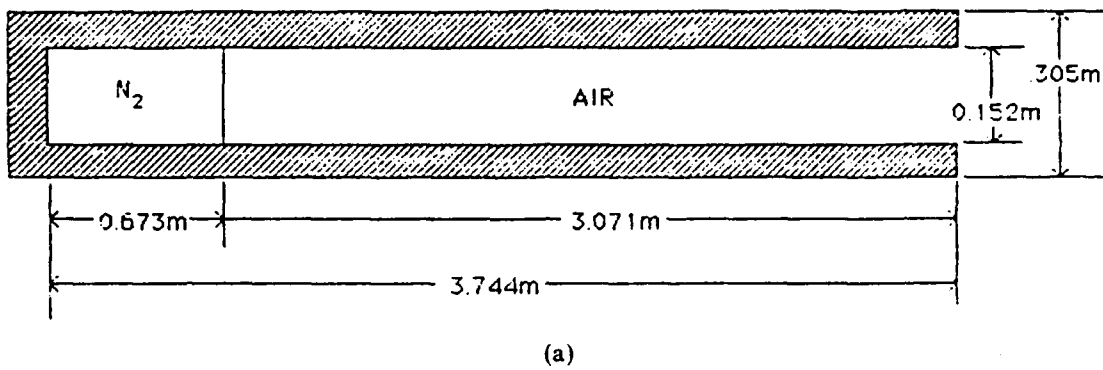
Since the flow is subsonic, the mesh boundaries should permit inflow of the surrounding ambient atmosphere at late times, and this should come to equilibrium with the emerging flow of propellant gases. Because we kept the same outflow boundary conditions as in Case I, inflow cannot take place, and at late times the pressures and densities near the outer boundary become unphysically low. For this reason we have plotted station histories only out to 1 ms.

## CONCLUSION

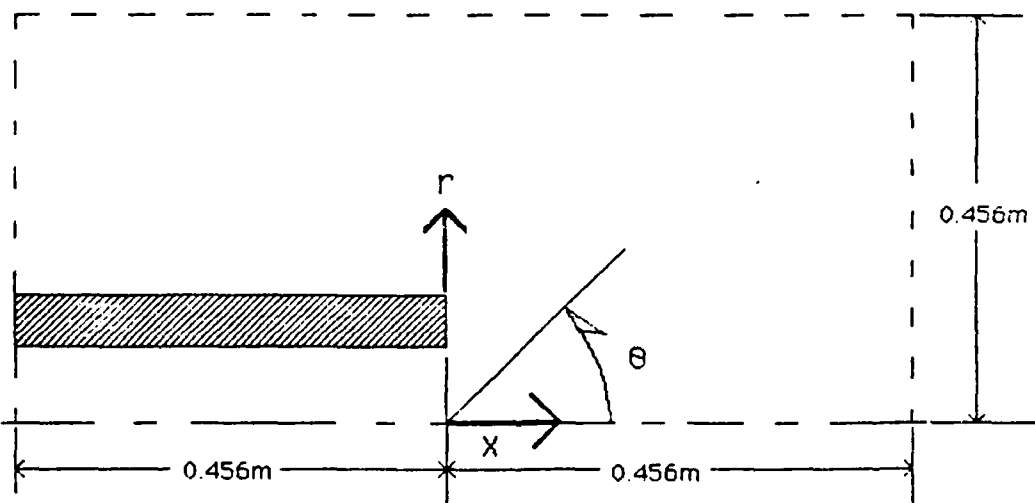
We have carried out two test muzzle blast calculations using the FCT code FAST2D. Numerous simplifications have been introduced to minimize the programming effort required, and considerable improvement could be made in our treatment of (i) viscous boundary layers (in Case I); (ii) inflow and projectile boundary conditions (in Case II); and (iii) the propellant gas equation of state. Nevertheless, the agreement with the data in Case I and the physical plausibility and internal consistency of both cases strongly support the validity of this modeling approach and suggest that FCT hydrocodes can make a valuable contribution to the muzzle blast modeling effort.

Although the calculations described here were carried out on a Cray-1 supercomputer, it is worth noting that the computing requirements for FAST2D are actually very modest. The Laboratory for Computational Physics has assembled a Graphical and Array Processing System (GAPS) consisting of a VAX 11/780, two FPS 5305 array processors working in tandem (up to 10 APs are possible), an Aptec DPS 2400 I/O computer, and a Tektronix 4115B high-speed graphics device. This system is running a comparable two-dimensional hydrocode, programmed entirely in FORTRAN, at speeds of  $\sim 0.2$  ms per mesh point per timestep, in either batch or interactive mode. In the latter it produces color plots of the evolving simulation approximately every 5 seconds with DICOMED hard copy capability. This is about 1/8 the speed of a single processor Cray X-MP. A sample frame from a muzzle blast calculation done using the RFM hydrocode on the GAPS is reproduced as Fig. 48. It is important to stress that such a system is small and can be maintained in a secure self-contained facility, where it can be dedicated entirely to muzzle blast or similar energetic gasdynamic calculations if so desired. The cost of the basic system is  $\sim \$220K$ .

SHOCK TUBE CONFIGURATION:



COMPUTATIONAL DOMAIN:



(b)  
Figure 1

BLAST DIFFRACTION FROM SHOCK TUBE  
TIME= 0.00000E+00 SEC., STEP 1. DUMP TUBB0001 DENSITY 1, KG/M3

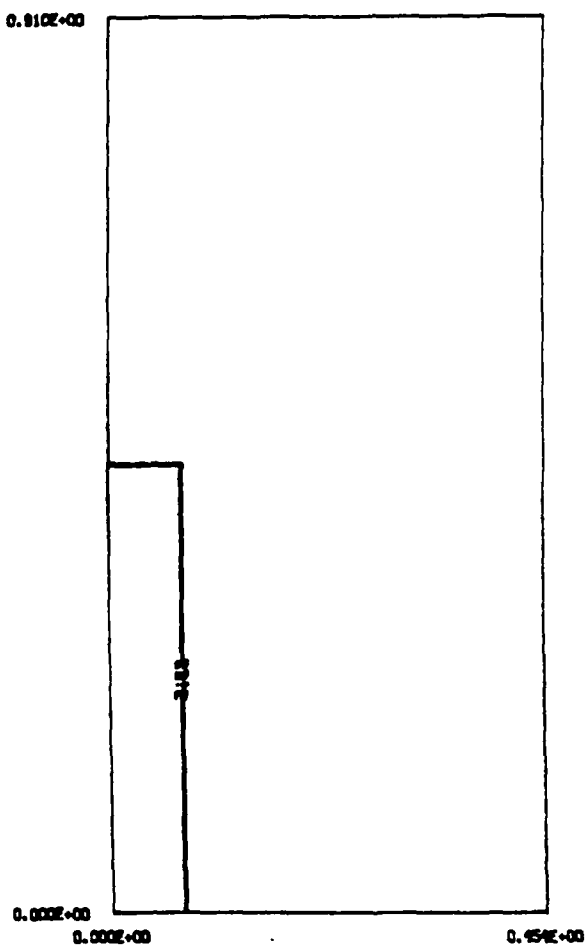


Figure 1b

BLAST DIFFRACTION FROM SHOCK TUBE  
TIME= 0.00000E+00 SEC., STEP 1, DUMP TUBB0001 PRESSURE, NEWTONS/M\*\*2

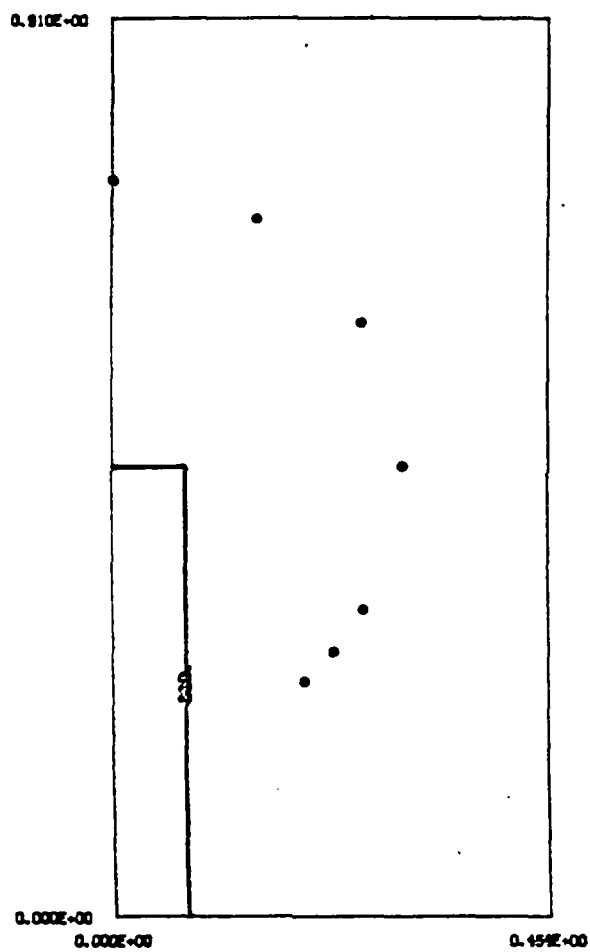


Figure 1c

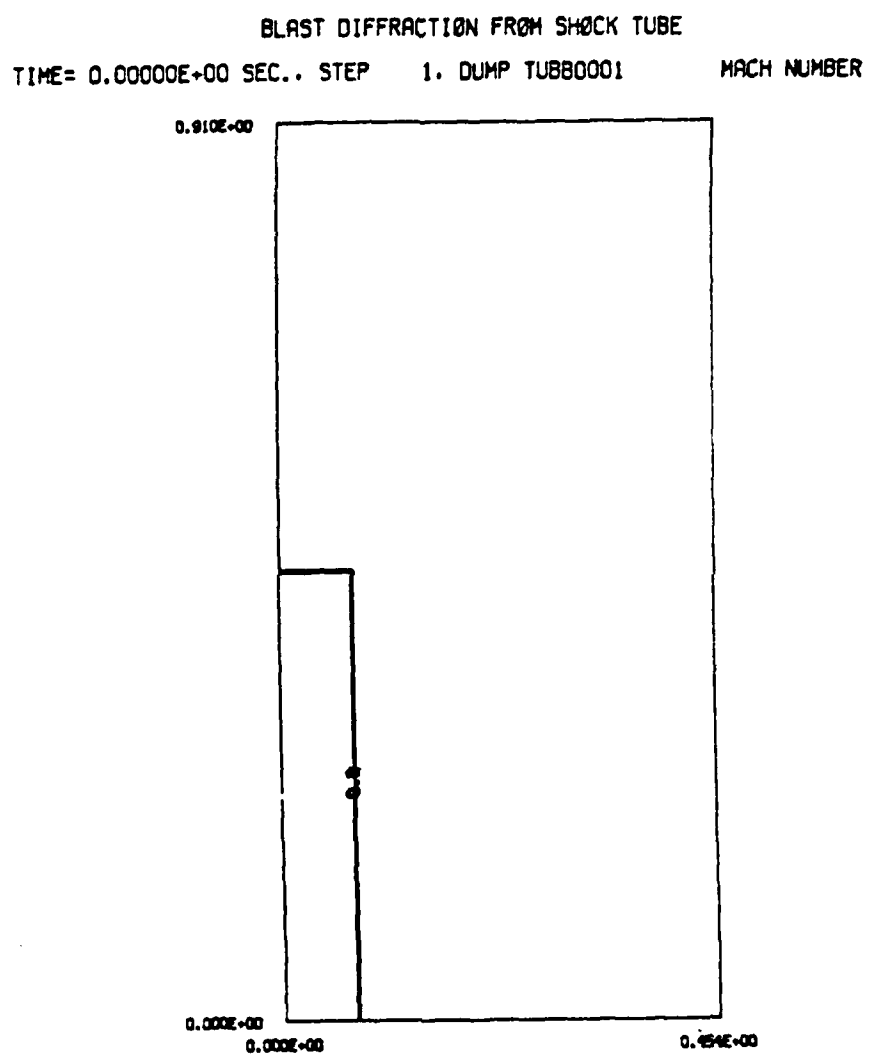


Figure 1c

BLAST DIFFRACTION FROM SHOCK TUBE  
TIME= 0.00000E+00 SEC.. STEP 1. DUMP TUBB0001 VELOCITY. M/SEC

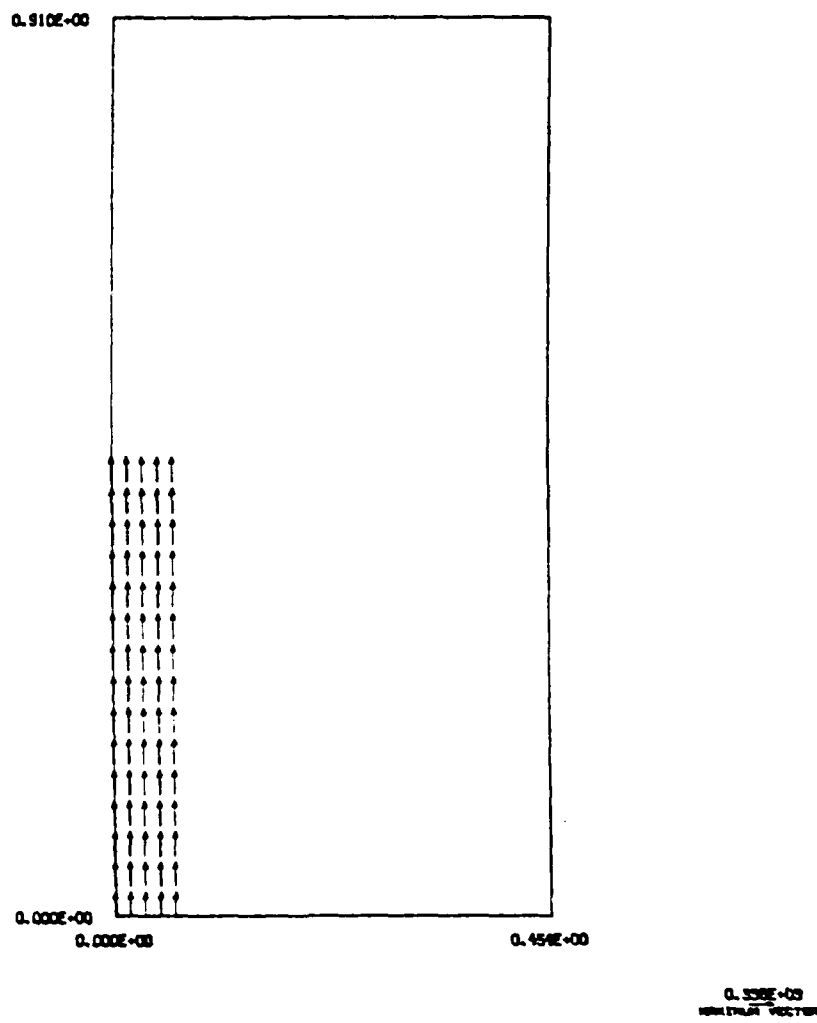


Figure 1d

BLAST DIFFRACTION FROM SHOCK TUBE  
TIME= 0.25649E-04 SEC., STEP 86, DUMP TUBB0002 PRESSURE, NEWTONS/M\*\*2

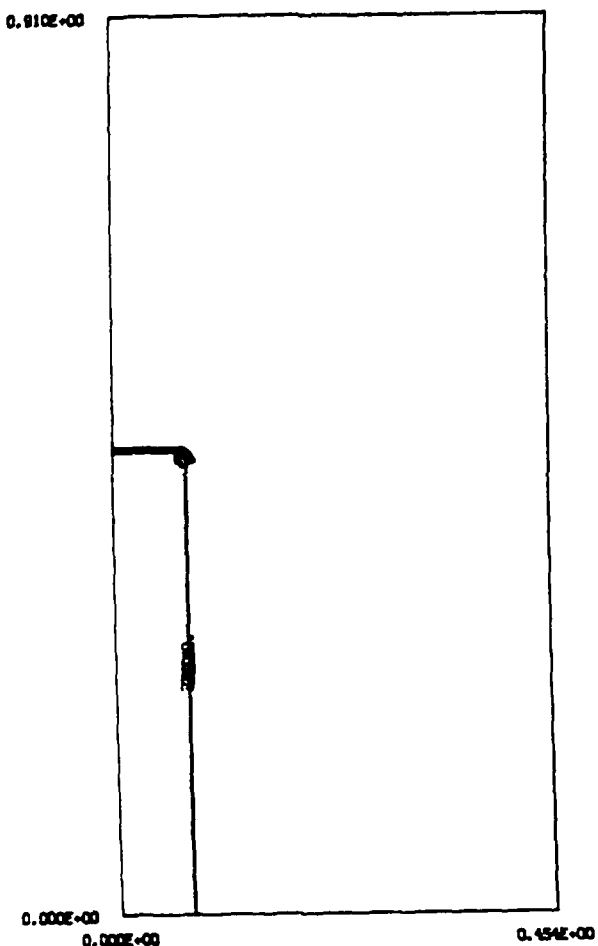


Figure 2a

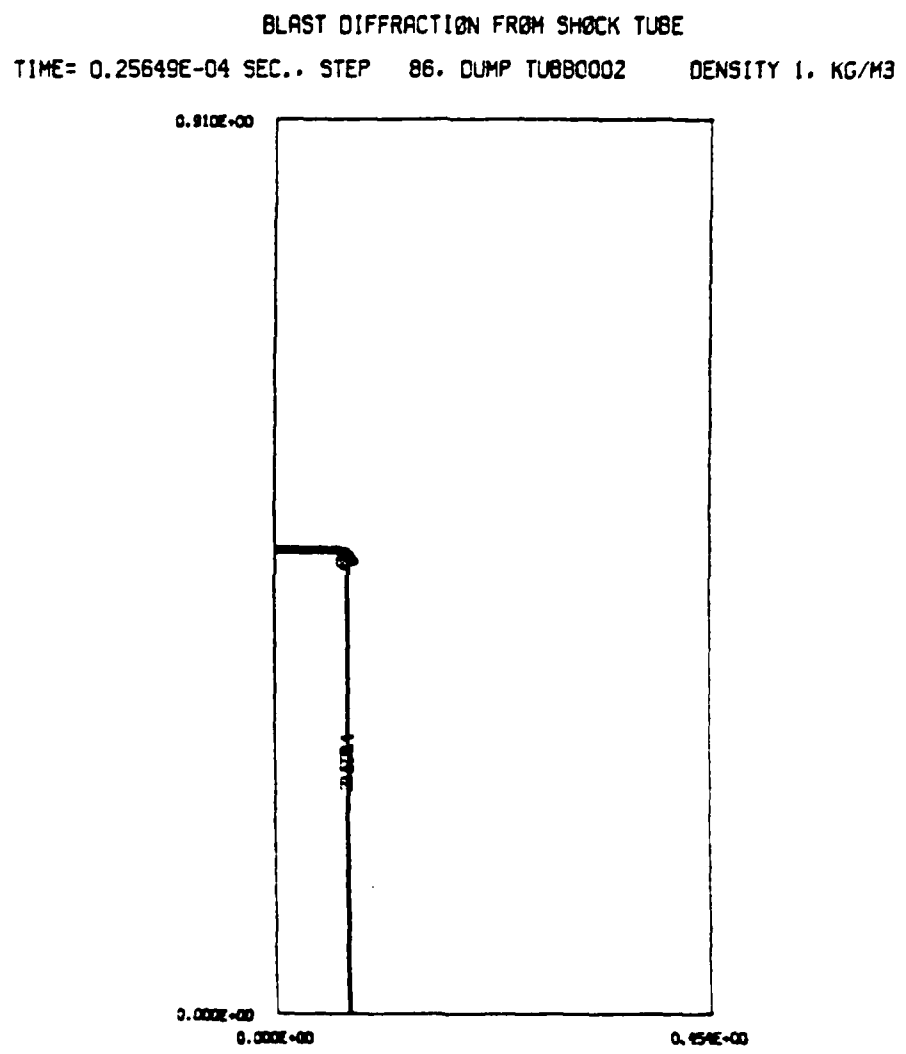


Figure 2b

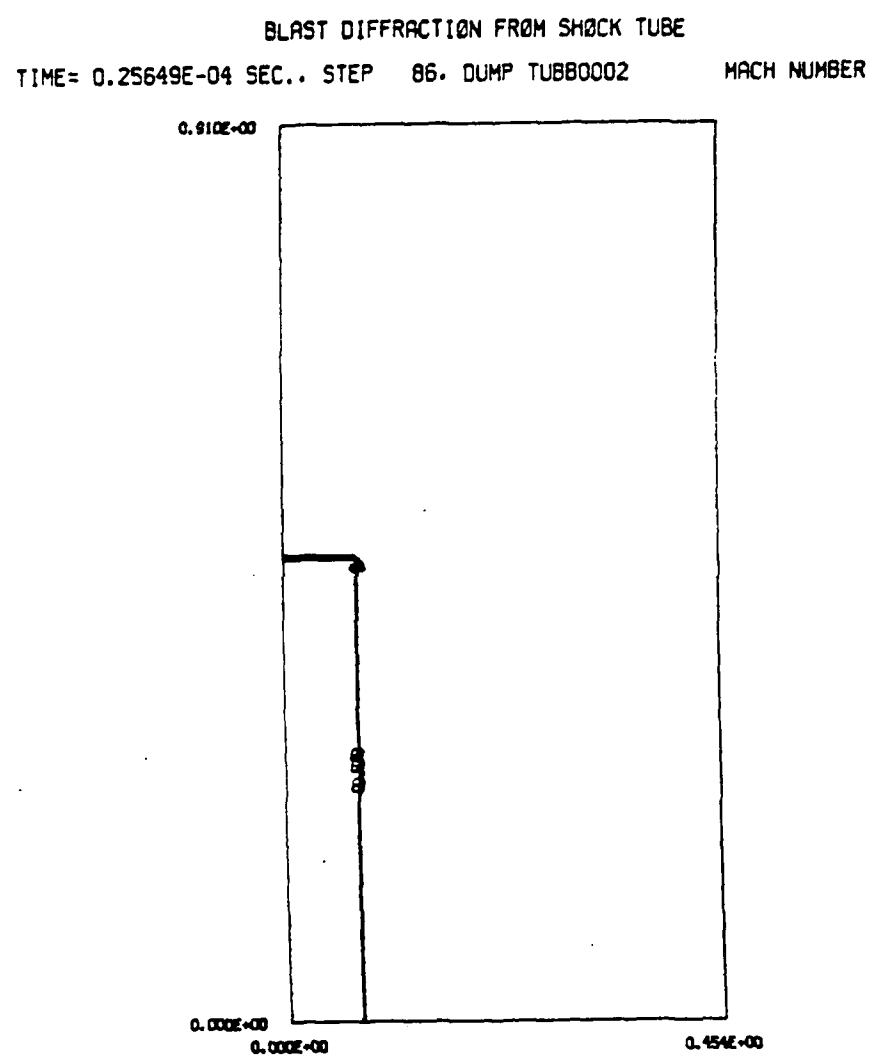
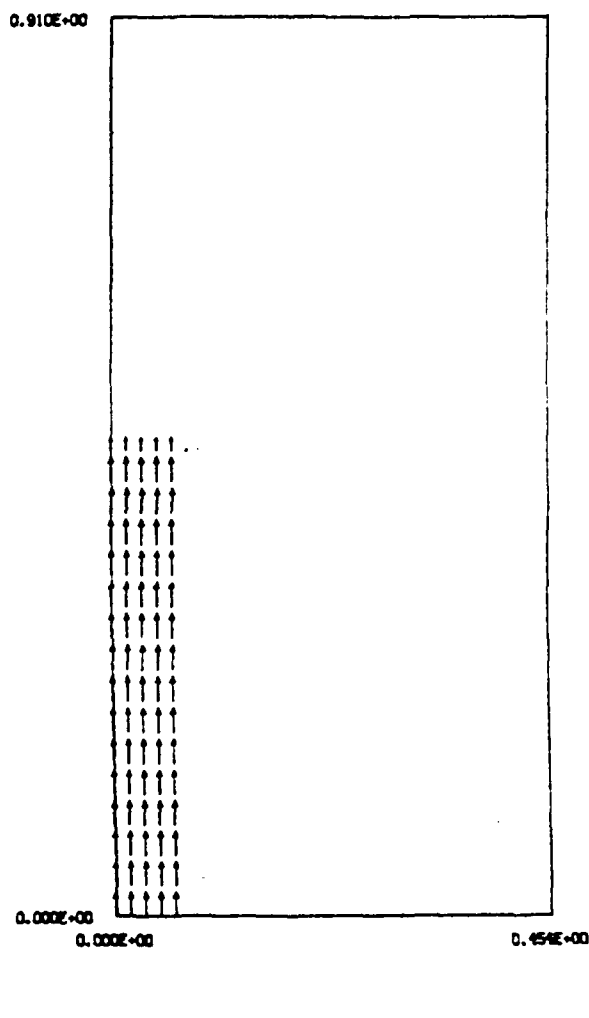


Figure 2c

BLAST DIFFRACTION FROM SHOCK TUBE  
TIME= 0.25649E-04 SEC.. STEP 86. DUMP TUBB0002 VELOCITY. M/SEC



0.359E+03  
NORMAL VELOCITY

Figure 2d

BLAST DIFFRACTION FROM SHOCK TUBE  
TIME= 0.50172E-04 SEC., STEP 107, DUMP TUB80003 PRESSURE, NEWTONS/M<sup>2</sup>

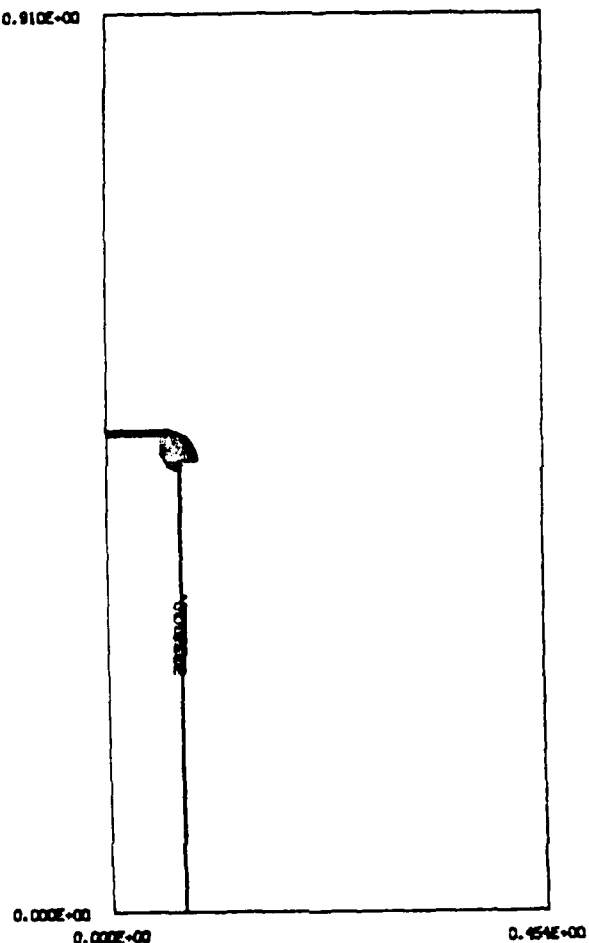


Figure 3a

BLAST DIFFRACTION FROM SHOCK TUBE

TIME= 0.50172E-04 SEC., STEP 107, DUMP TUBB0003 DENSITY 1, KG/M3

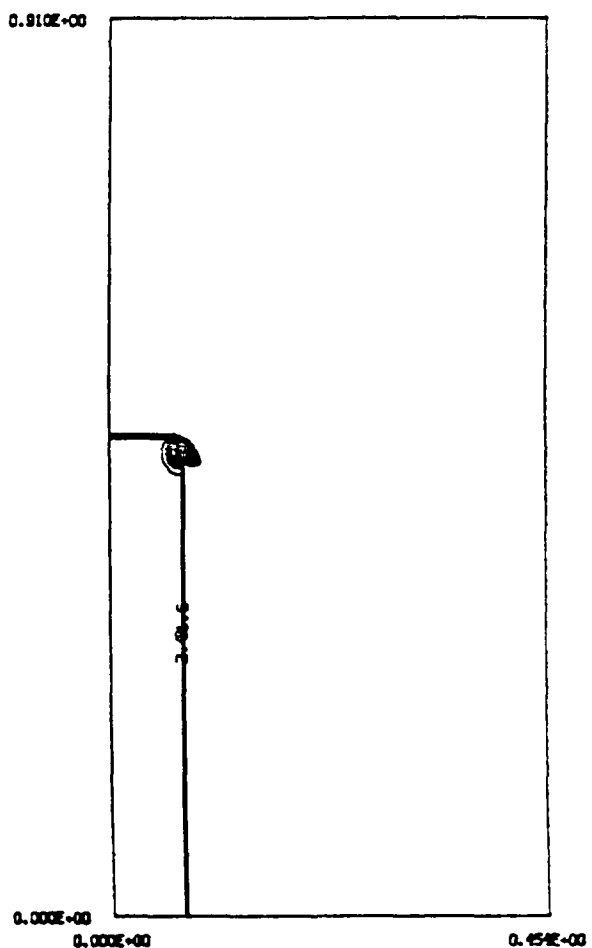


Figure 3b

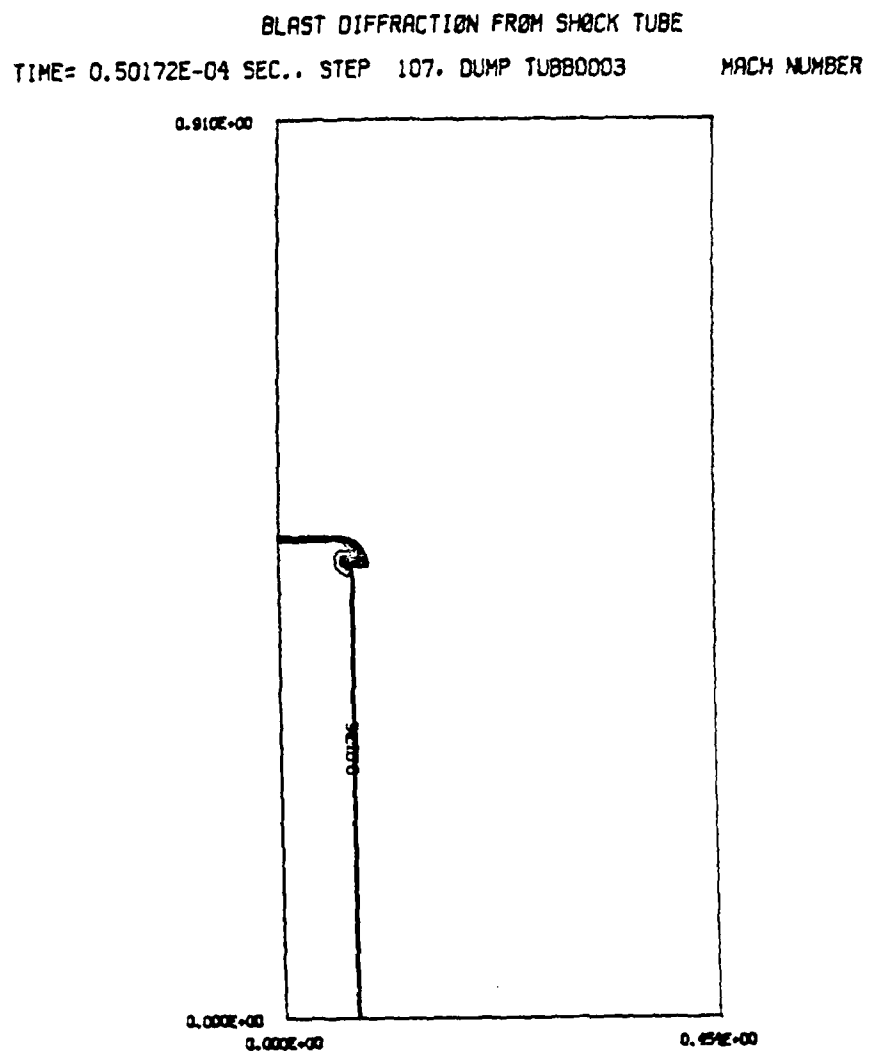


Figure 3c

BLAST DIFFRACTION FROM SHOCK TUBE  
TIME= 0.50172E-04 SEC.. STEP 107. DUMP TUBB0003 VELOCITY. M/SEC

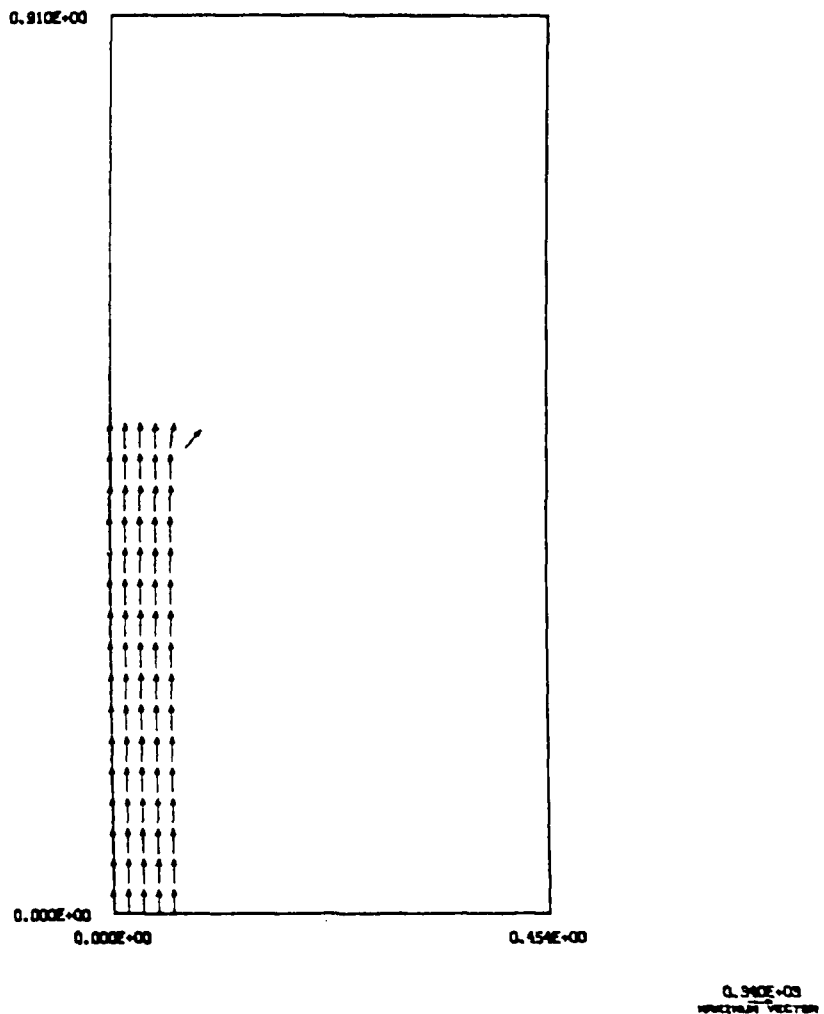


Figure 3d

BLAST DIFFRACTION FROM SHOCK TUBE

TIME= 0.10014E-03 SEC.. STEP 152. DUMP TUBB0004 PRESSURE. NEWTONS/M\*\*2

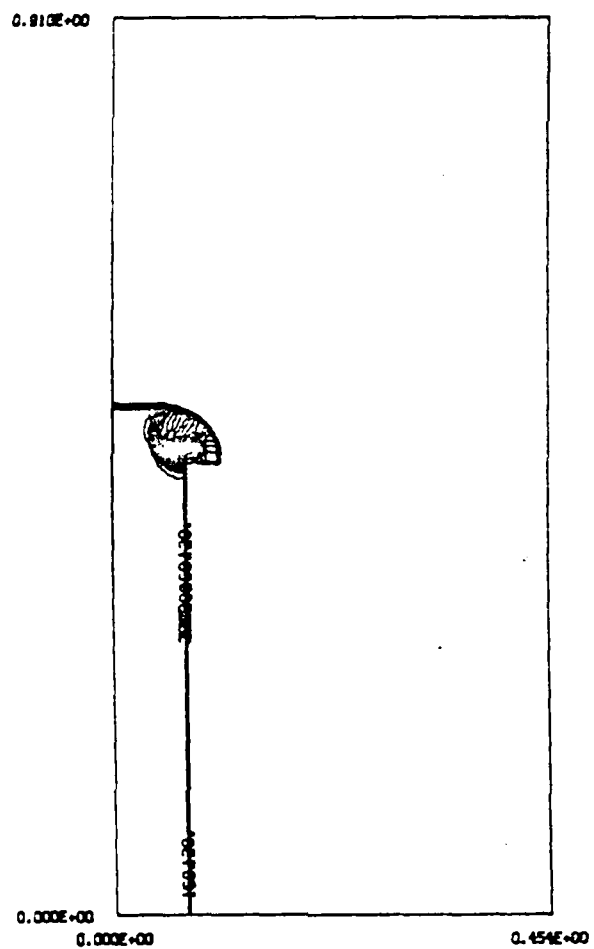


Figure 4a

BLAST DIFFRACTION FROM SHOCK TUBE  
TIME= 0.10014E-03 SEC., STEP 152, DUMP TUBB0004 DENSITY 1. KG/M3

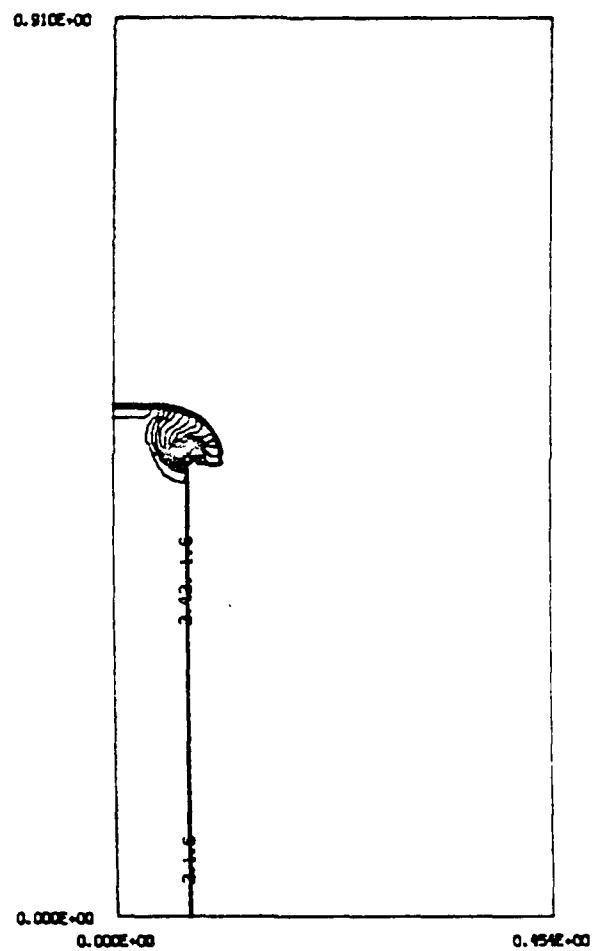


Figure 4b

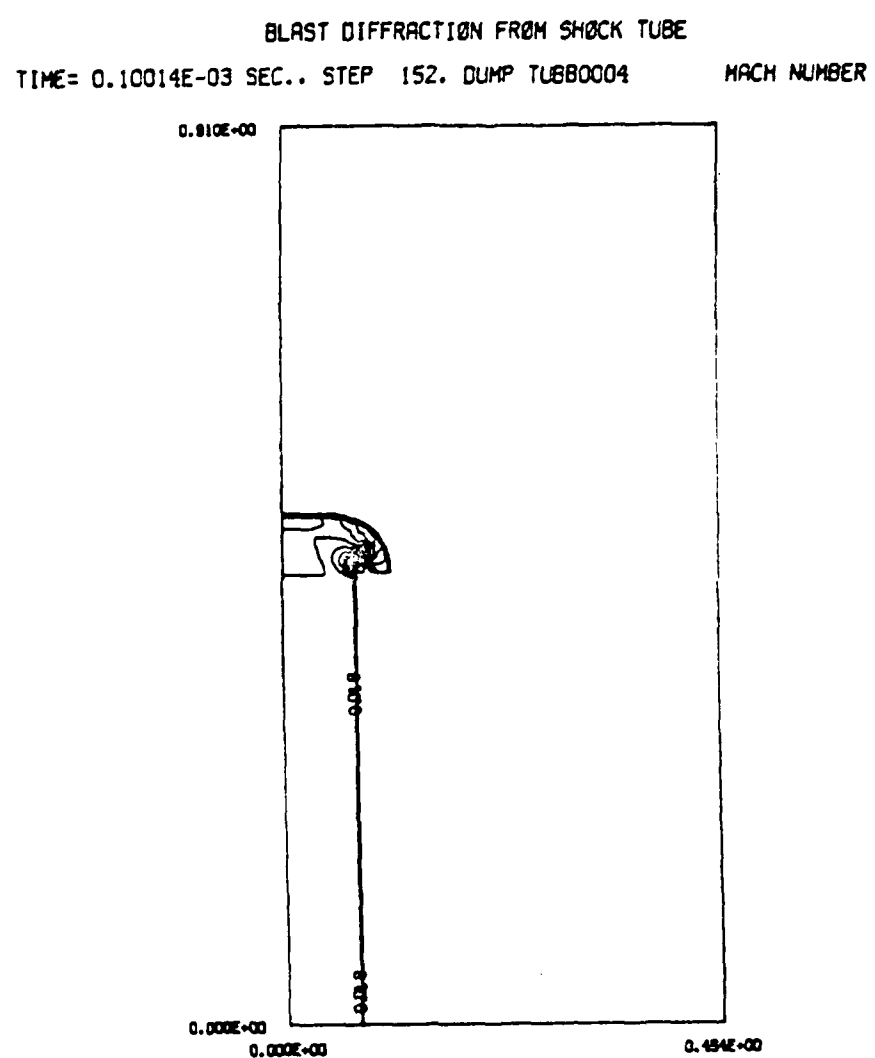
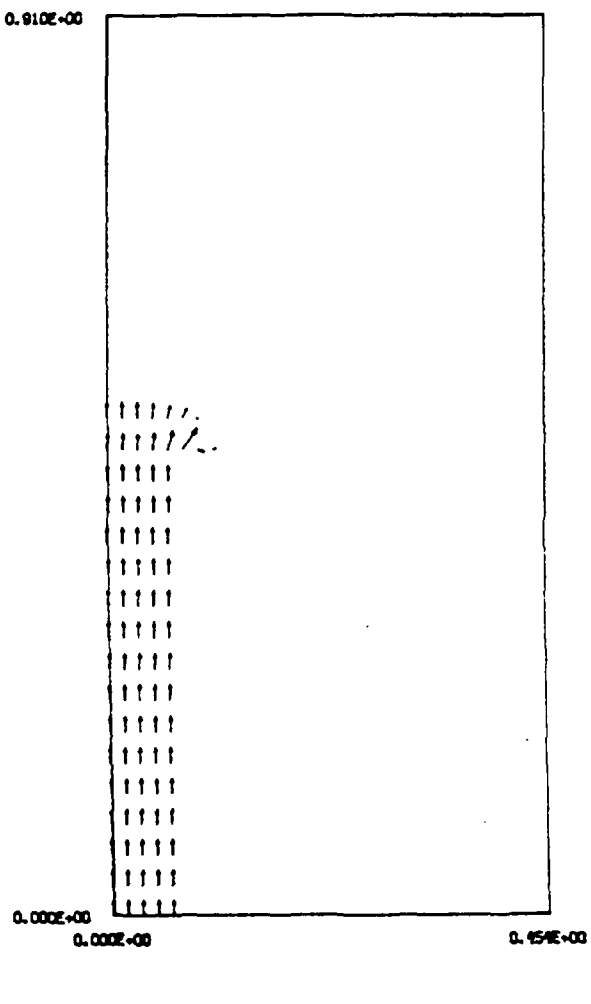


Figure 4c

BLAST DIFFRACTION FROM SHOCK TUBE

TIME= 0.10014E-03 SEC., STEP 152, DUMP TUBB0004 VELOCITY, M/SEC



0.50E+03  
MAXIMUM VECTOR

Figure 4d

BLAST DIFFRACTION FROM SHOCK TUBE  
TIME= 0.20090E-03 SEC., STEP 247, DUMP TUBB0005 PRESSURE, NEWTONS/M\*\*2

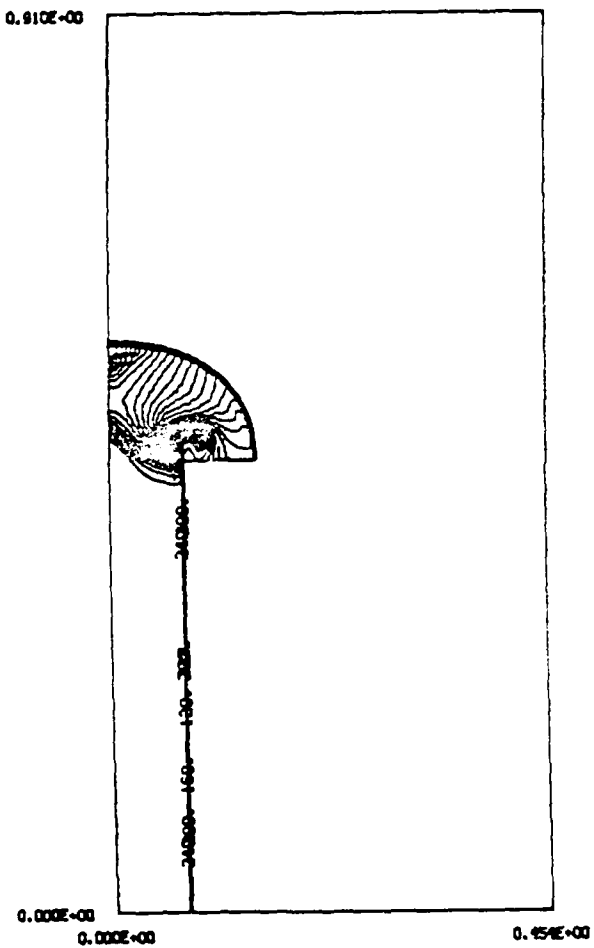


Figure 5a

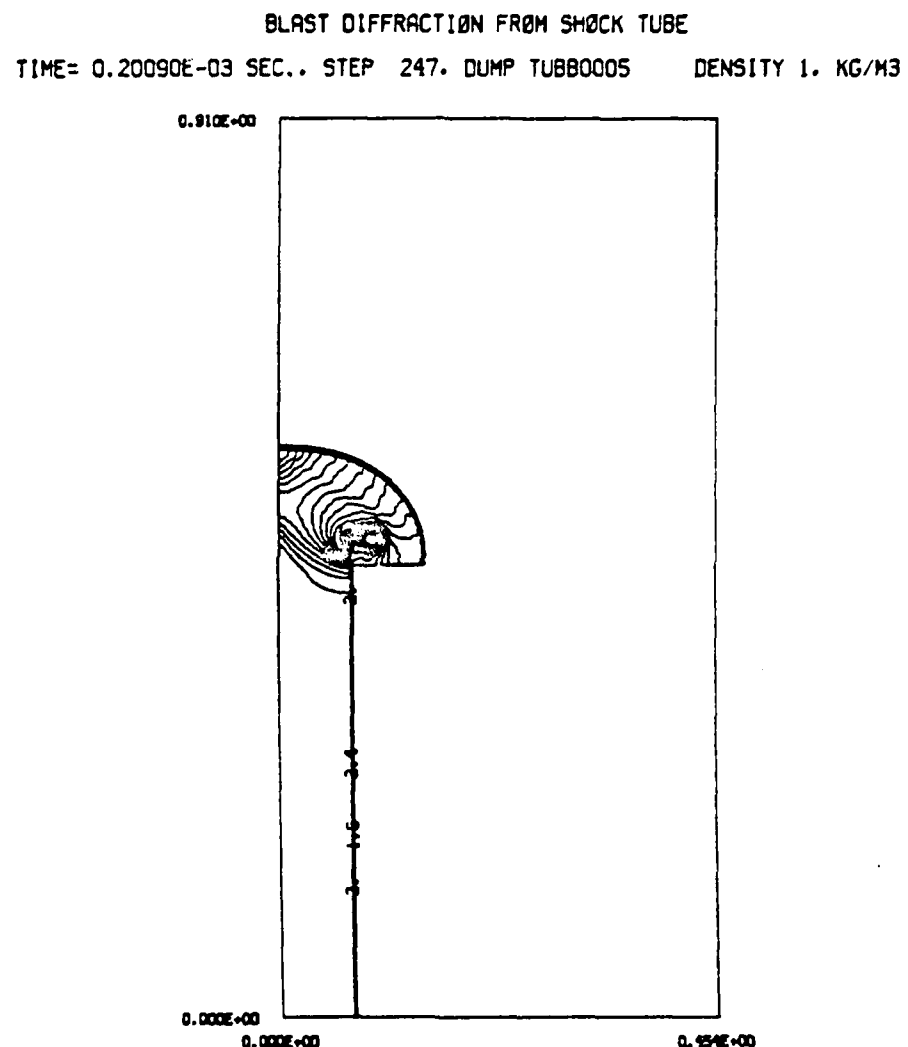


Figure 5b

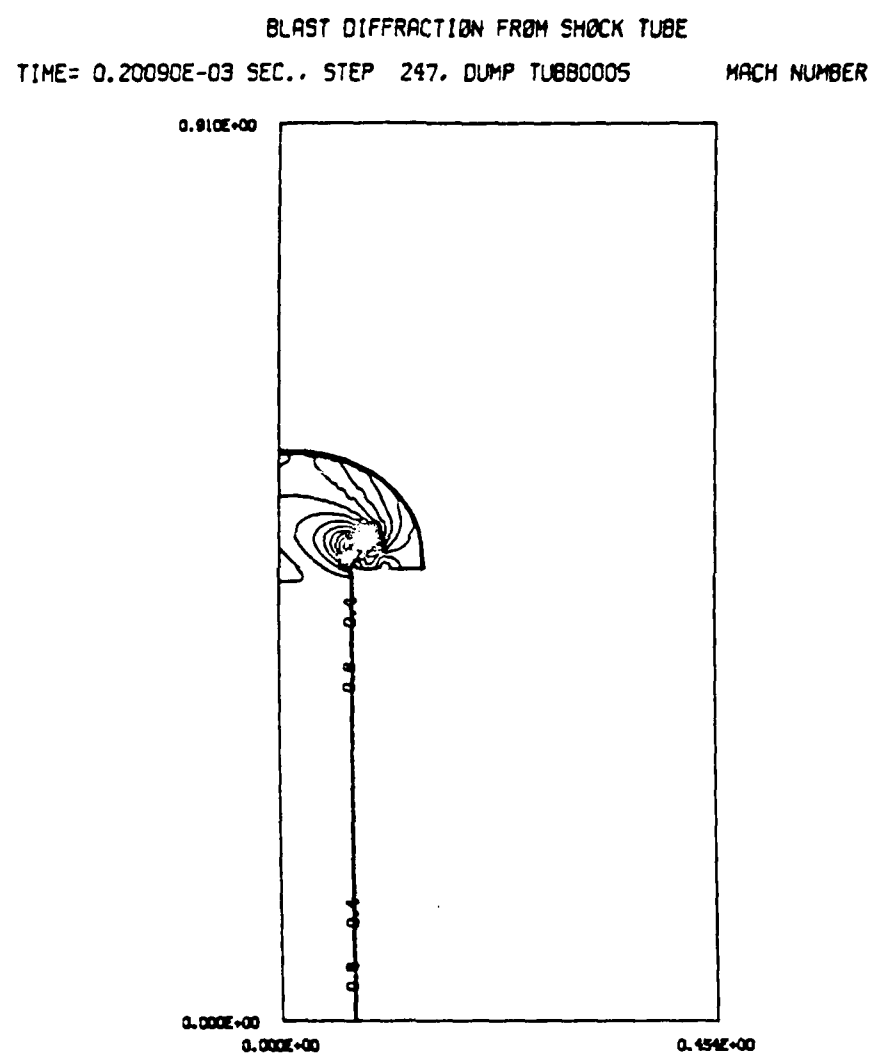
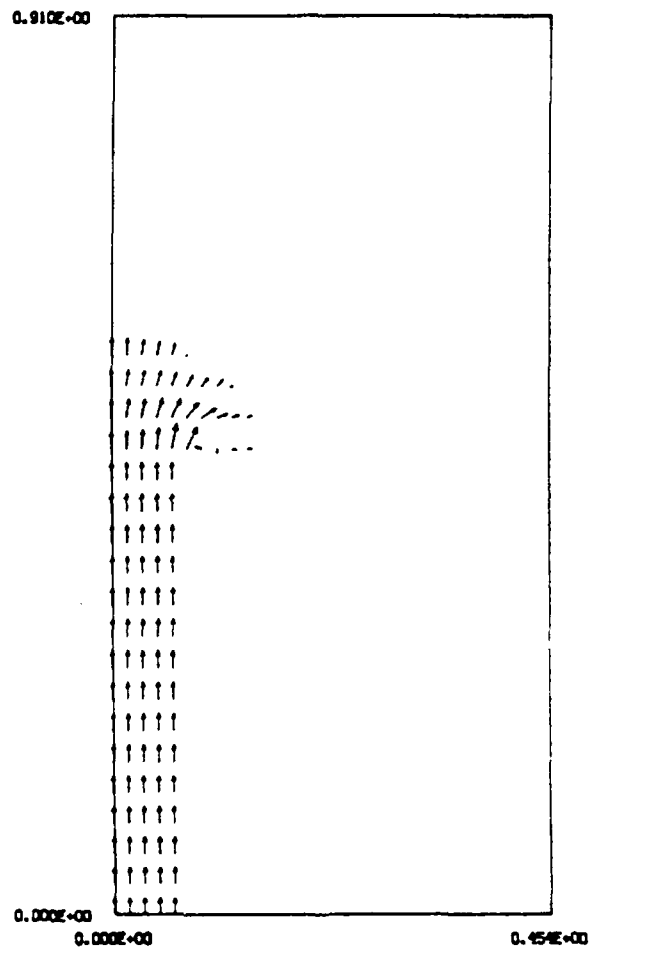


Figure 5c

BLAST DIFFRACTION FROM SHOCK TUBE  
TIME= 0.20090E-03 SEC., STEP 247, DUMP TUBB0005 VELOCITY, M/SEC



0.490E+03  
MAXIMUM VECTOR

Figure 5d

BLAST DIFFRACTION FROM SHOCK TUBE  
TIME= 0.50093E-03 SEC., STEP 534, DUMP TUBB0006 PRESSURE, NEWTONS/M\*\*2

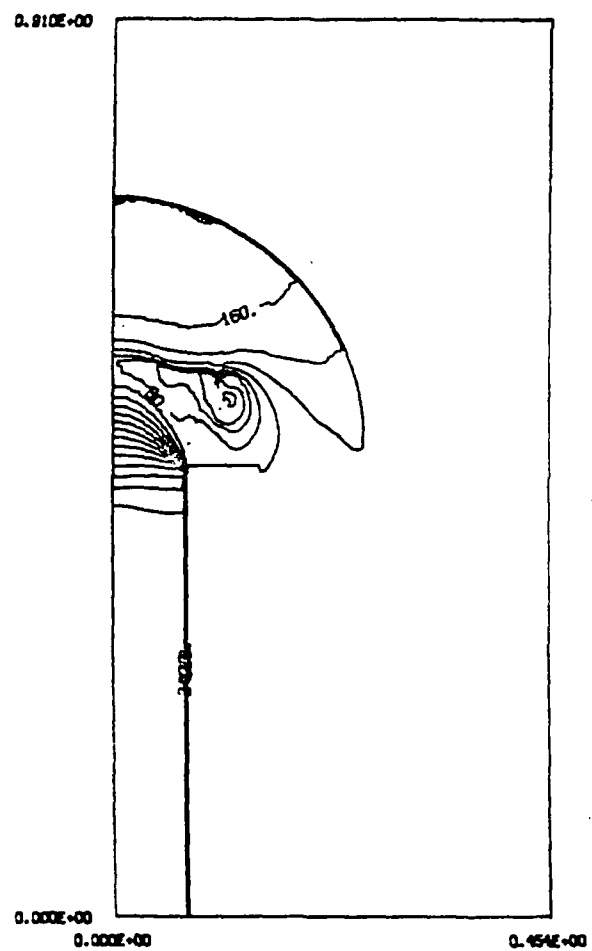


Figure 6a

BLAST DIFFRACTION FROM SHOCK TUBE  
TIME= 0.50093E-03 SEC., STEP 534, DUMP TUBB0006 DENSITY 1. KG/M3

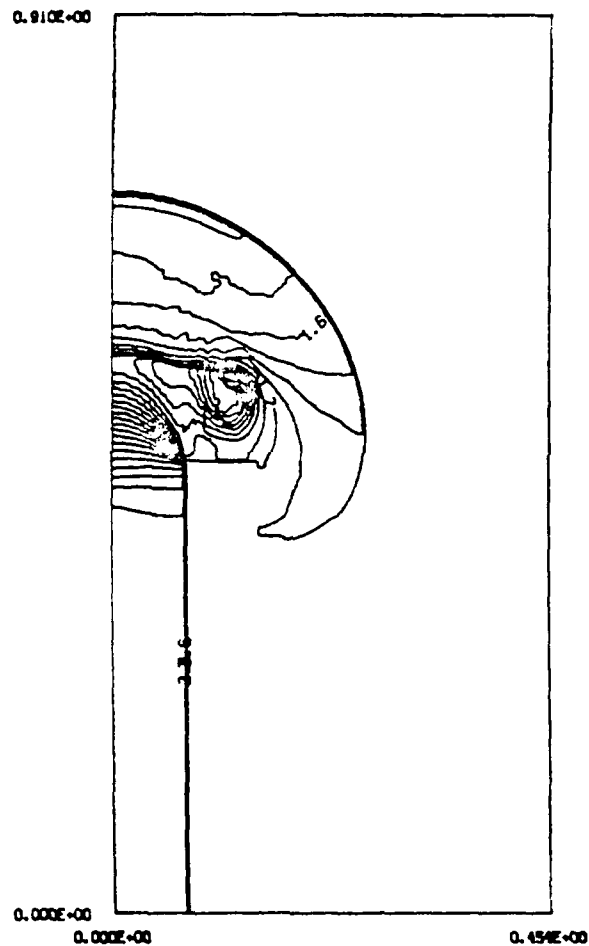


Figure 6b

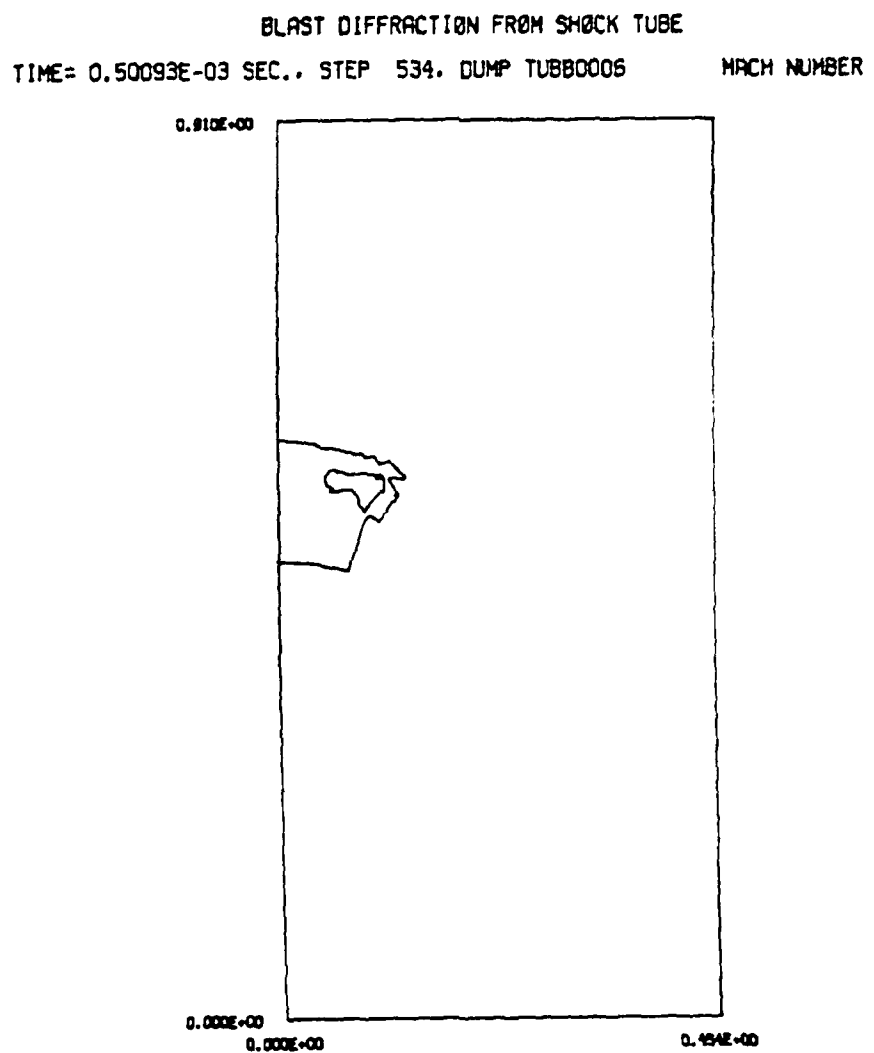


Figure 6c

BLAST DIFFRACTION FROM SHOCK TUBE  
TIME= 0.50093E-03 SEC., STEP 534, DUMP TUB80006 VELOCITY, M/SEC

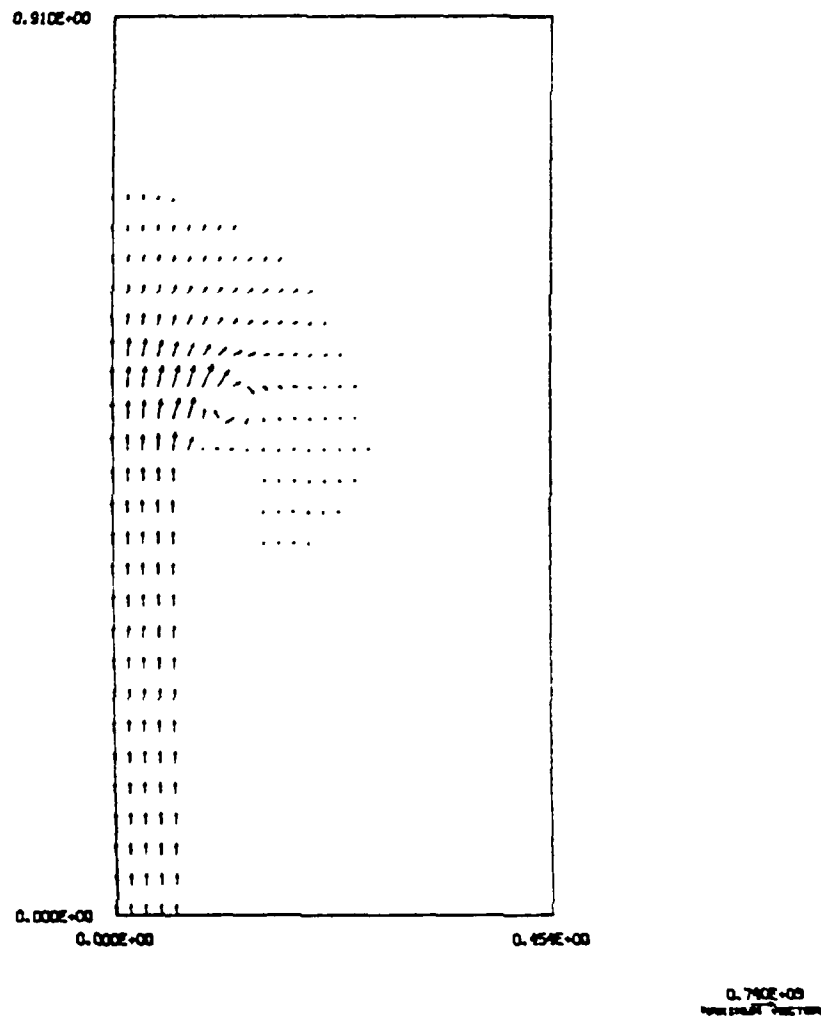


Figure 6d

BLAST DIFFRACTION FROM SHOCK TUBE

TIME= 0.10007E-02 SEC., STEP 1063, DUMP TUB80007 PRESSURE, NEWTONS/M\*\*2

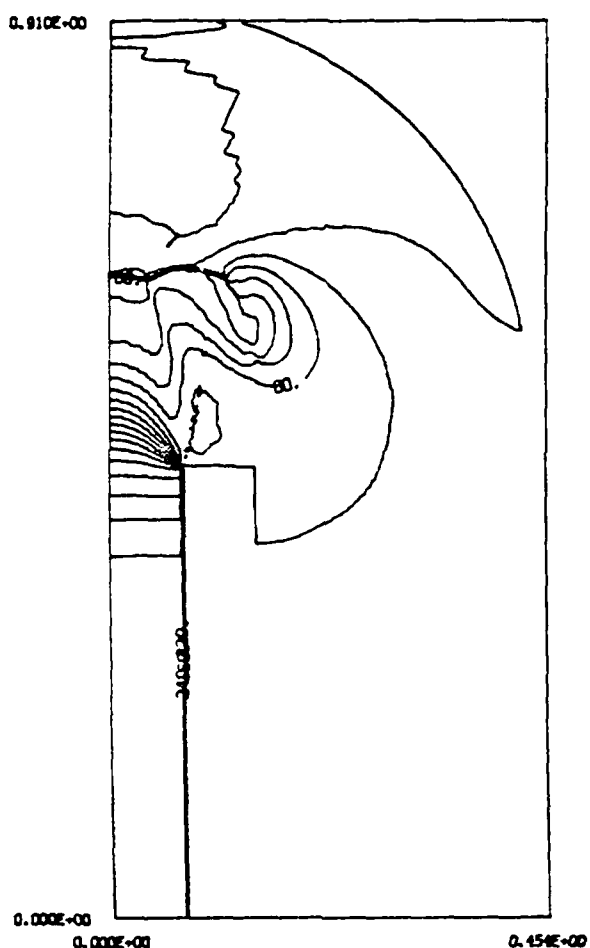


Figure 7a

BLAST DIFFRACTION FROM SHOCK TUBE  
TIME= 0.10007E-02 SEC., STEP 1063, DUMP TUBB0007      DENSITY 1, KG/M3

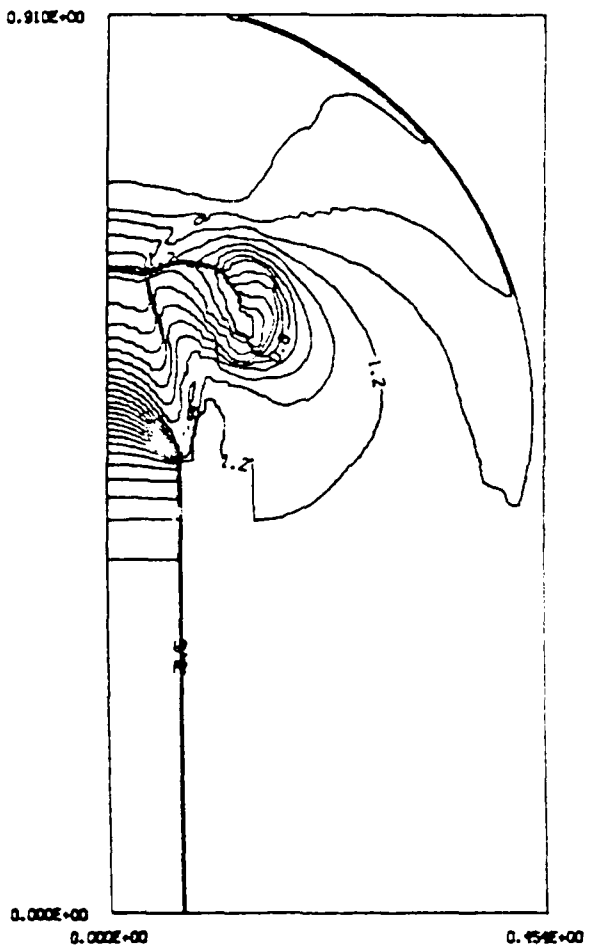


Figure 7b

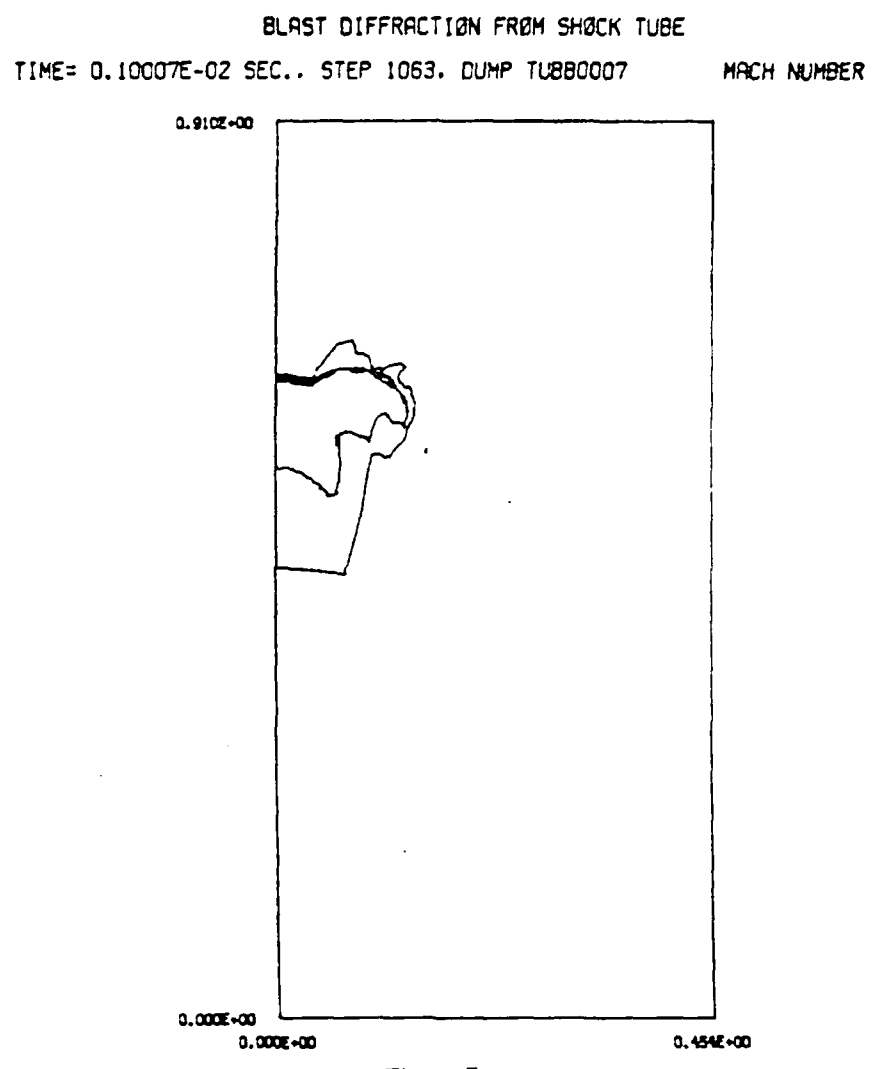


Figure 7c

BLAST DIFFRACTION FROM SHOCK TUBE

TIME= 0.10007E-02 SEC., STEP 1063, DUMP TUB80007      VELOCITY, M/SEC

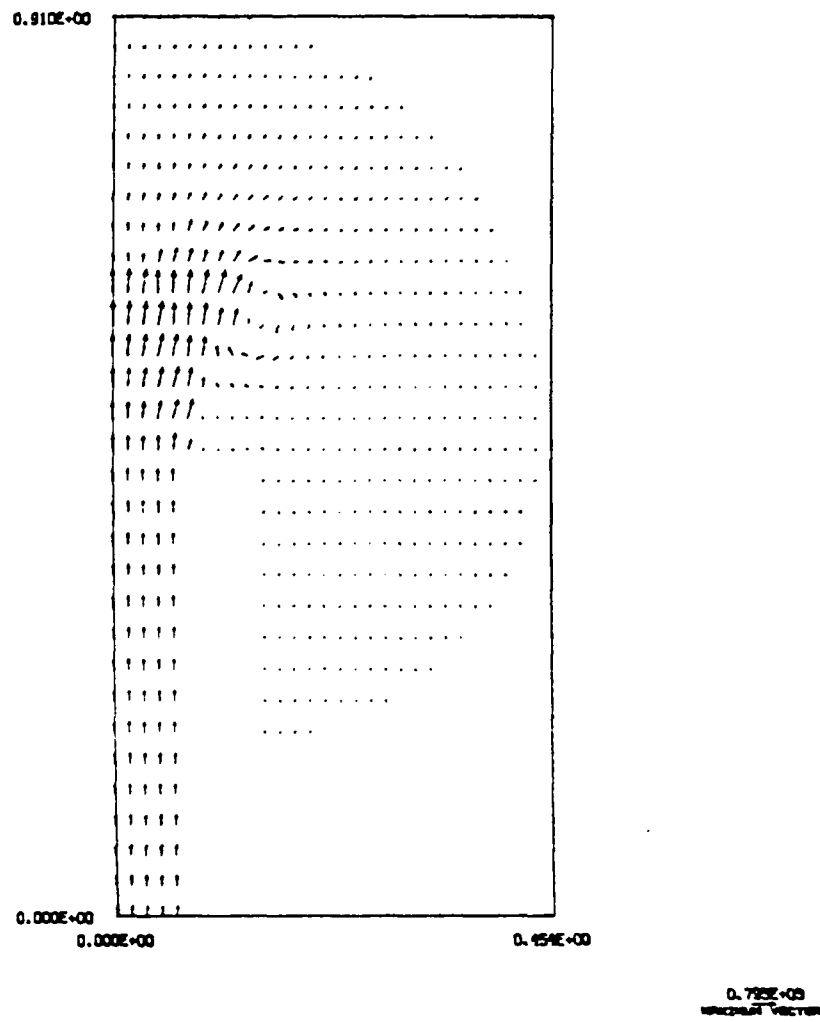


Figure 7d

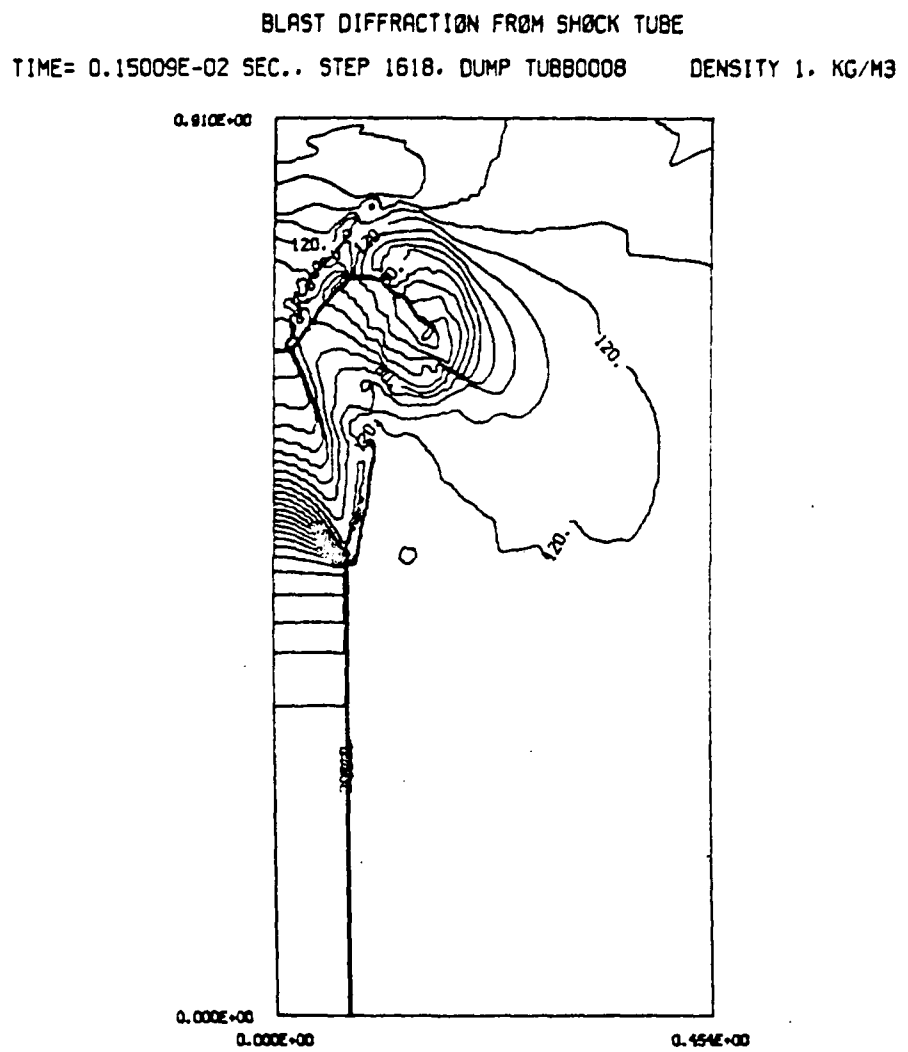
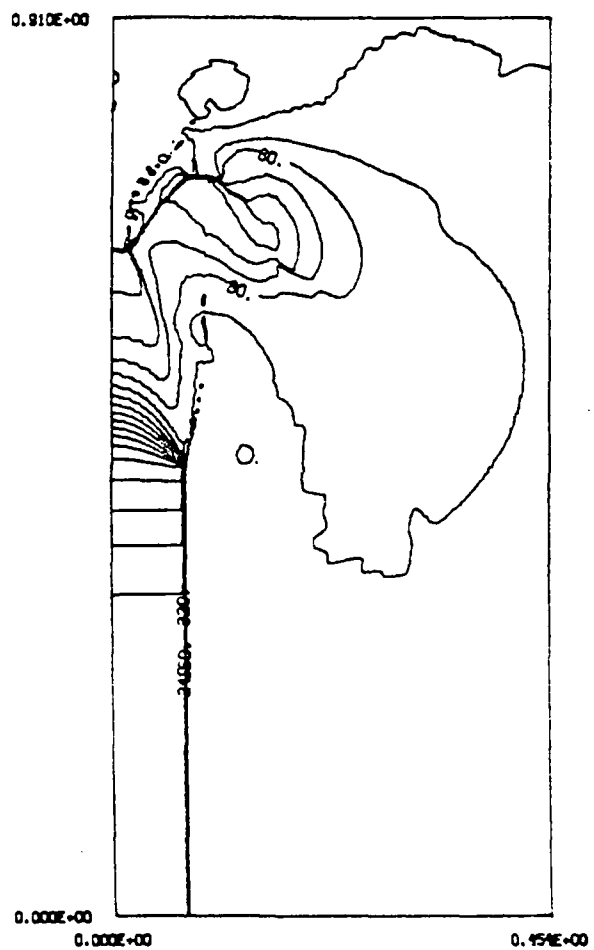


Figure 8a

## BLAST DIFFRACTION FROM SHOCK TUBE

TIME= 0.15009E-02 SEC.. STEP 1618. DUMP TUBB0008 PRESSURE,NEWTONS/M\*\*2



**Figure 8b**

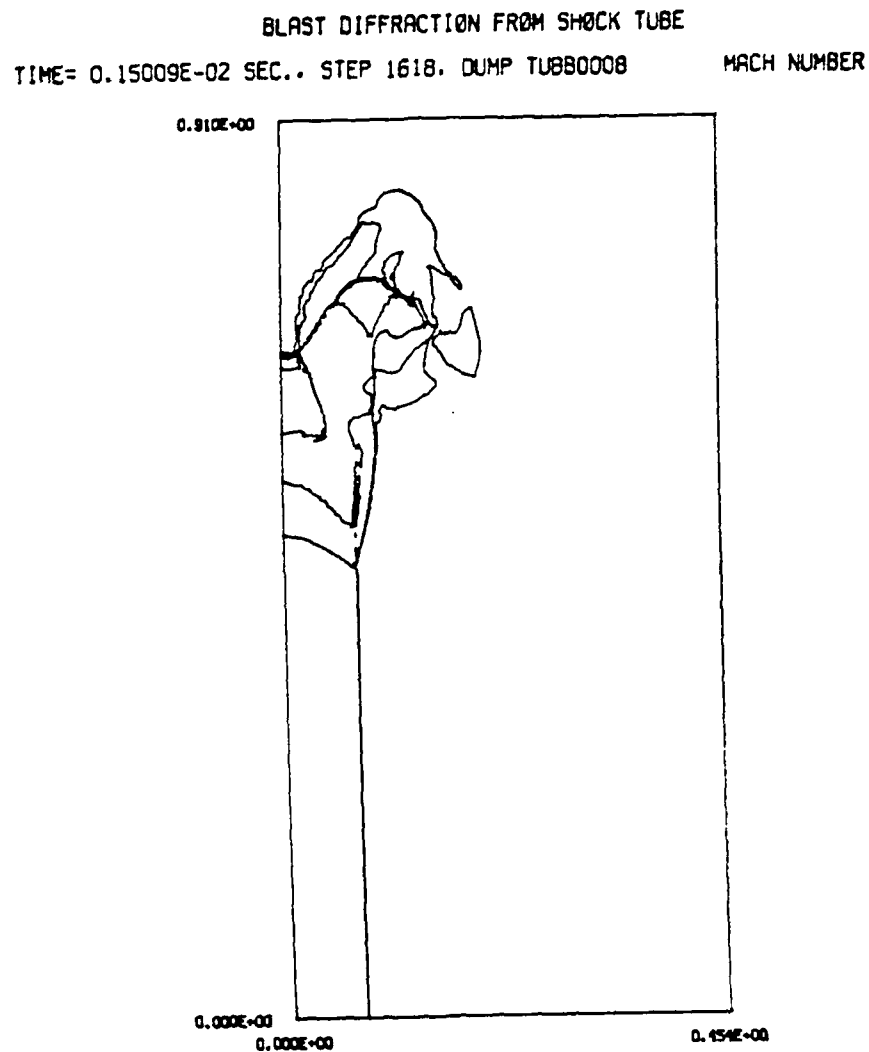


Figure 8c

BLAST DIFFRACTION FROM SHOCK TUBE

TIME= 0.15009E-02 SEC., STEP 1618, DUMP TUBB0008      VELOCITY, M/SEC

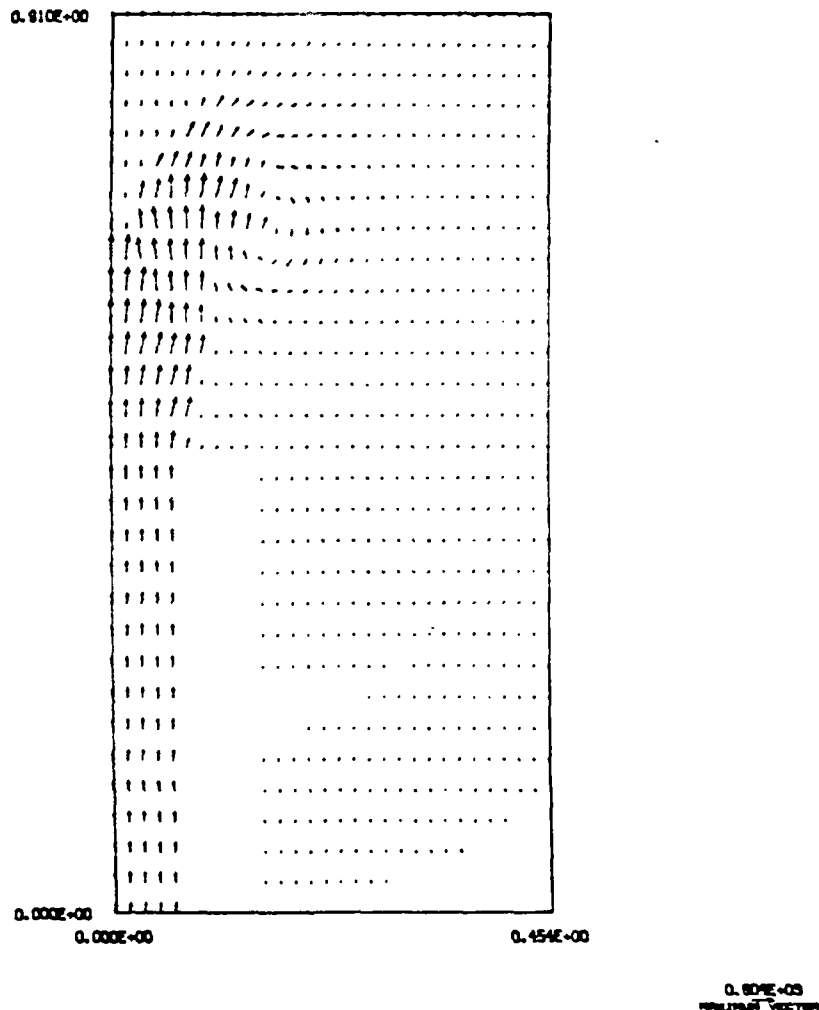
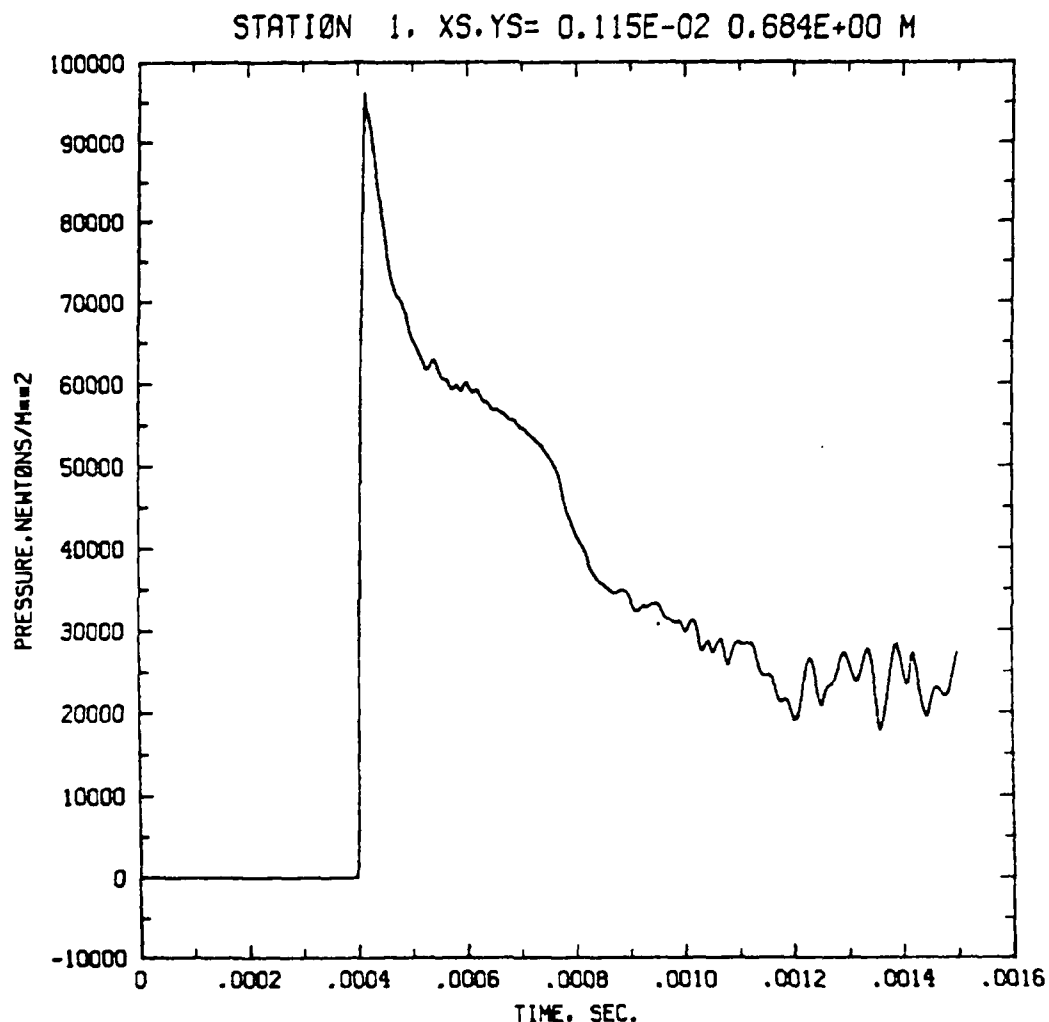


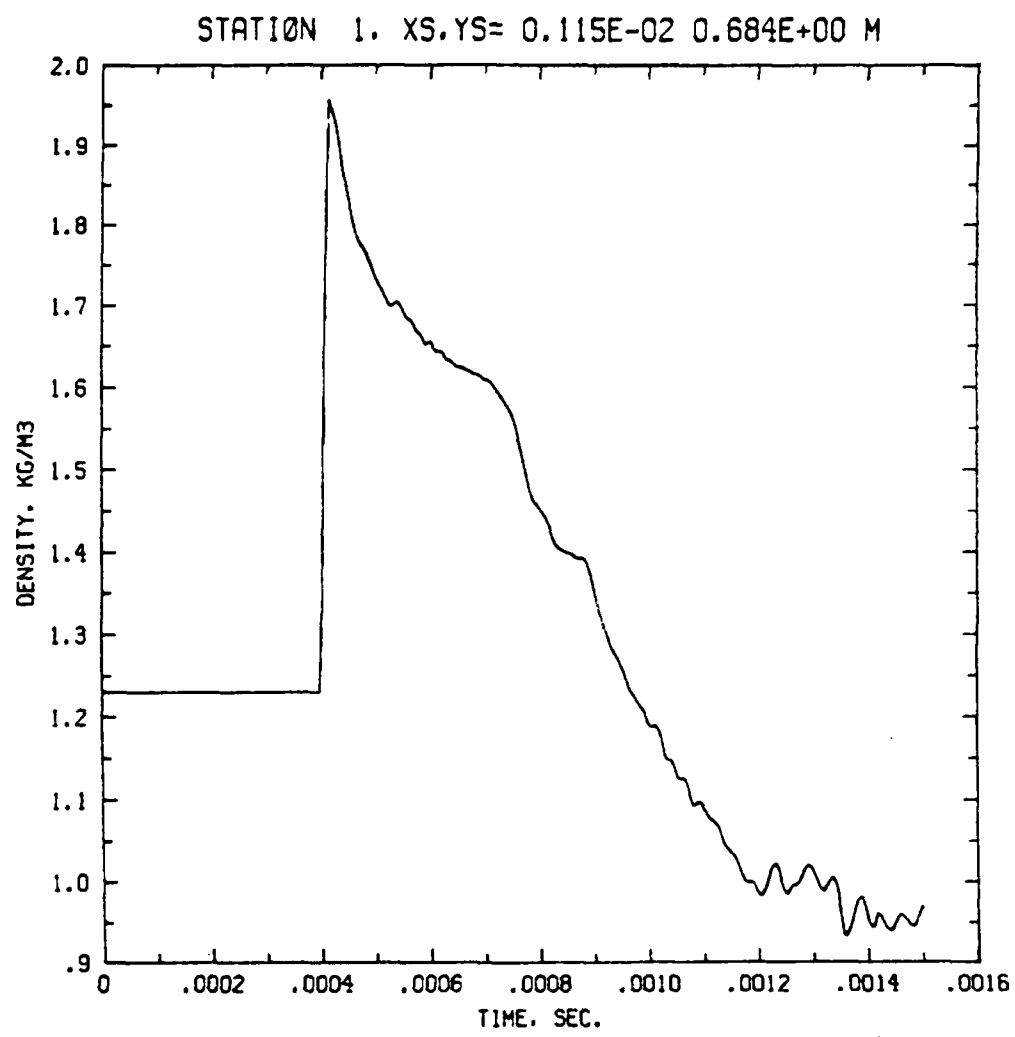
Figure 8d



BLAST DIFFRACTION FROM SHOCK TUBE

7 DUMPS. LAST DUMP IS TUE00008

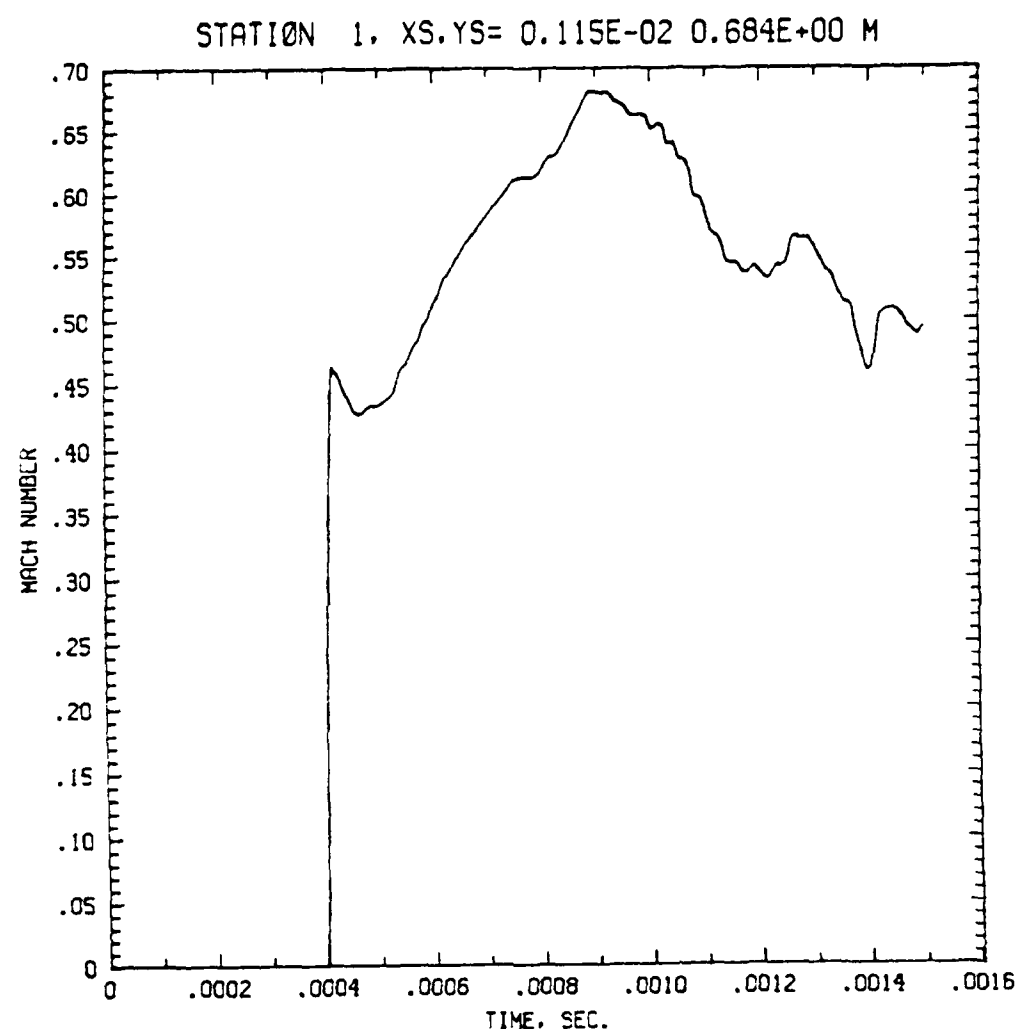
Figure 9a



BLAST DIFFRACTION FROM SHOCK TUBE

7 DUMPS. LAST DUMP IS TUE80008

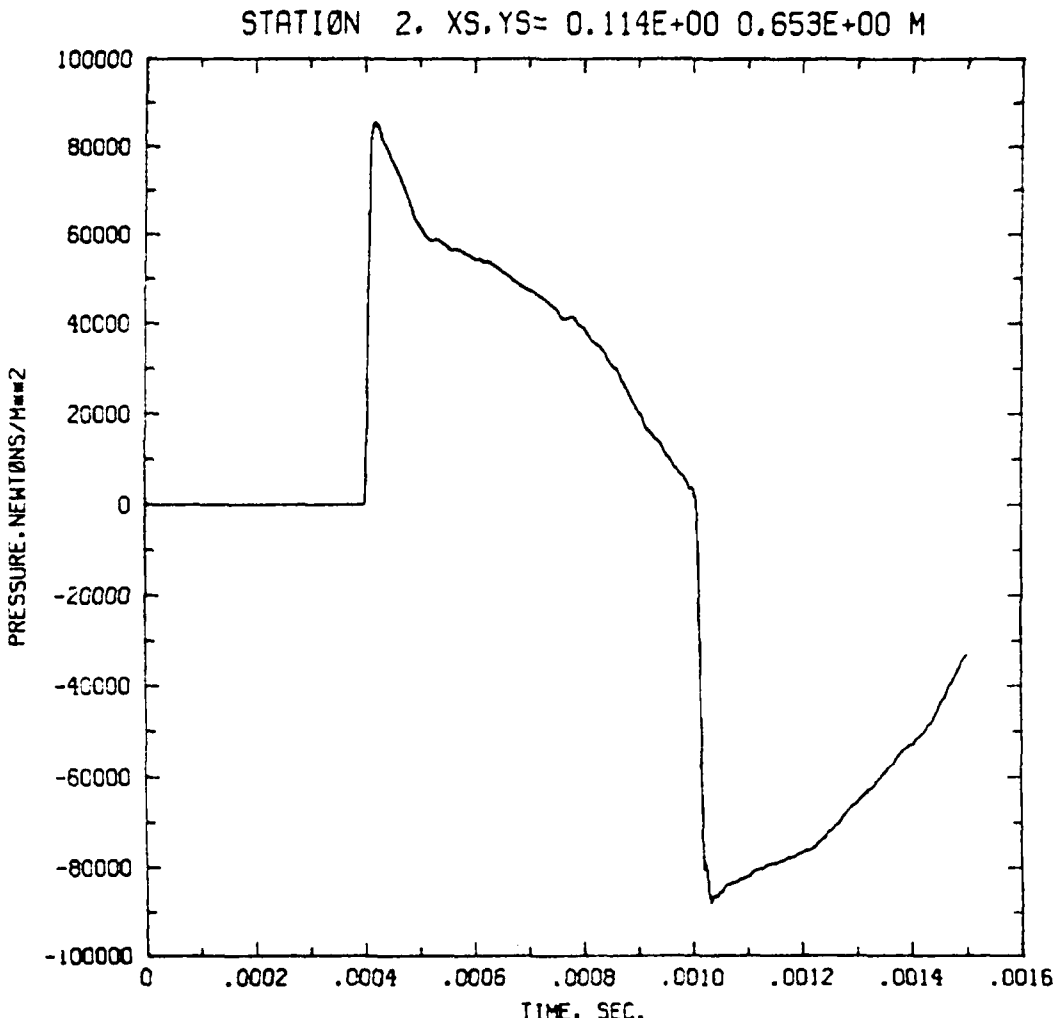
Figure 9b



BLAST DIFFRACTION FROM SHOCK TUBE

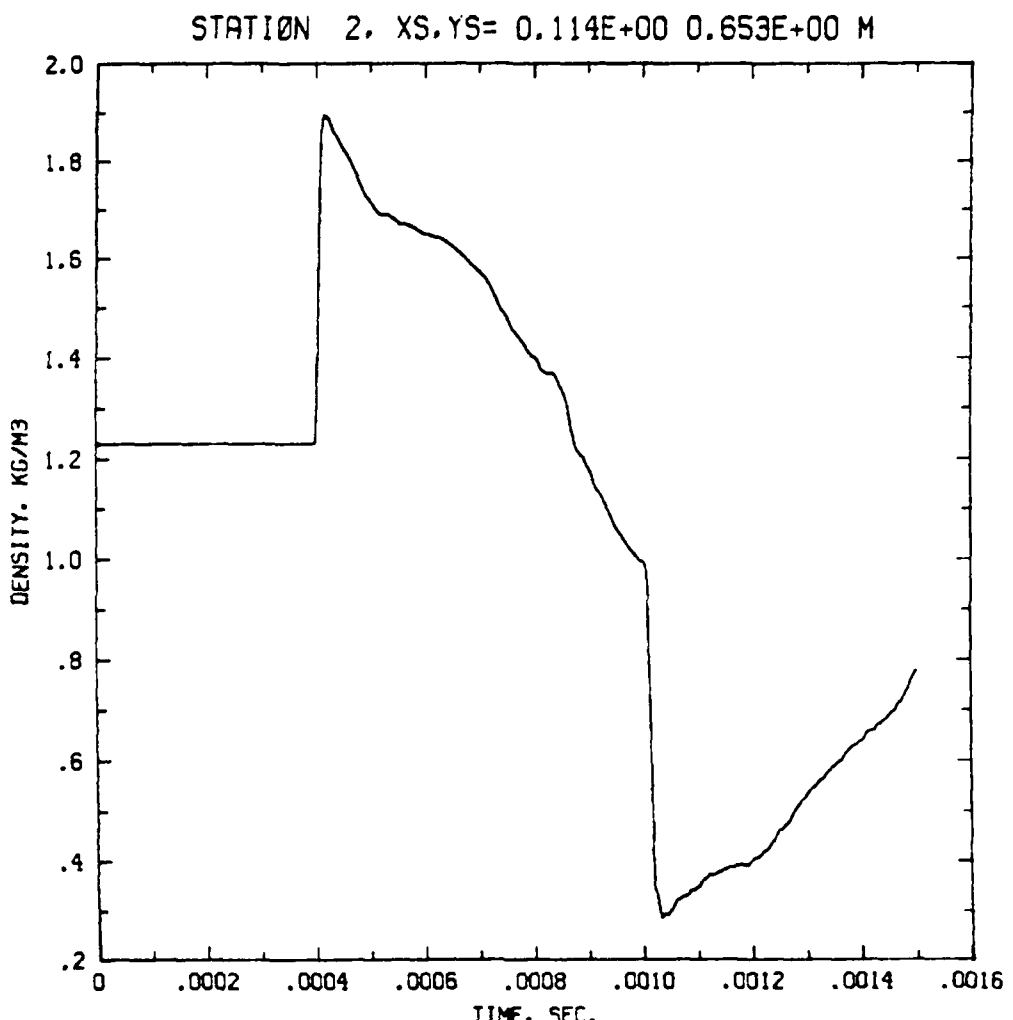
7 DUMPS. LAST DUMP IS TUB800008

Figure 9c



BLAST DIFFRACTION FROM SHOCK TUBE  
7 DUMPS. LAST DUMP IS TUE50000

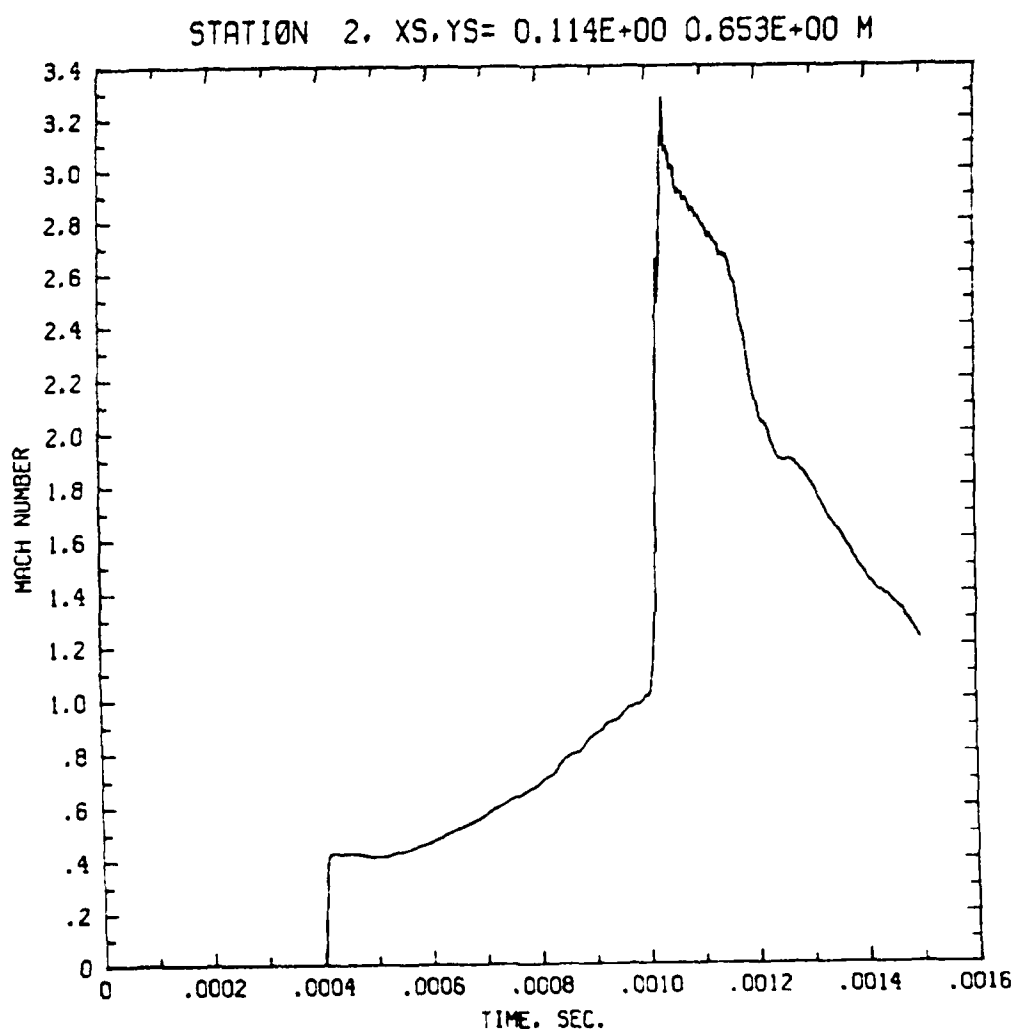
Figure 10a



BLAST DIFFRACTION FROM SHOCK TUBE

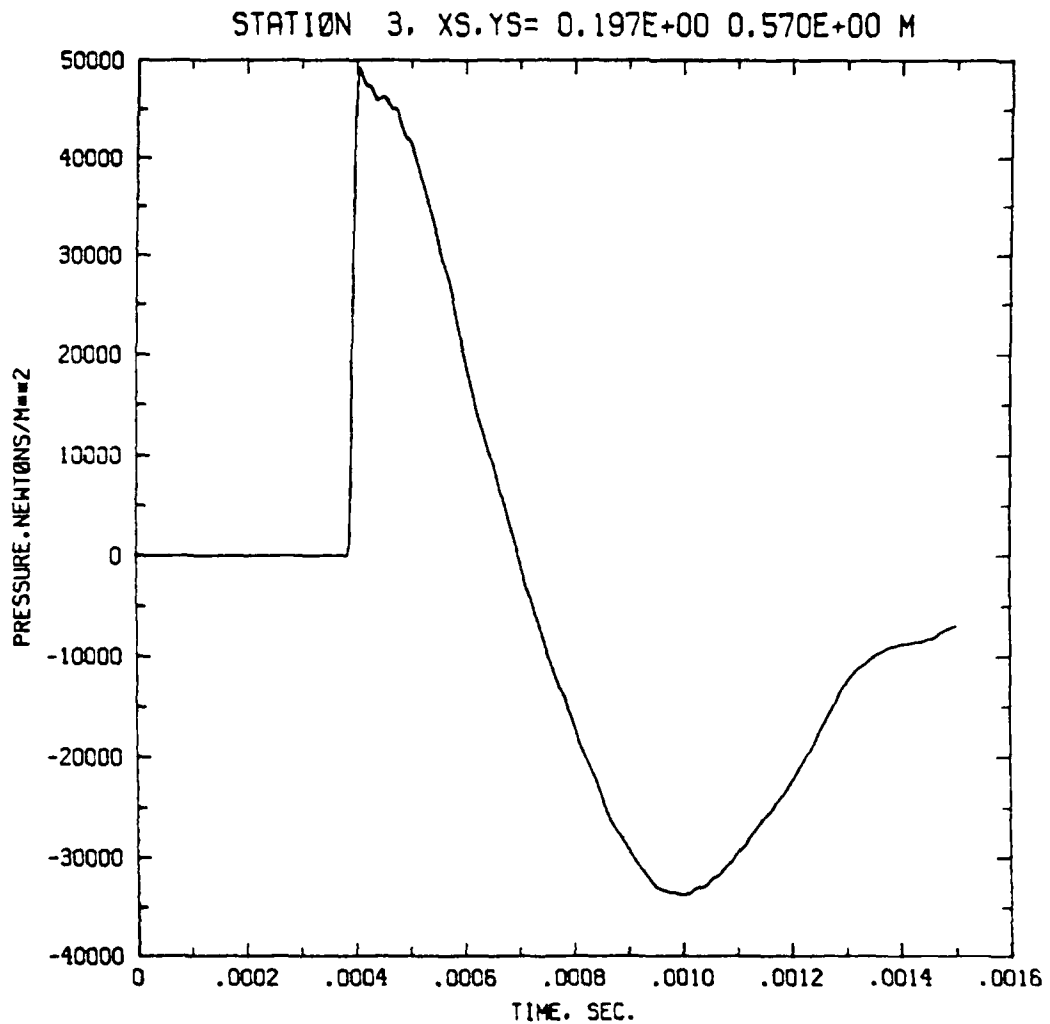
7 DUMPS. LAST DUMP IS TUB8000S

Figure 10b



BLAST DIFFRACTION FROM SHOCK TUBE  
7 DUMPS. LAST DUMP IS TUE00008

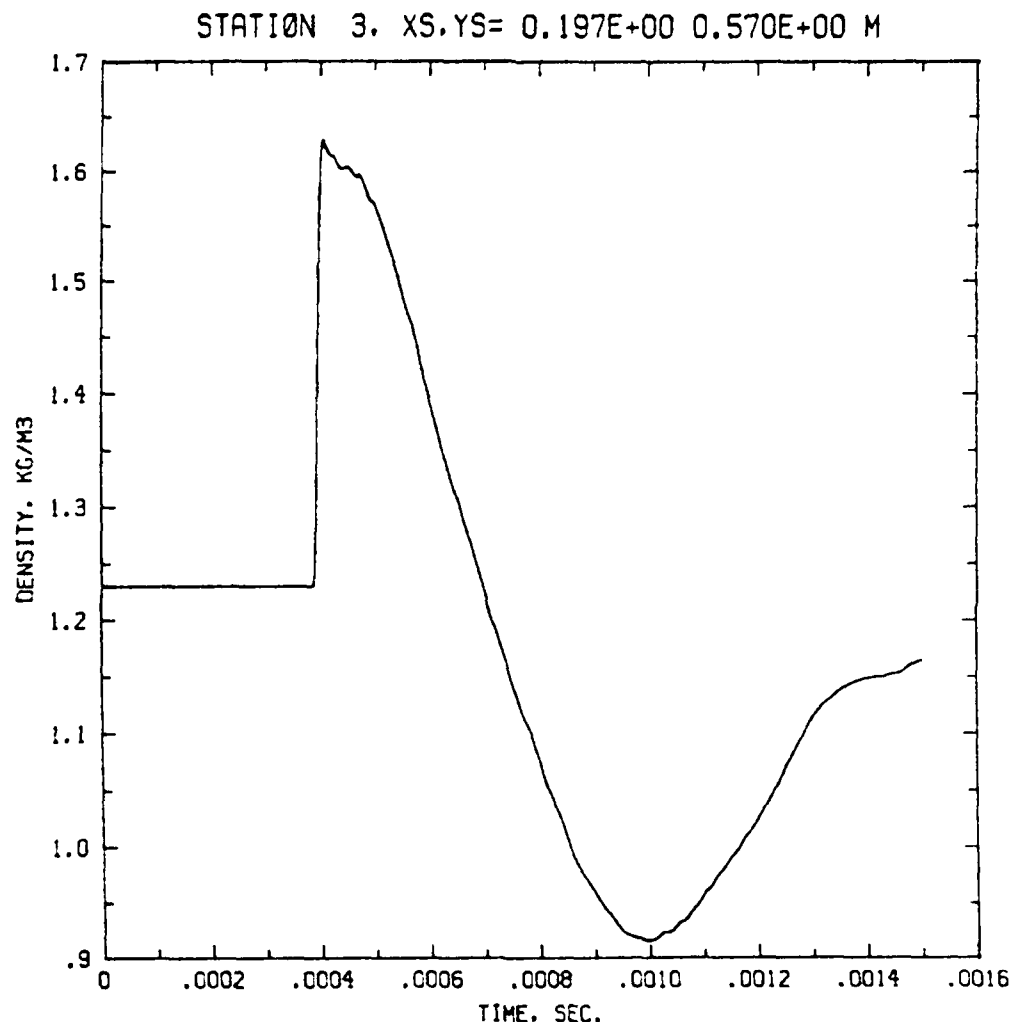
Figure 10c



BLAST DIFFRACTION FROM SHOCK TUBE

7 DUMPS. LAST DUMP IS TUB80000

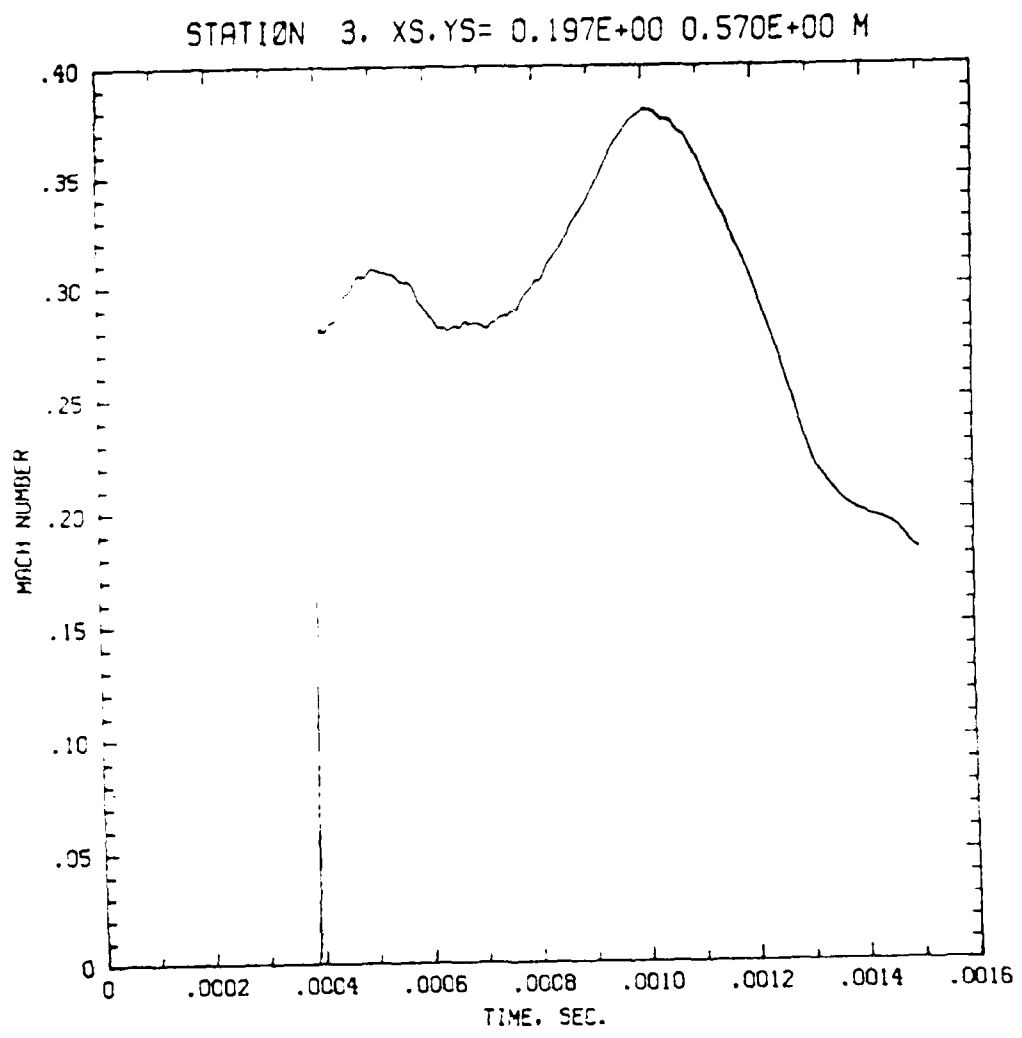
Figure 11a



BLAST DIFFRACTION FROM SHOCK TUBE

7 DUMPS. LAST DUMP IS TUE8000S

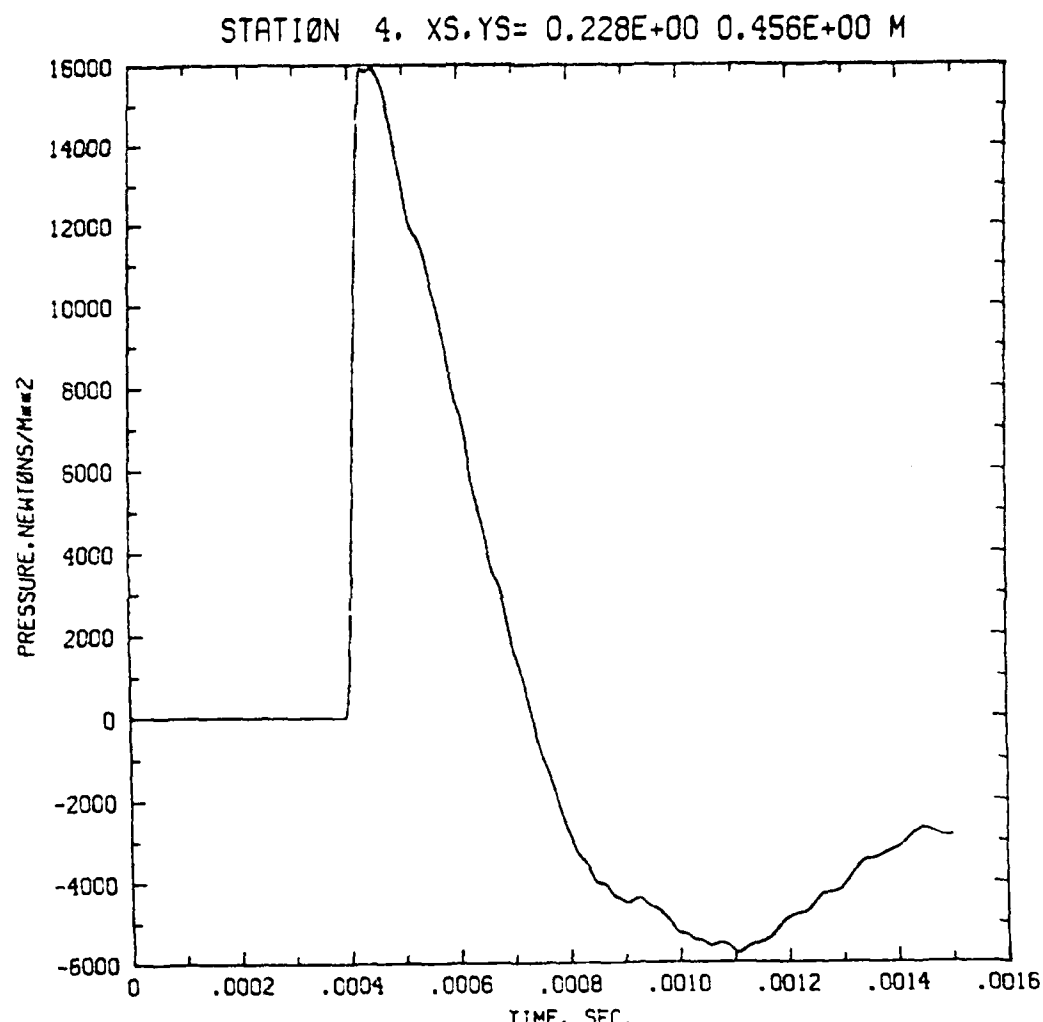
Figure 11b



BLAST DIFFRACTION FROM SHOCK TUBE

7 DUMPS. LAST DUMP IS TUBES0008

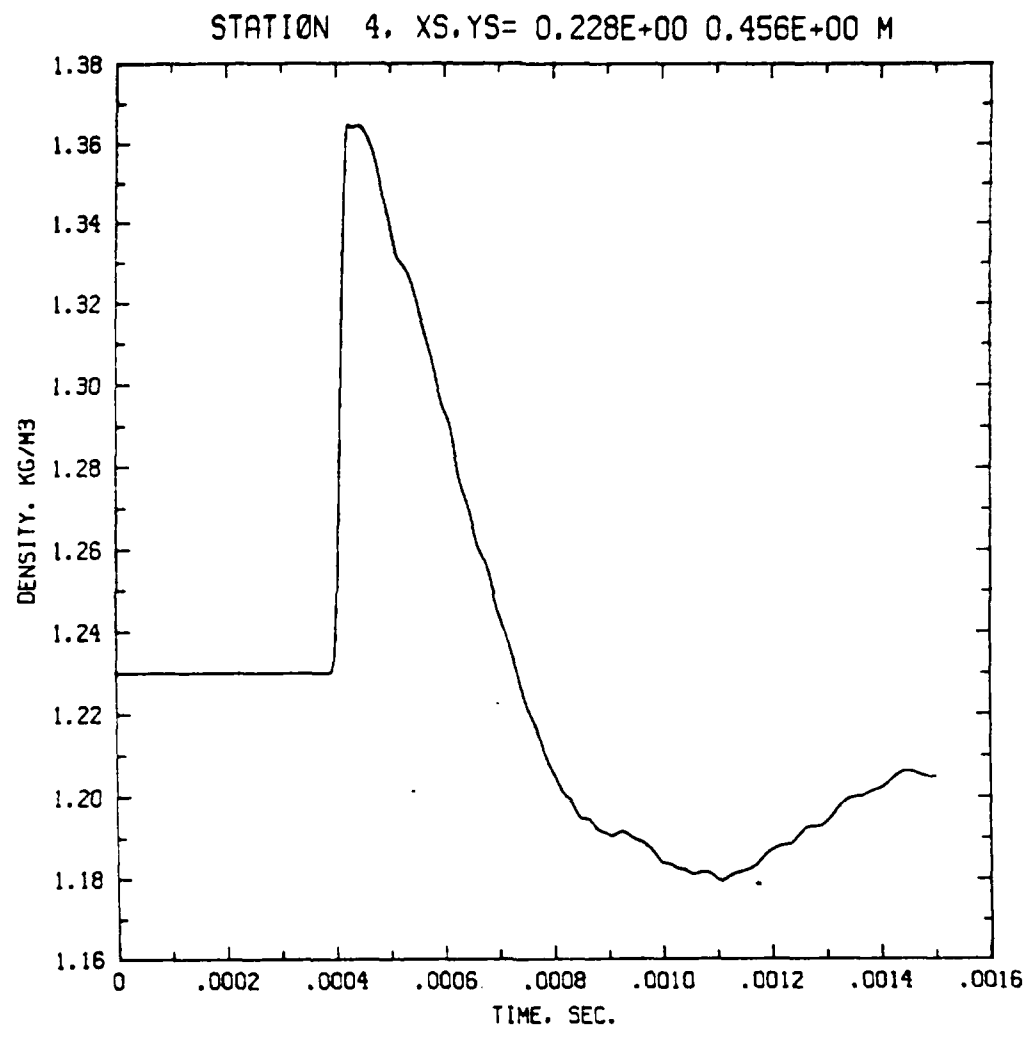
Figure 11c



BLAST DIFFRACTION FROM SHOCK TUBE

7 DUMPS. LAST DUMP IS T0.80000S

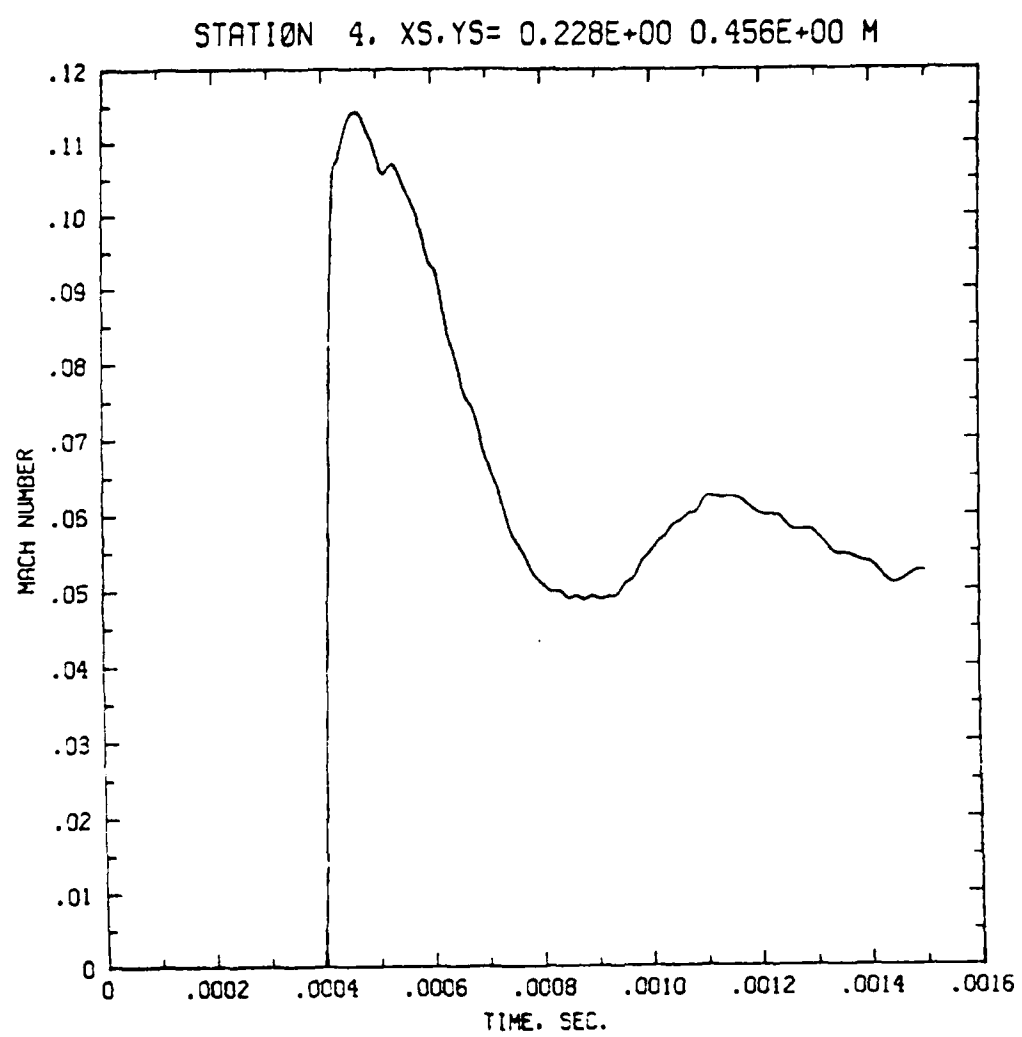
Figure 12a



BLAST DIFFRACTION FROM SHOCK TUBE

7 DUMPS. LAST DUMP IS T1880008

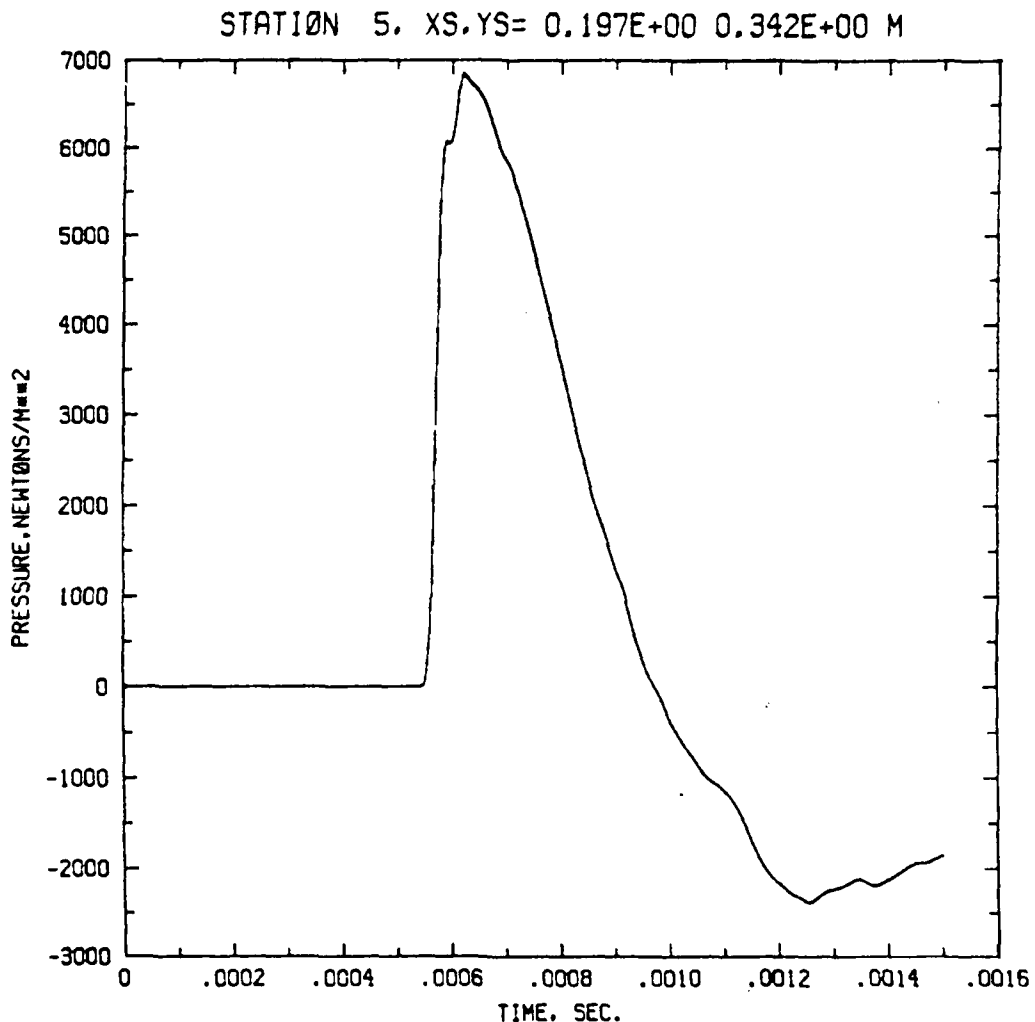
Figure 12b



BLAST DIFFRACTION FROM SHOCK TUBE

7 DUMPS. LAST DUMP IS TUB80008

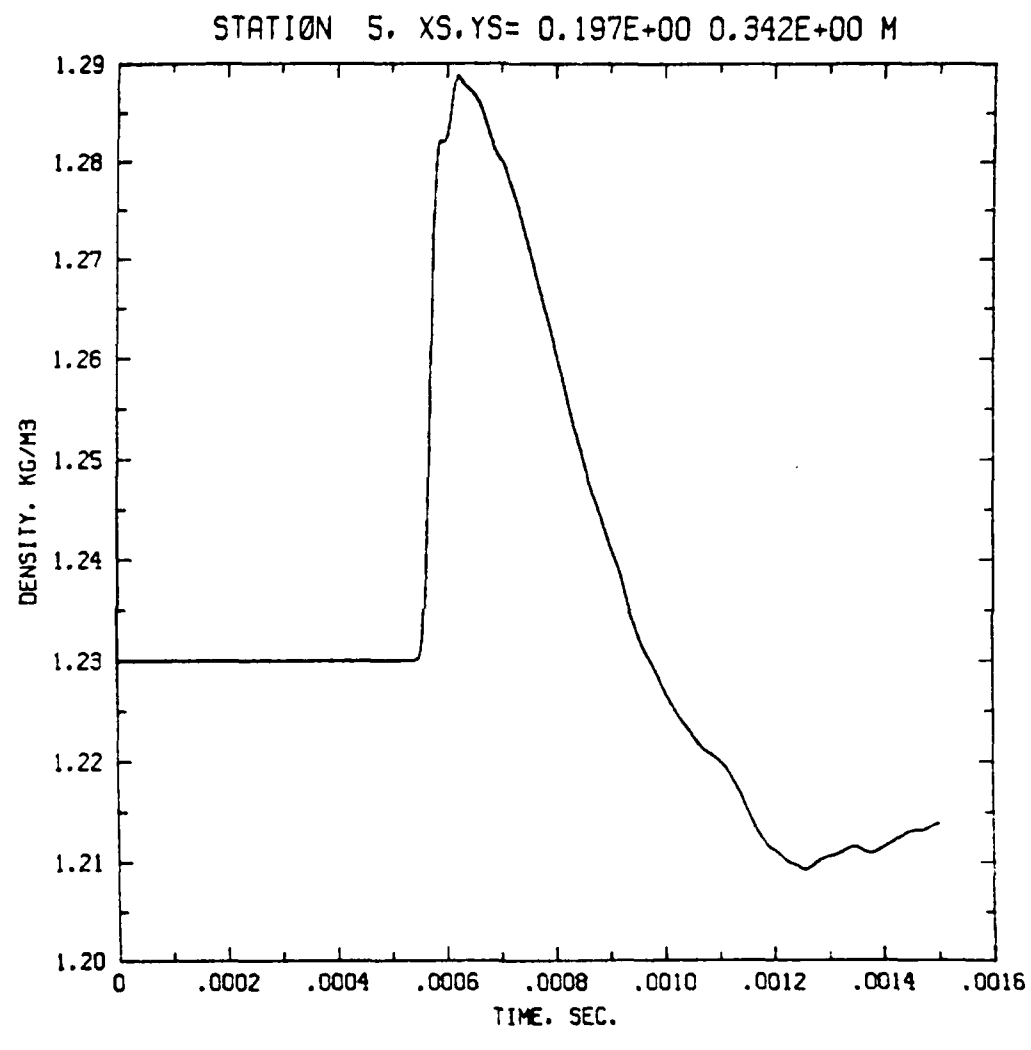
Figure 12c



BLAST DIFFRACTION FROM SHOCK TUBE

7 DUMPS. LAST DUMP IS TUBE DOOR

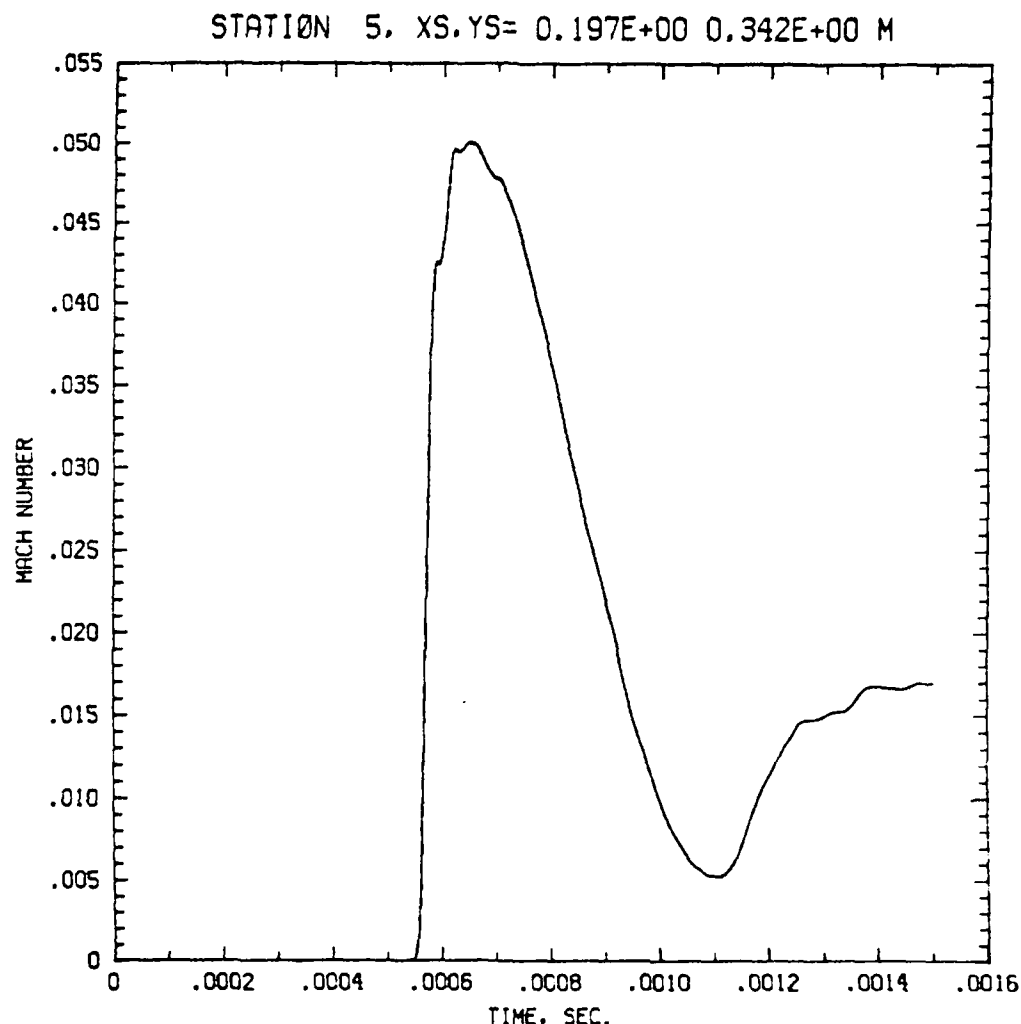
Figure 13a



BLAST DIFFRACTION FROM SHOCK TUBE

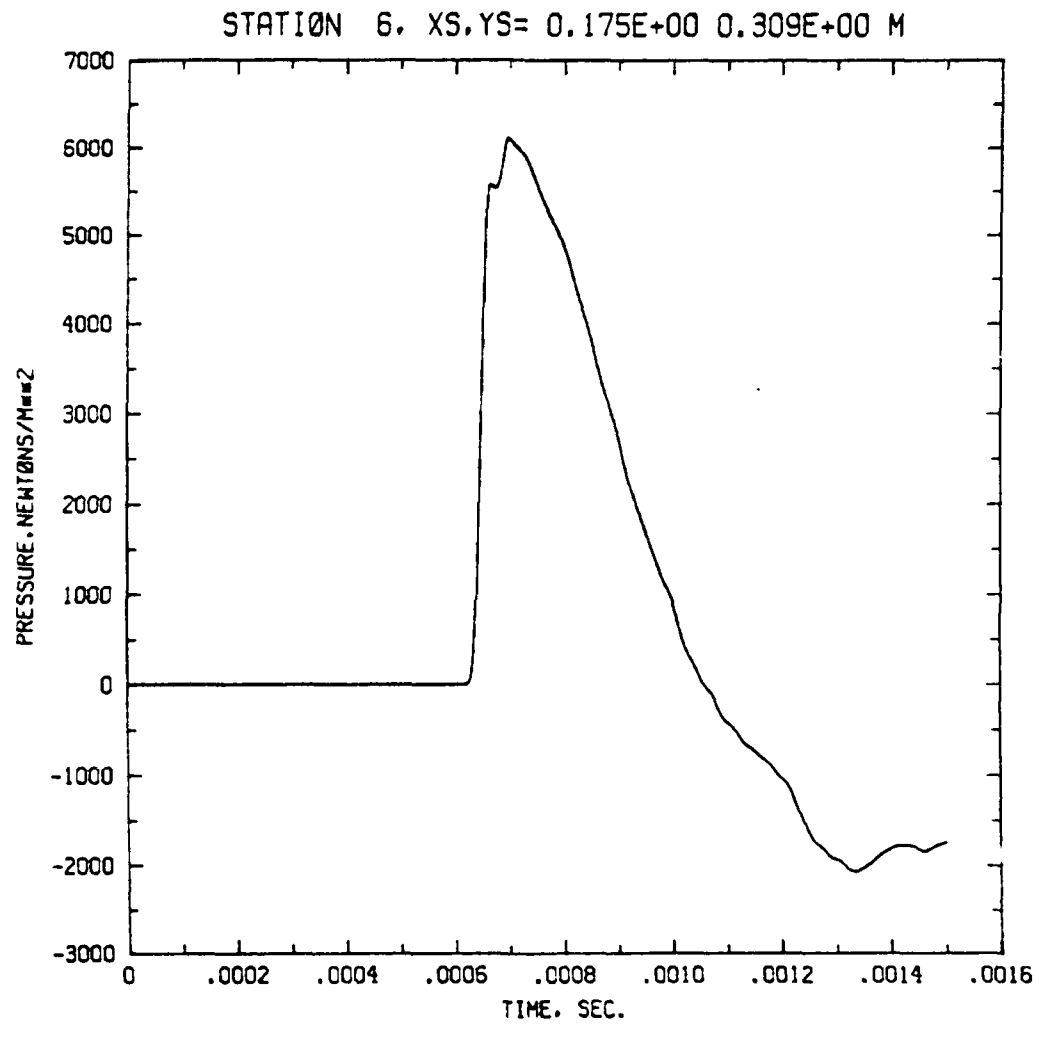
7 DUMPS. LAST DUMP IS TUBE00008

Figure 13b



BLAST DIFFRACTION FROM SHOCK TUBE  
7 DUMPS. LAST DUMP IS TUE30000

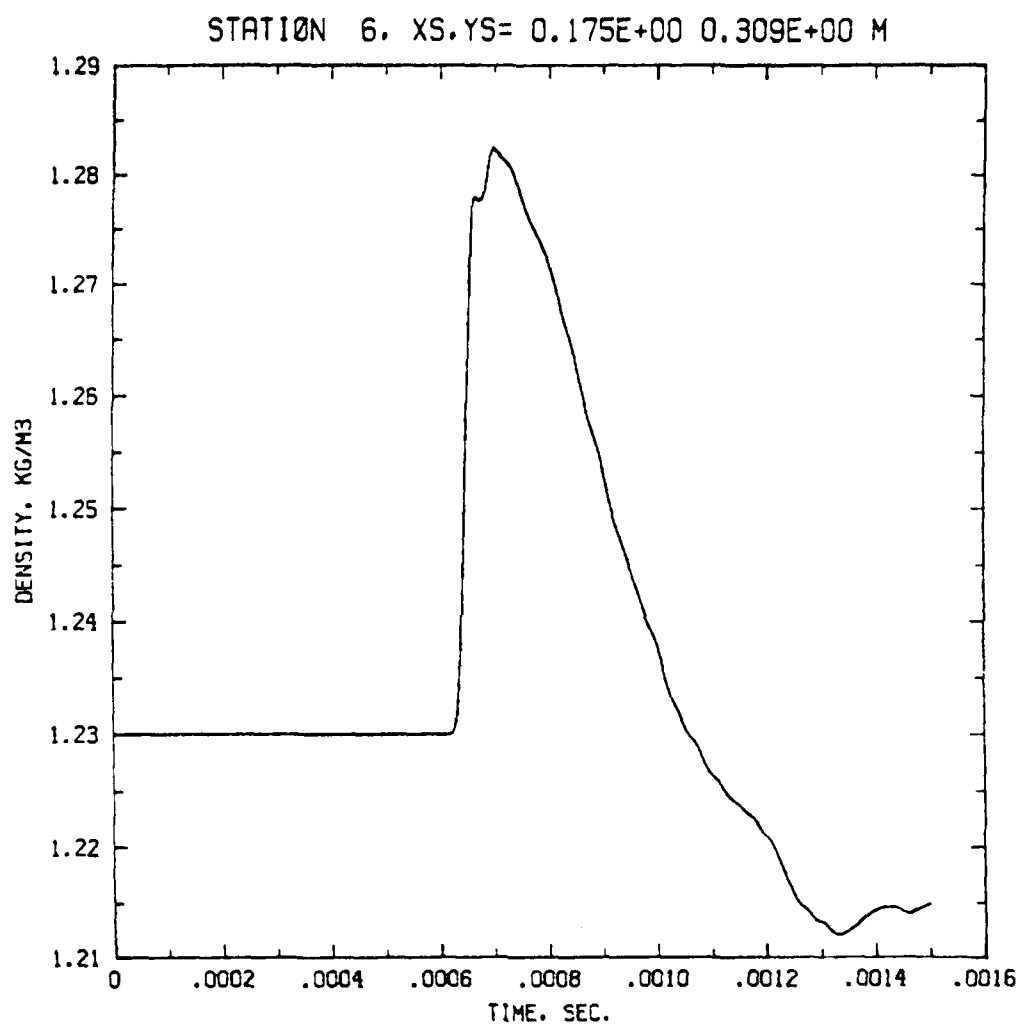
Figure 13c



BLAST DIFFRACTION FROM SHOCK TUBE

7 DUMPS. LAST DUMP IS TUBES0008

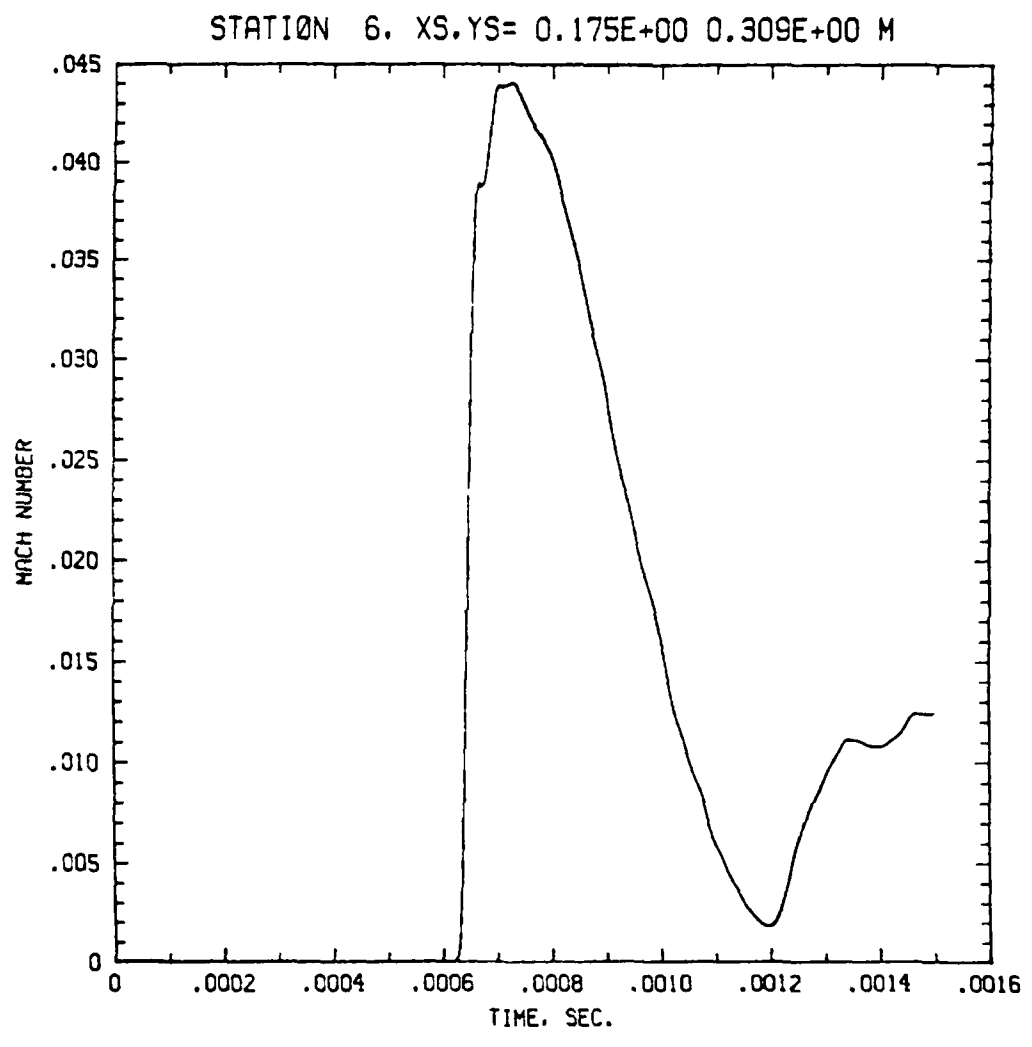
Figure 14a



BLAST DIFFRACTION FROM SHOCK TUBE

7 DUMPS. LAST DUMP IS T180008

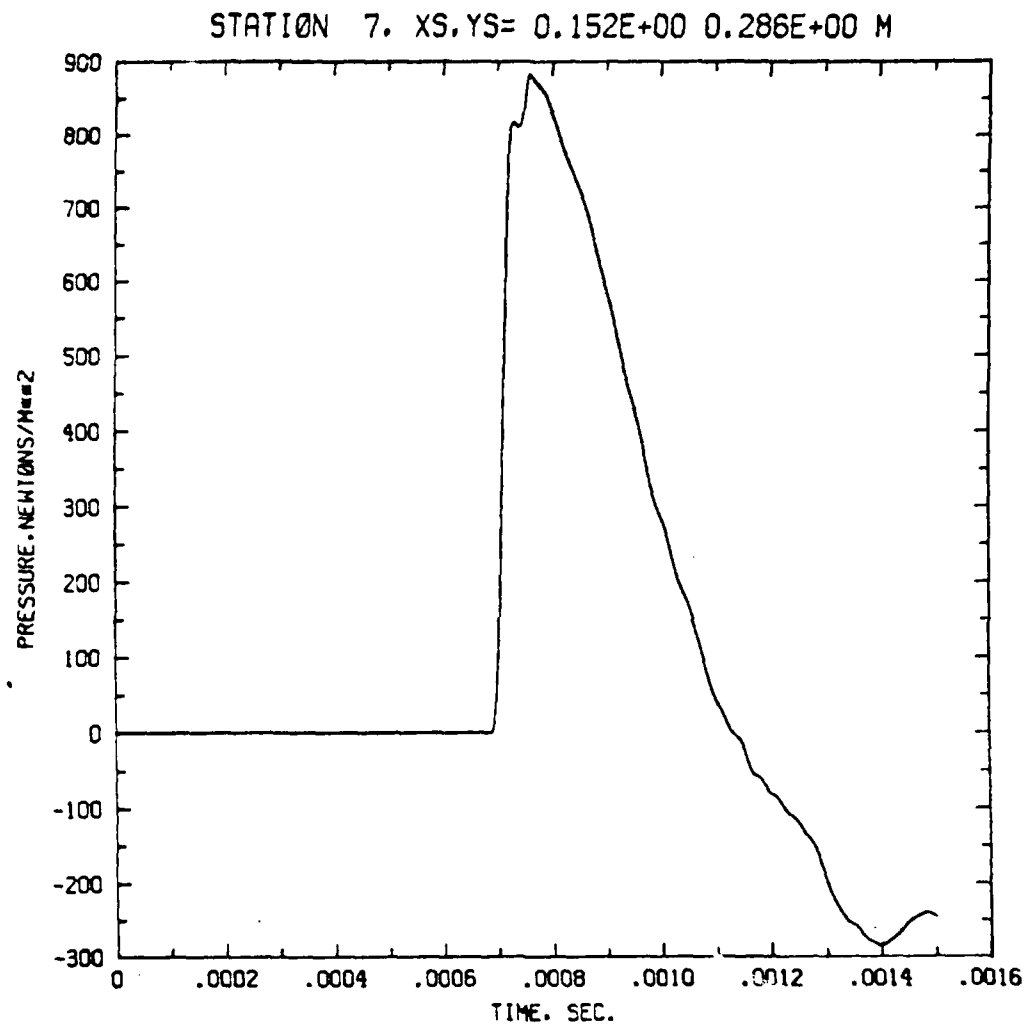
Figure 14b



BLAST DIFFRACTION FROM SHOCK TUBE

7 DUMPS. LAST DUMP IS TUE80008

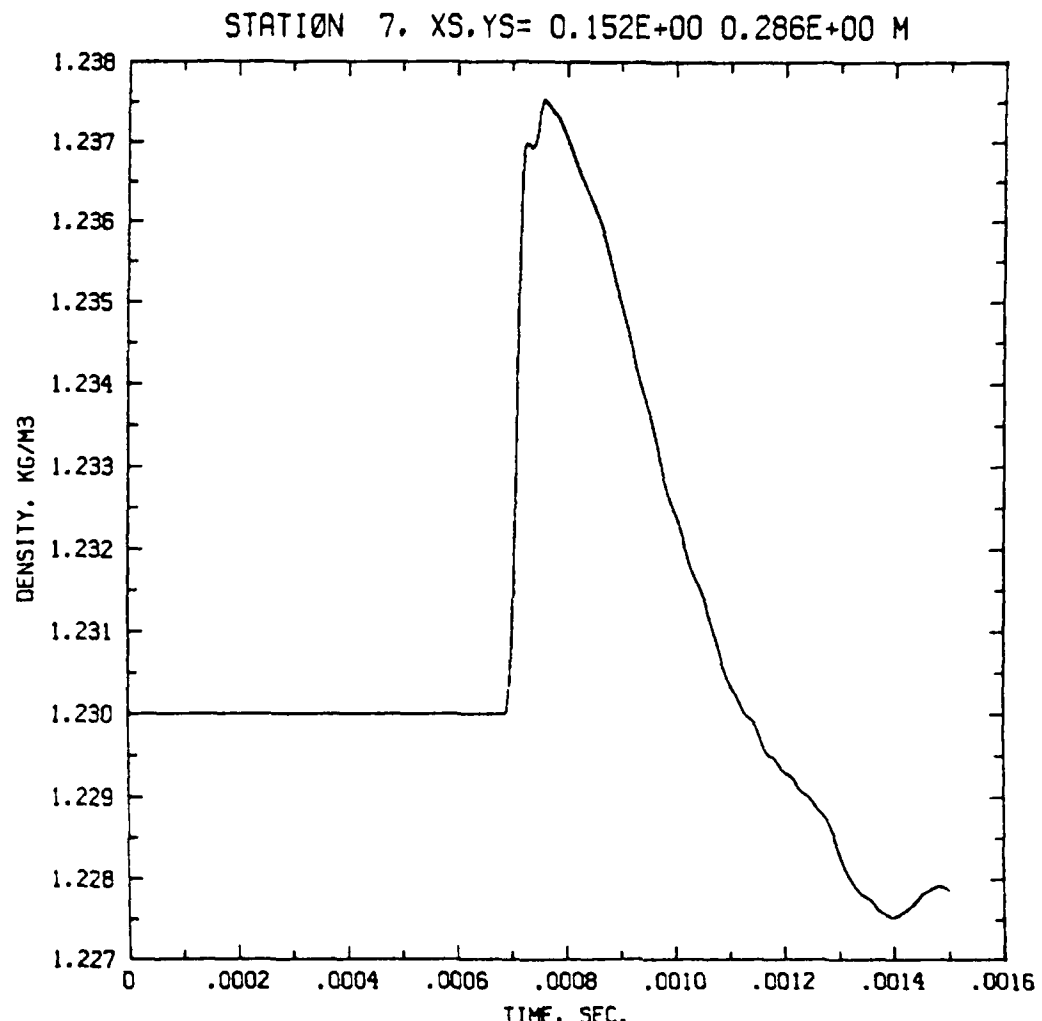
Figure 14c



BLAST DIFFRACTION FROM SHOCK TUBE

7 DUMPS. LAST DUMP IS TUBE00008

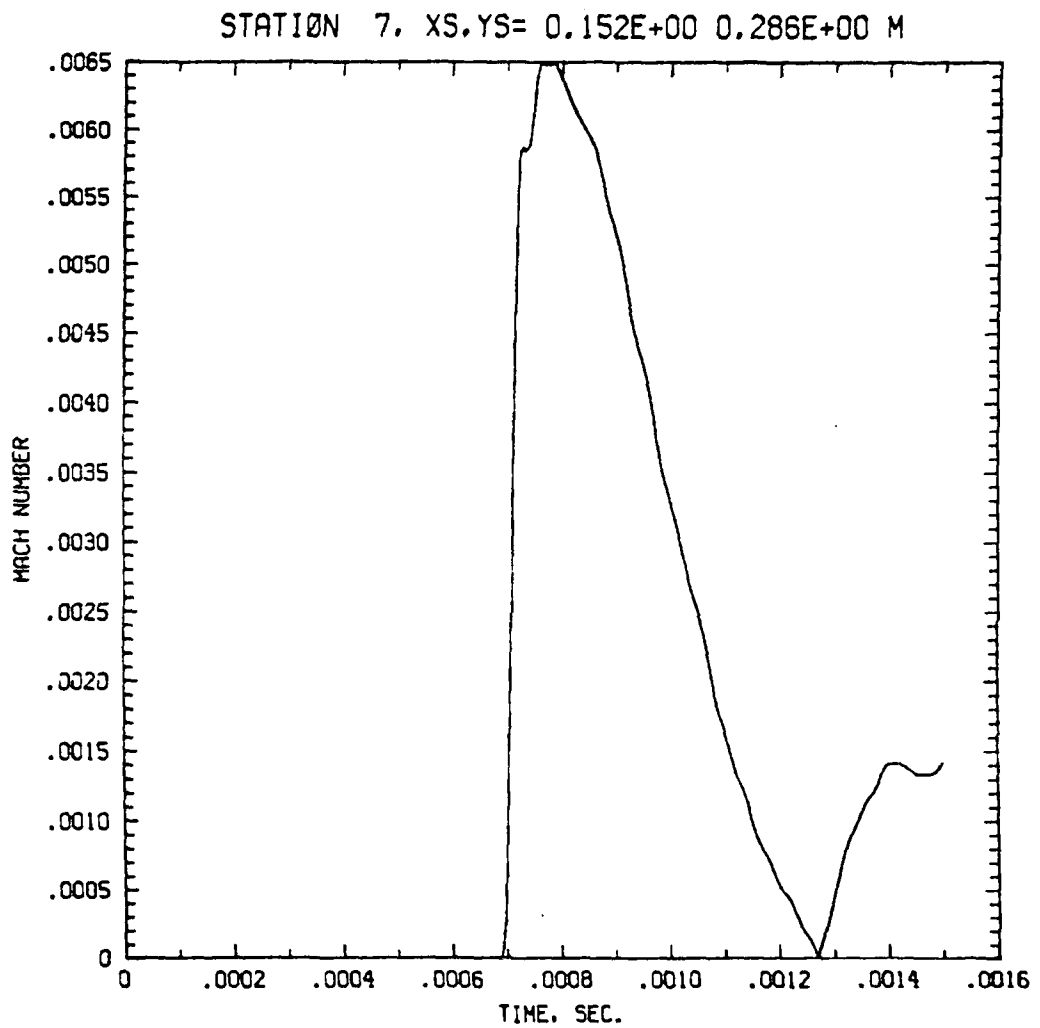
Figure 15a



BLAST DIFFRACTION FROM SHOCK TUBE

7 DUMPS. LAST DUMP IS TUBE0008

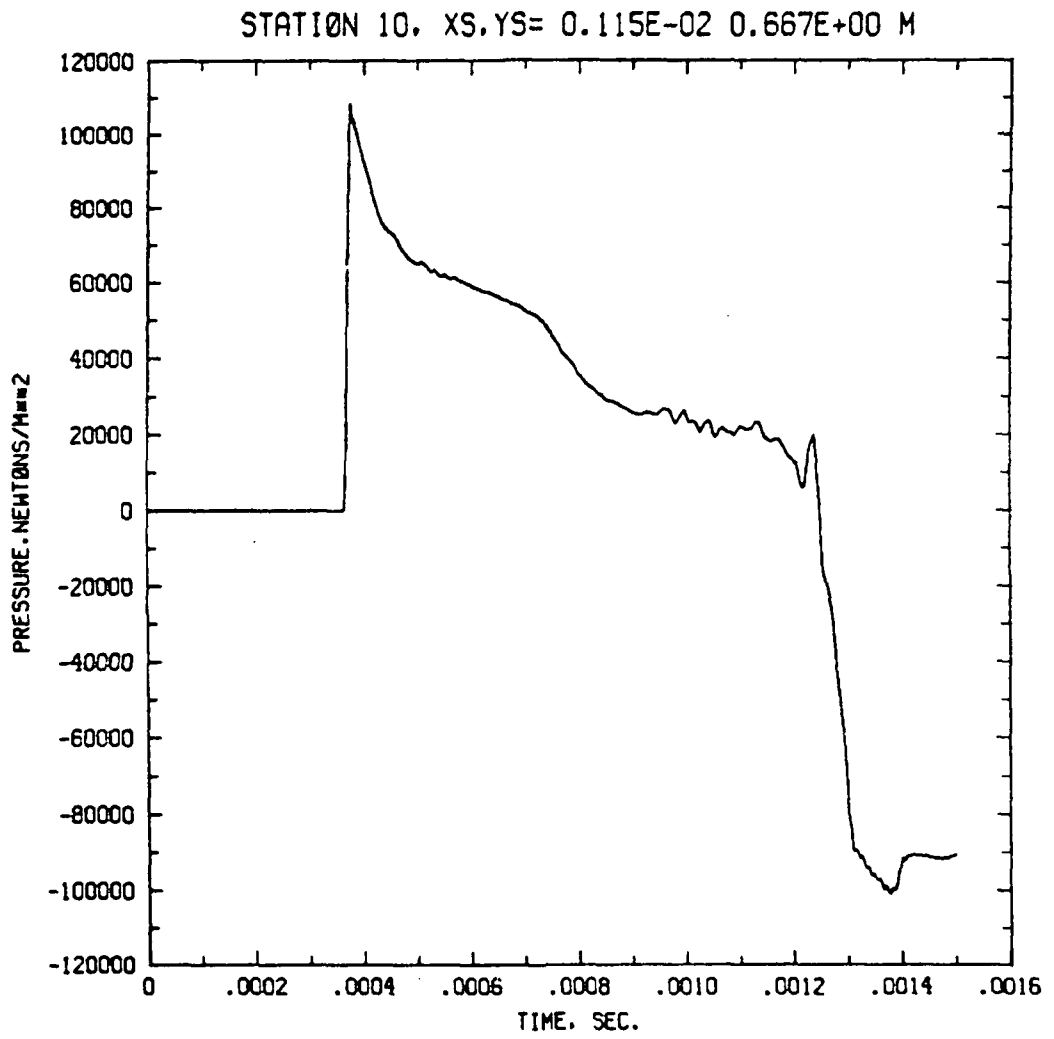
Figure 15b



BLAST DIFFRACTION FROM SHOCK TUBE

7 DUMPS. LAST DUMP IS T1280008

Figure 15c

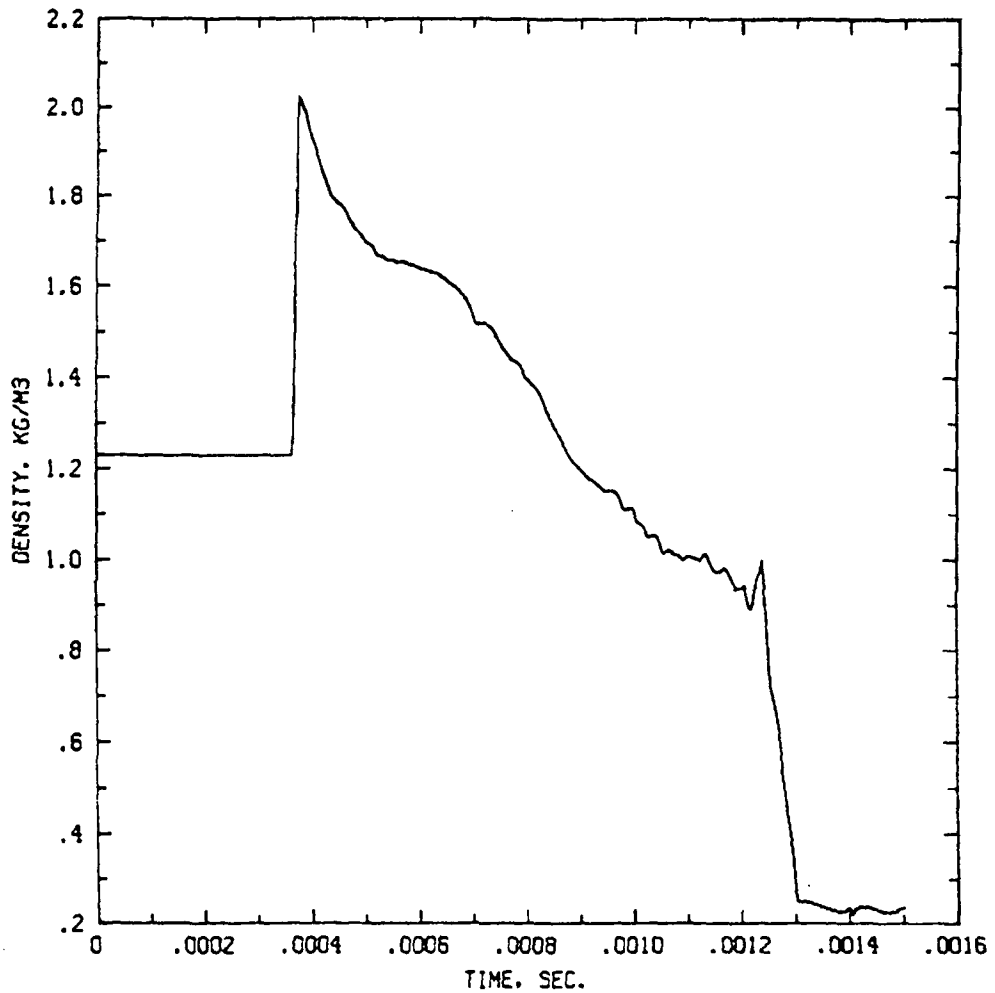


BLAST DIFFRACTION FROM SHOCK TUBE

7 DUMPS. LAST DUMP IS TUBE00008

Figure 16a

STATION 10, XS,YS= 0.115E-02 0.667E+00 M

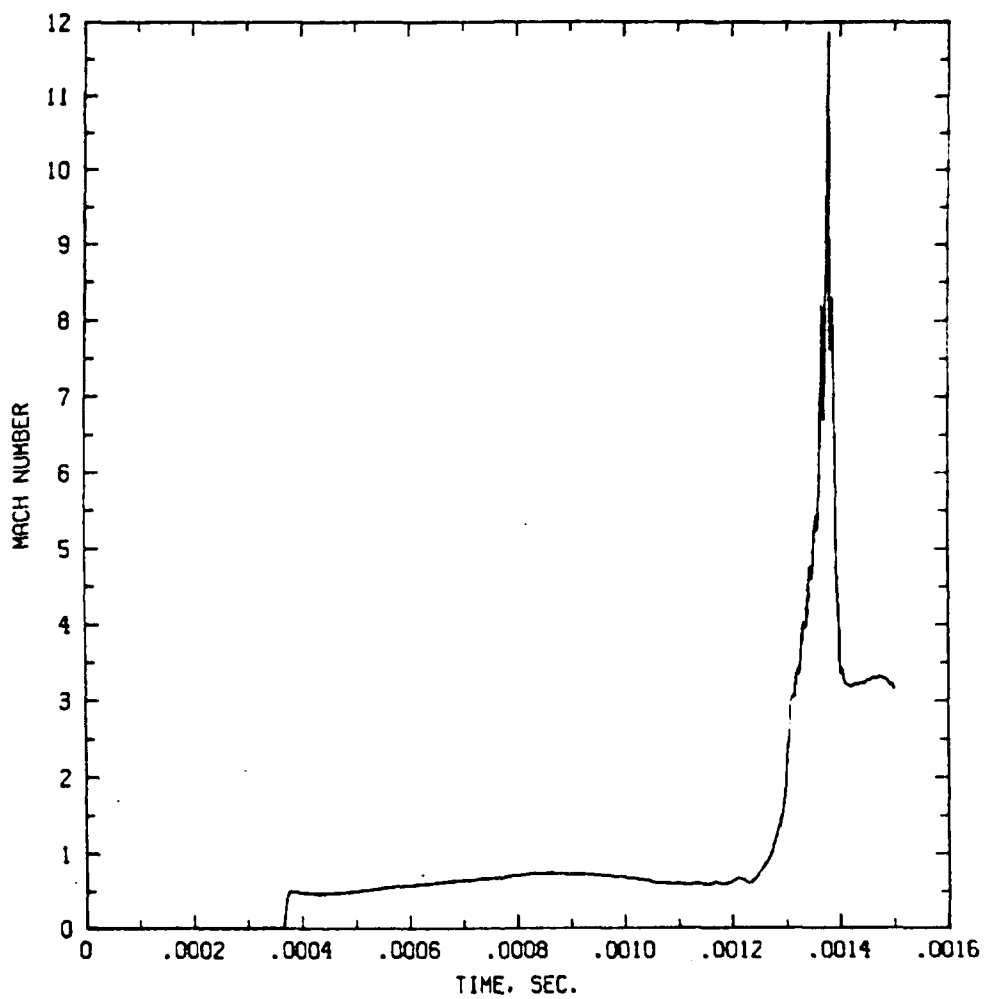


BLAST DIFFRACTION FROM SHOCK TUBE

7 DUMPS. LAST DUMP IS T1.680008

Figure 16b

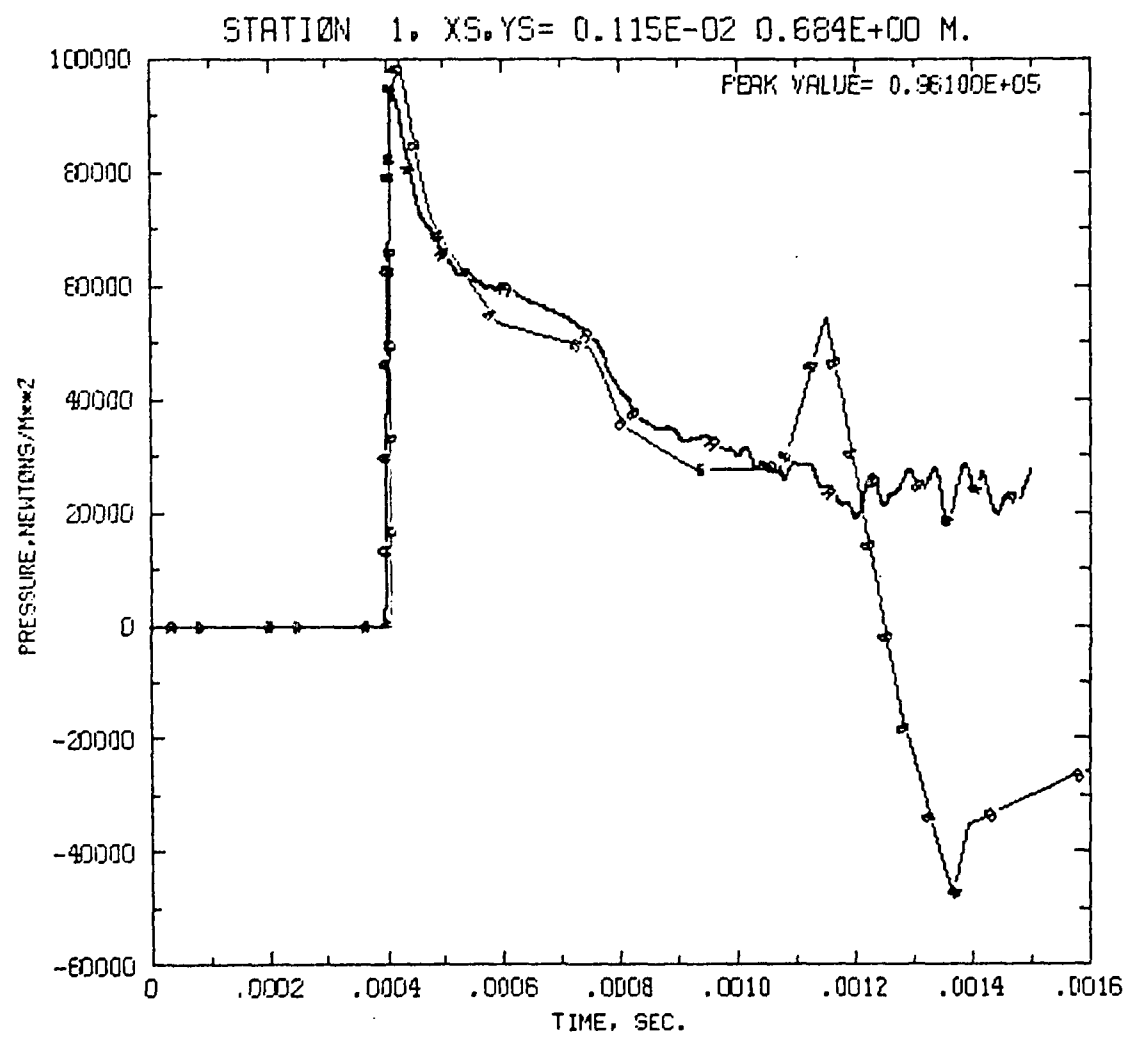
STATION 10, XS,YS= 0.115E-02 0.667E+00 M



BLAST DIFFRACTION FROM SHOCK TUBE

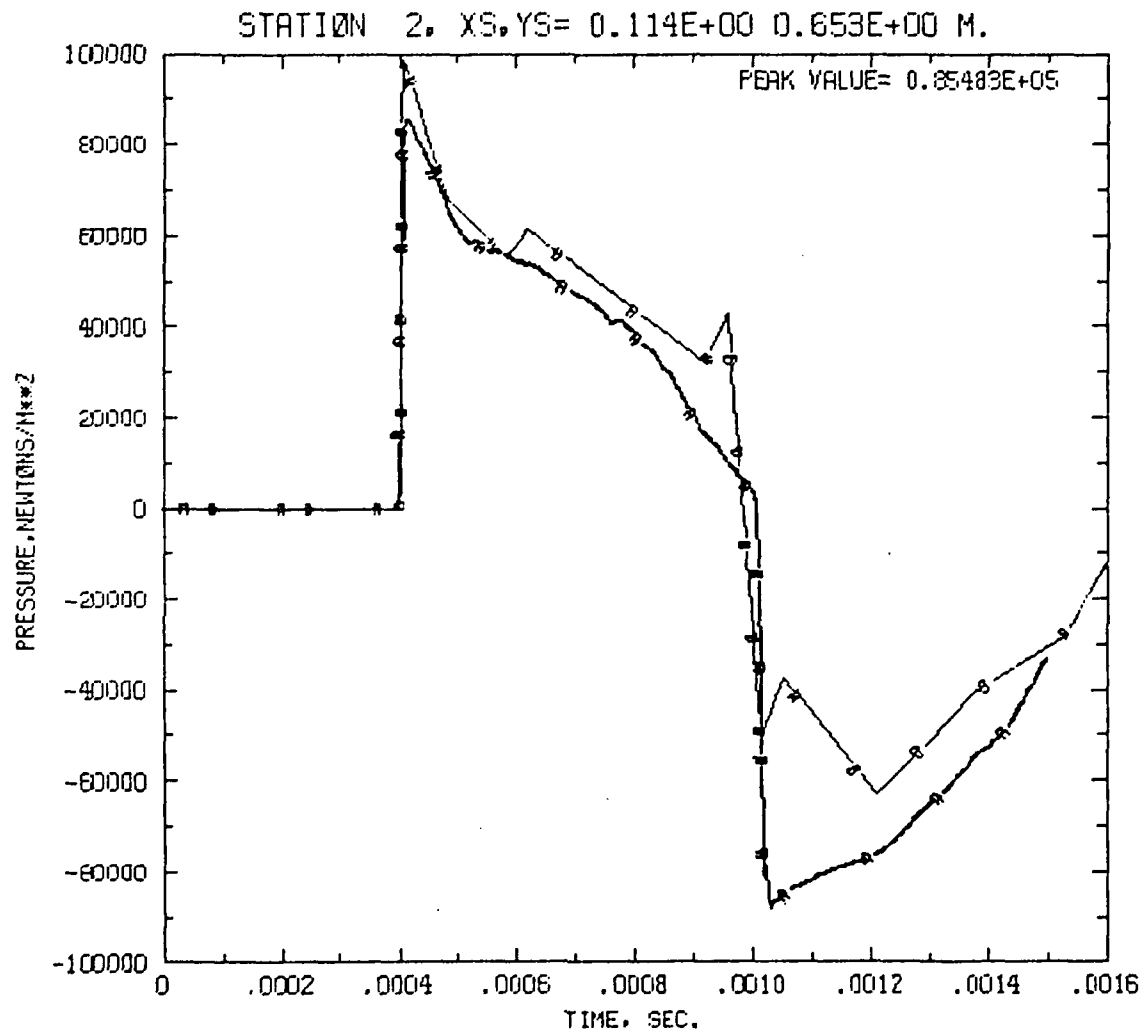
7 DUMPS. LAST DUMP IS T1880008

Figure 16c



BLAST DIFFRACTION FROM SHOCK TUBE  
7 DUMPS, LAST DUMP IS TUBB0006

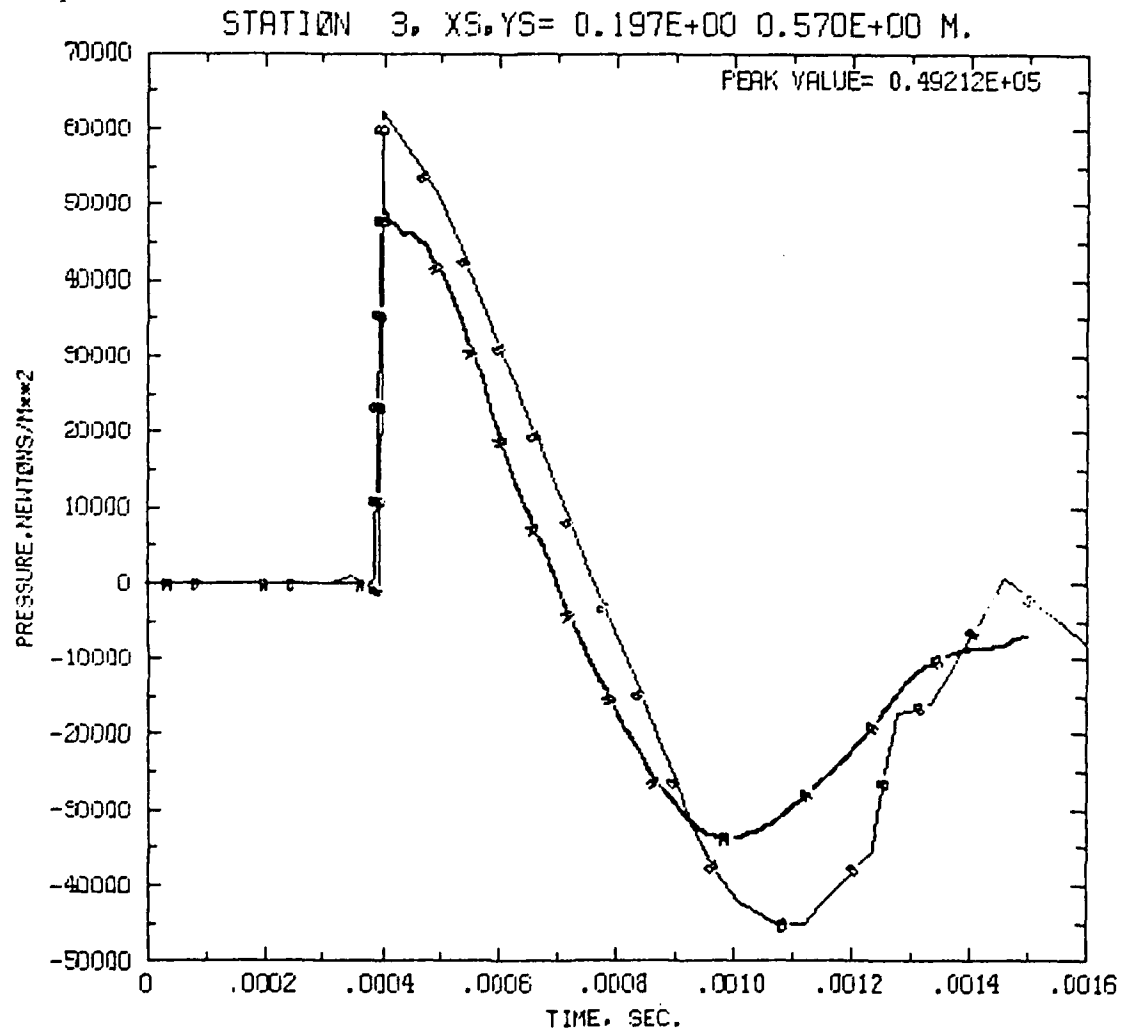
Figure 17



### BLAST DIFFRACTION FROM SHOCK TUBE

7 DUMPS, LAST DUMP IS TUBE0008

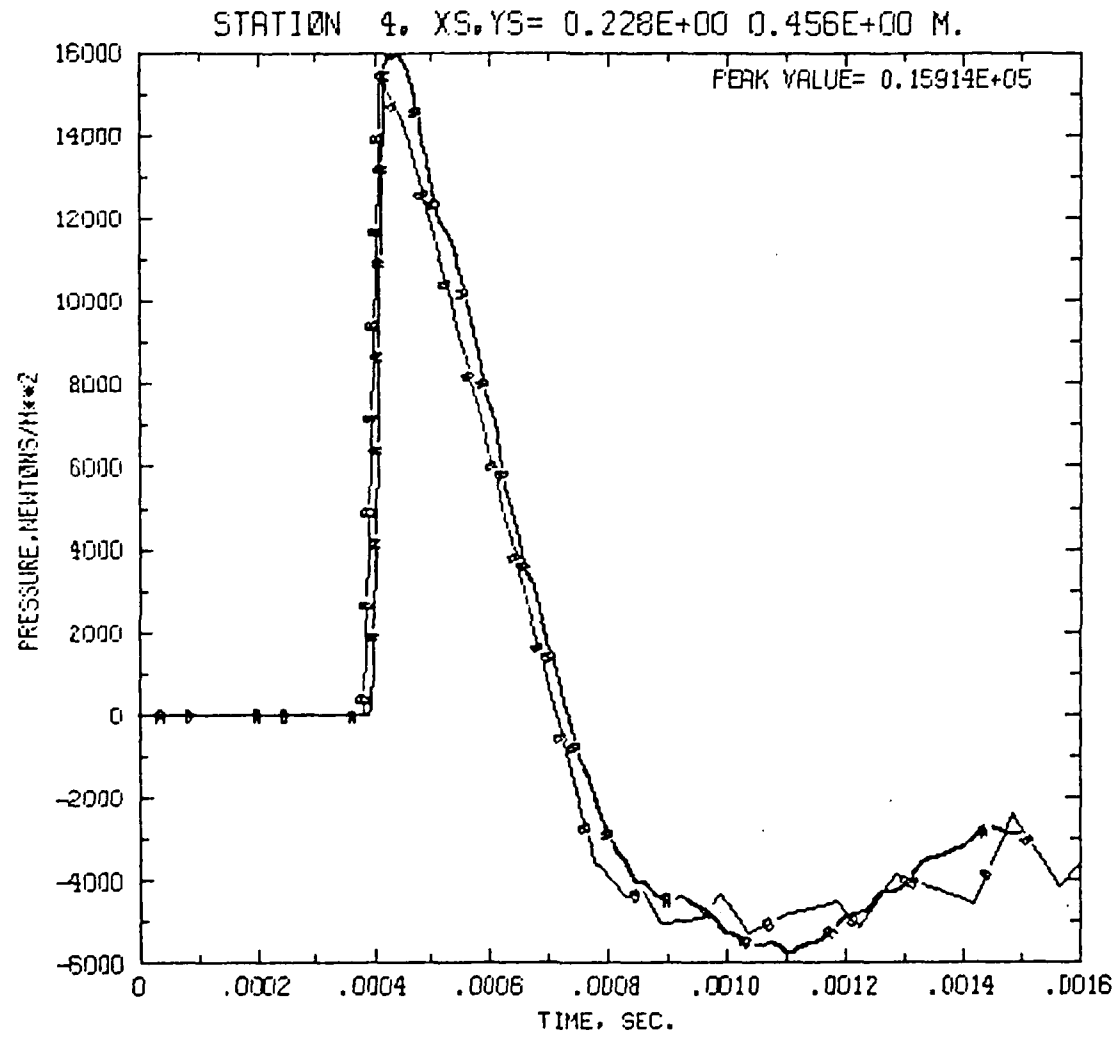
Figure 18



BLAST DIFFRACTION FROM SHOCK TUBE

7 DUMPS, LAST DUMP IS TUBE0008

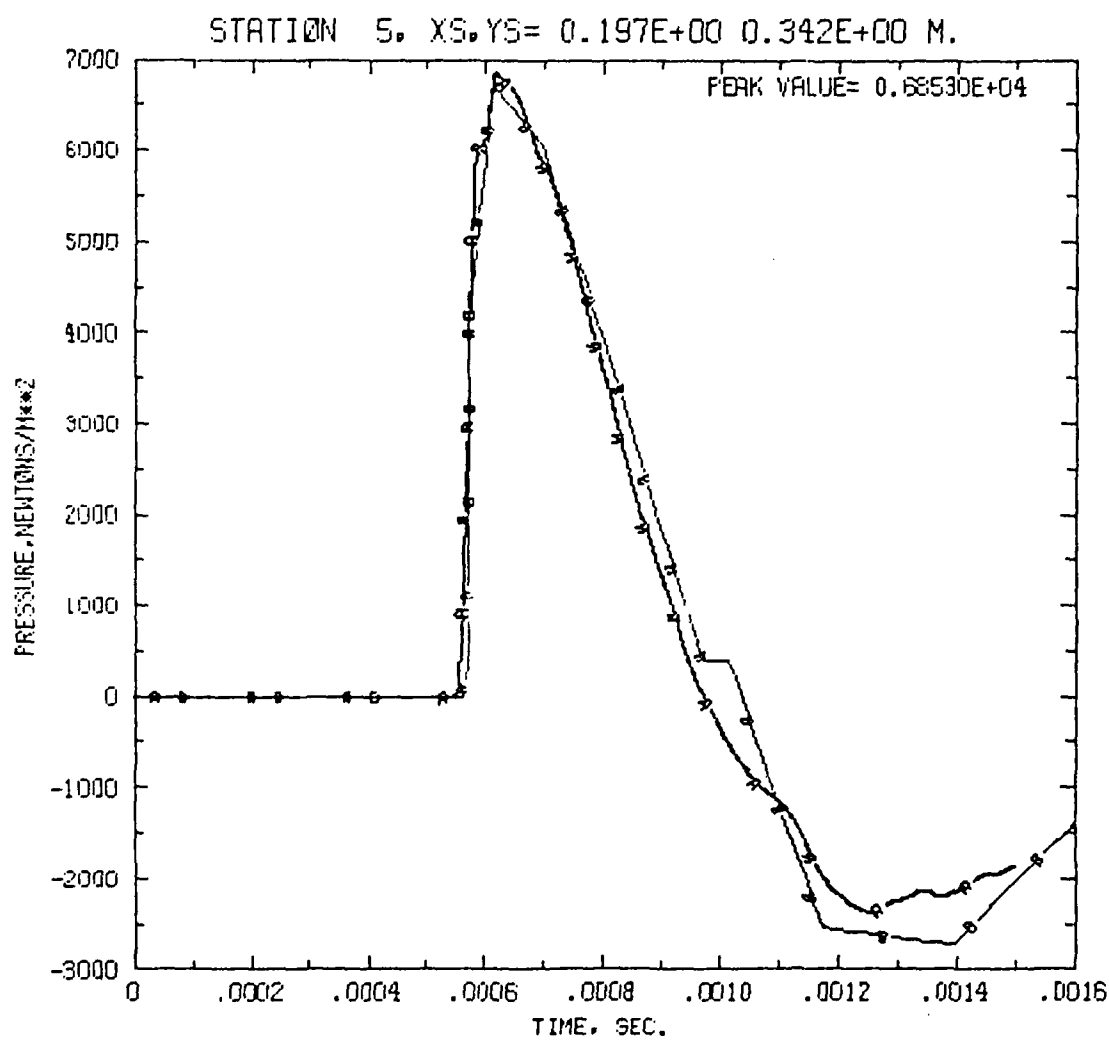
Figure 19



BLAST DIFFRACTION FROM SHOCK TUBE

7 DUMPS, LAST DUMP IS TUBE0006

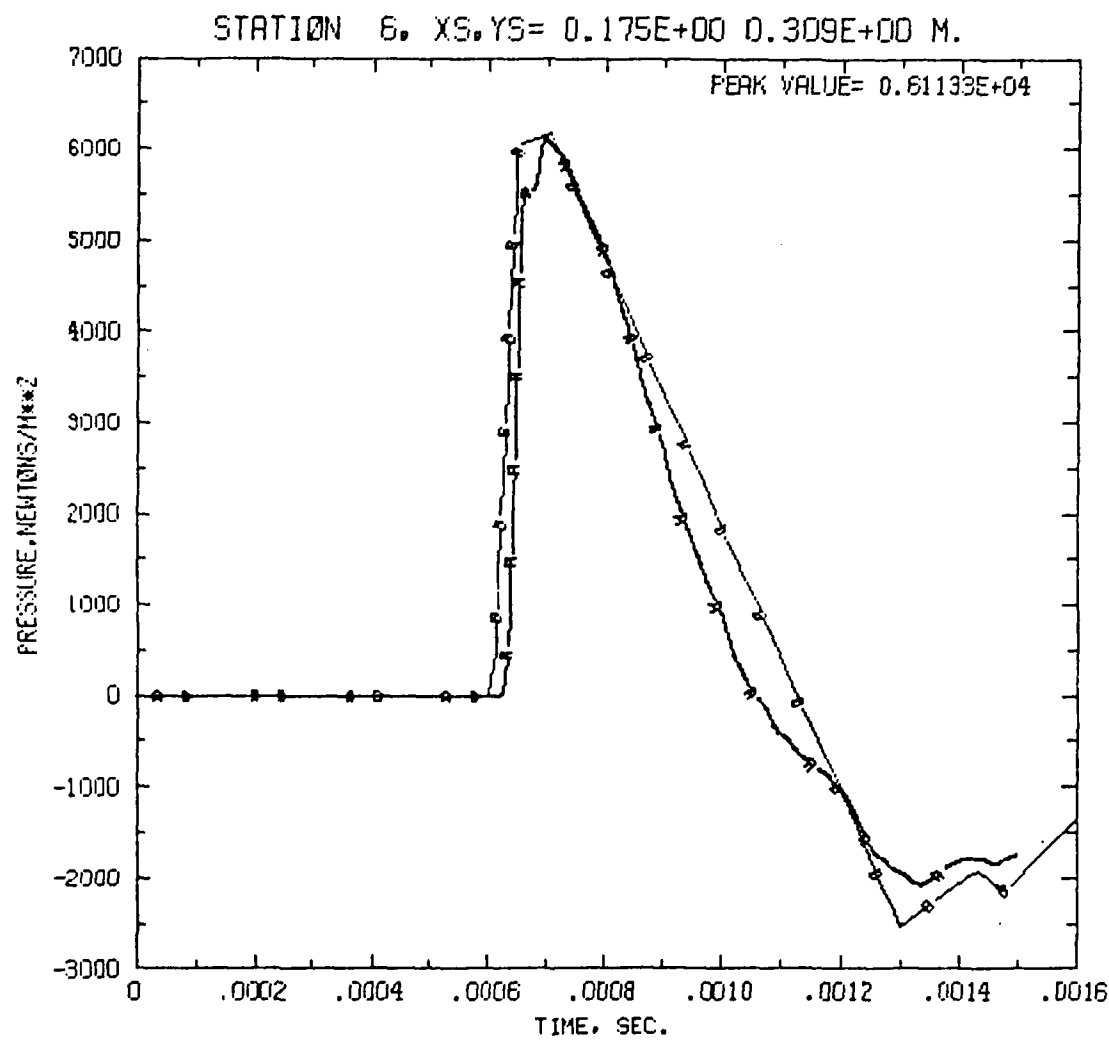
Figure 20



BLAST DIFFRACTION FROM SHOCK TUBE

7 DUMPS, LAST DUMP IS TUBE0006

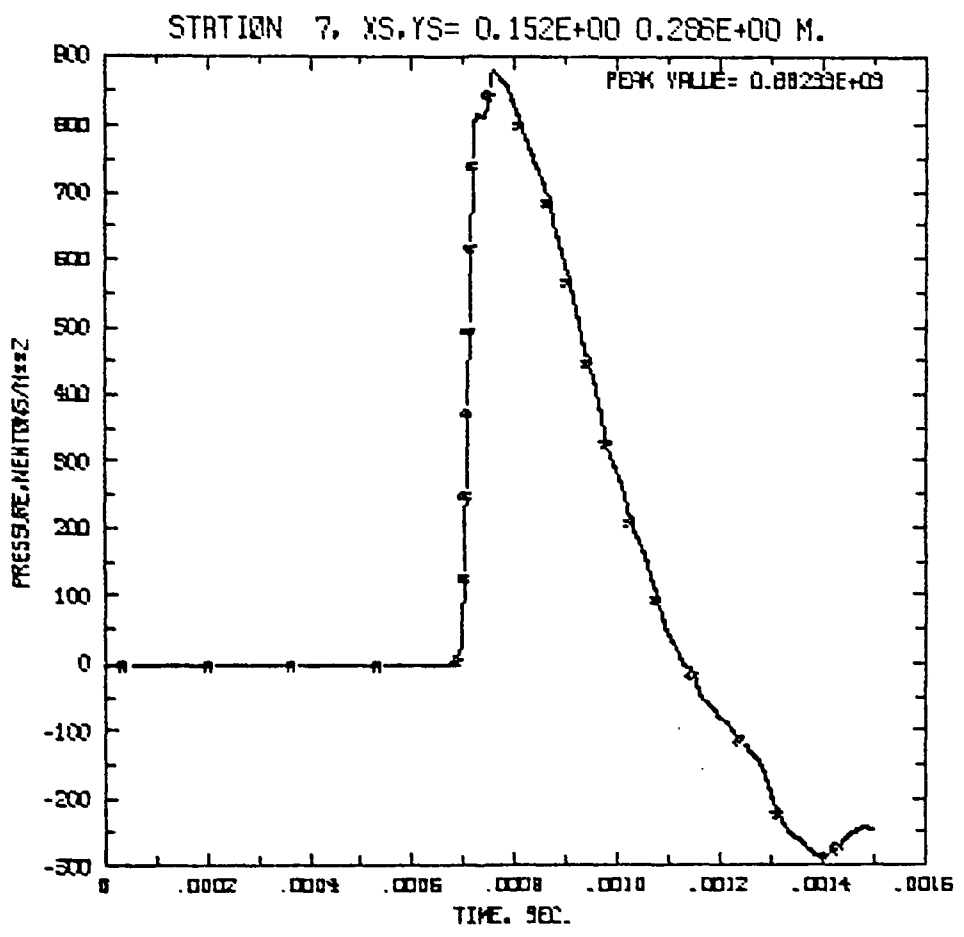
Figure 21



BLAST DIFFRACTION FROM SHOCK TUBE

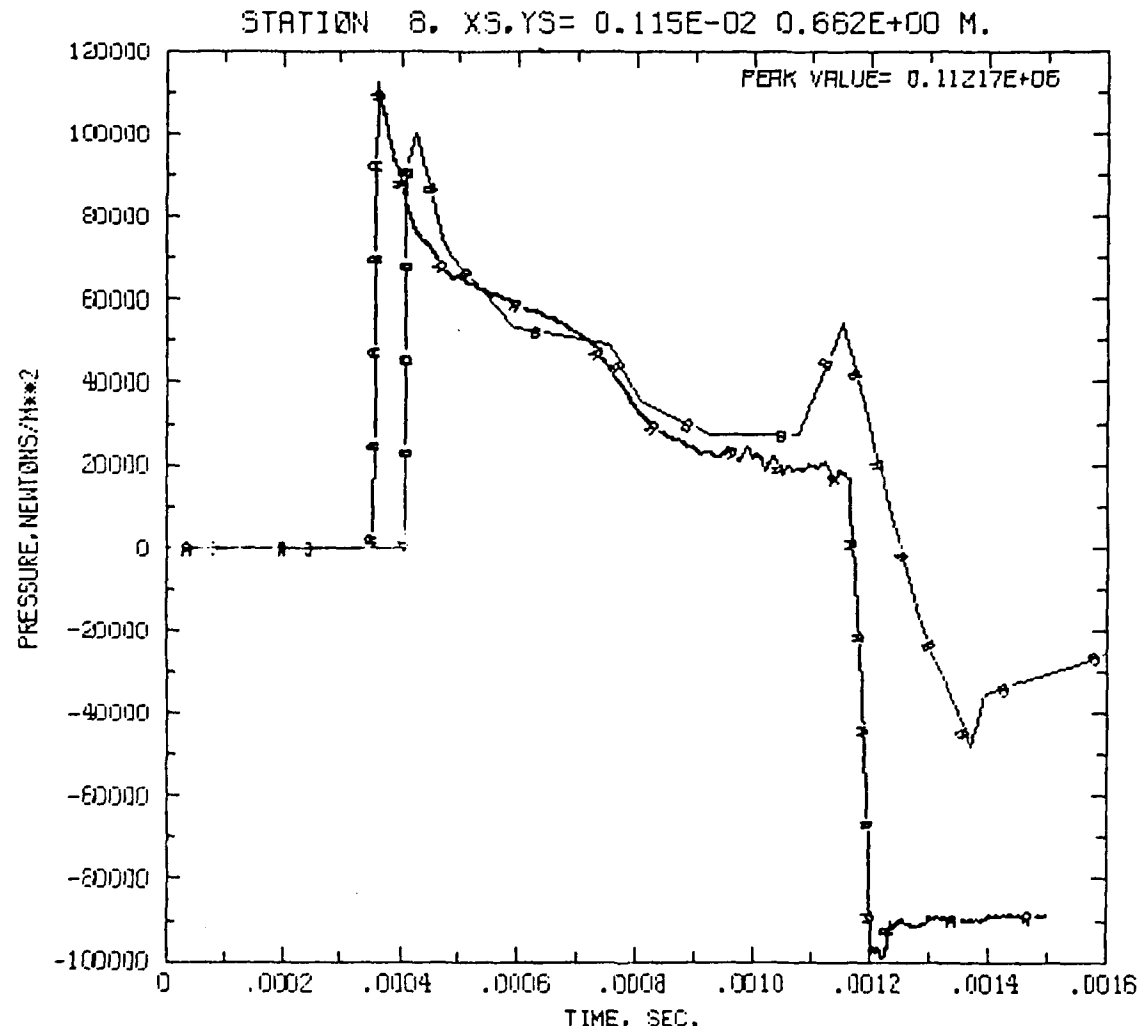
7 DUMPS, LAST DUMP IS TUBE0008

Figure 22



BLAST DIFFRACTION FROM SHOCK TUBE  
7 DUMPS. LAST DUMP IS TUBB0008

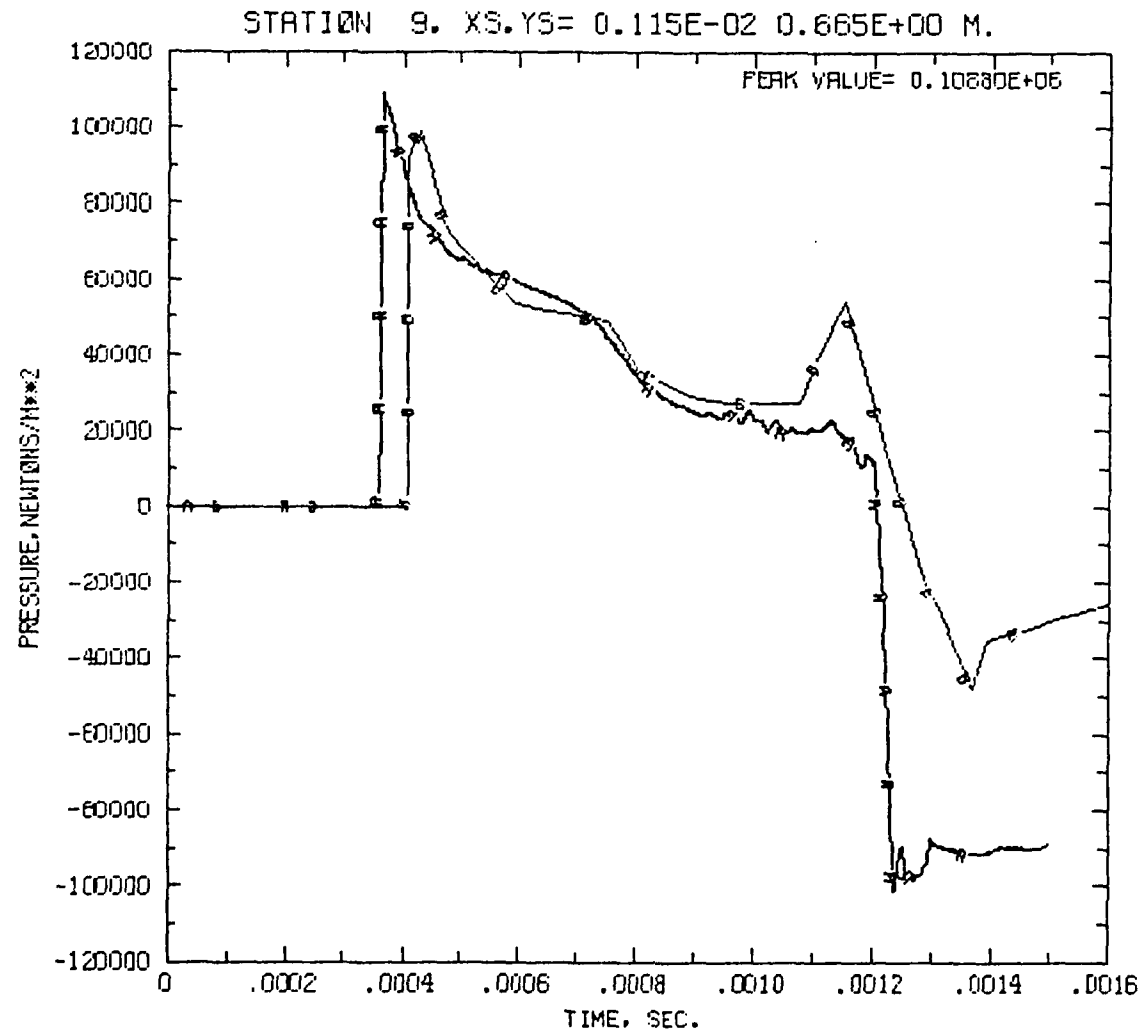
Figure 23



BLAST DIFFRACTION FROM SHOCK TUBE

7 DUMPS, LAST DUMP IS TUBE0008

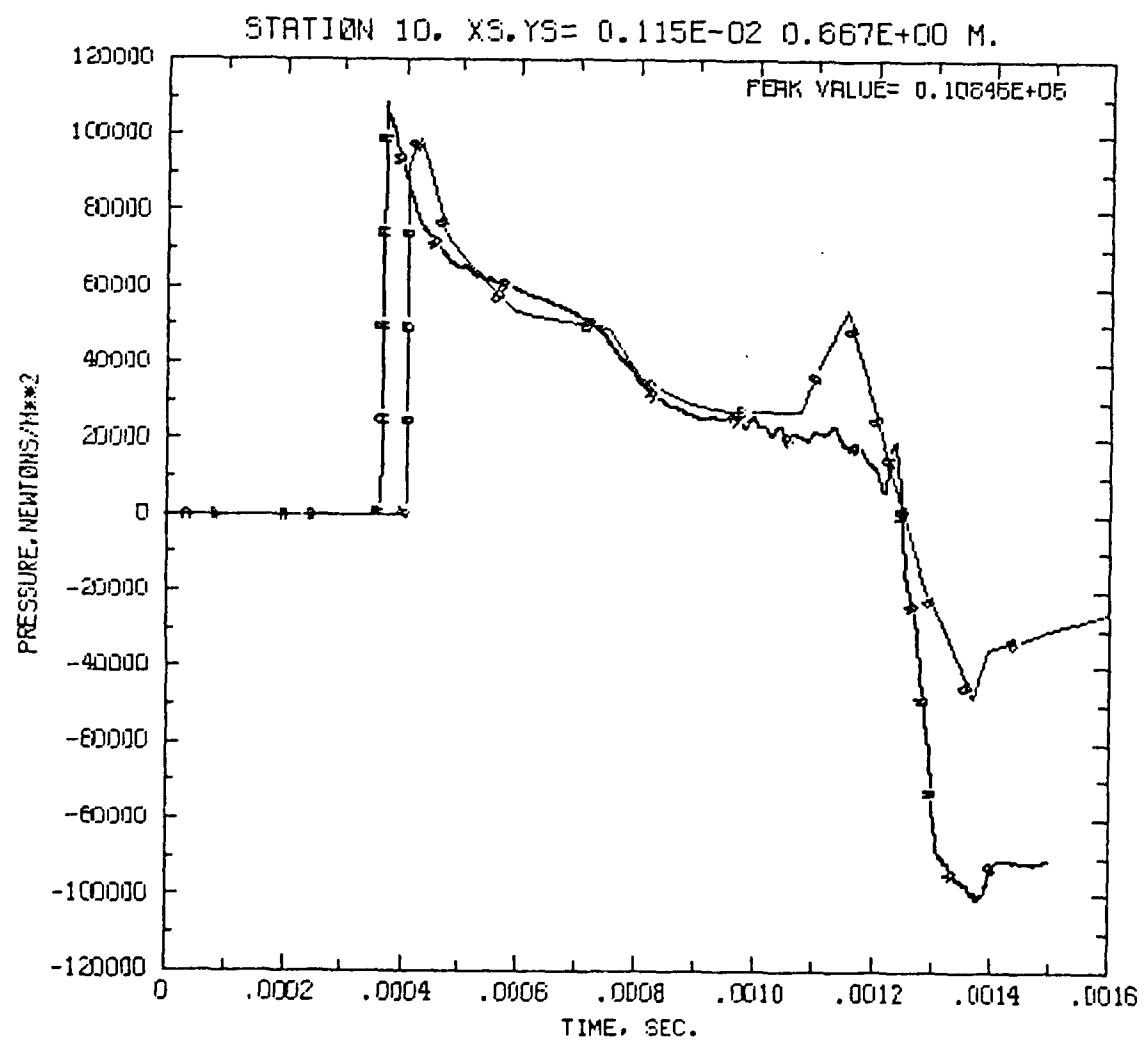
Figure 24



BLAST DIFFRACTION FROM SHOCK TUBE

7 DUMPS, LAST DUMP IS TUBE0006

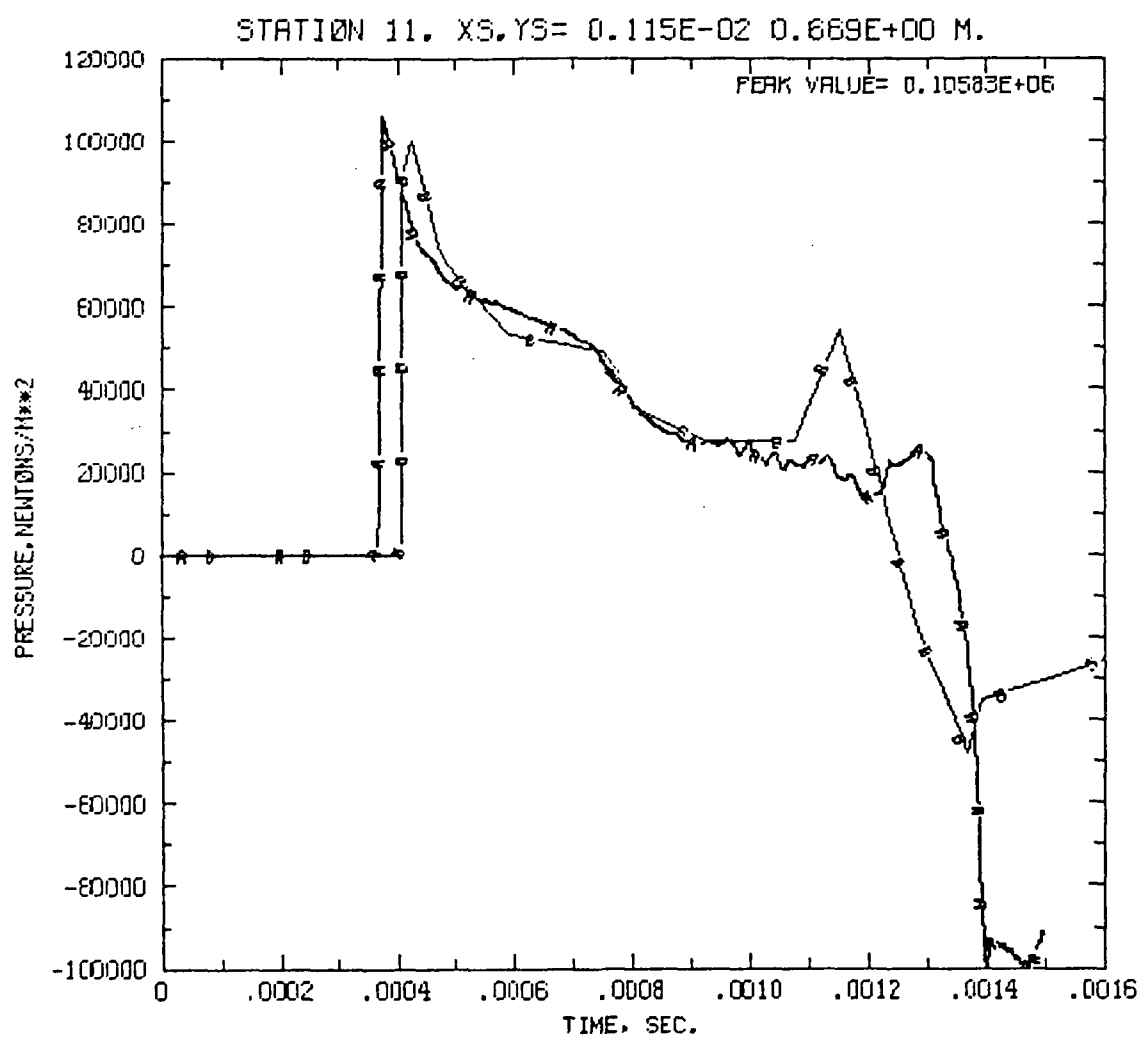
Figure 25



BLAST DIFFRACTION FROM SHOCK TUBE

7 DUMPS, LAST DUMP IS TUEB0008

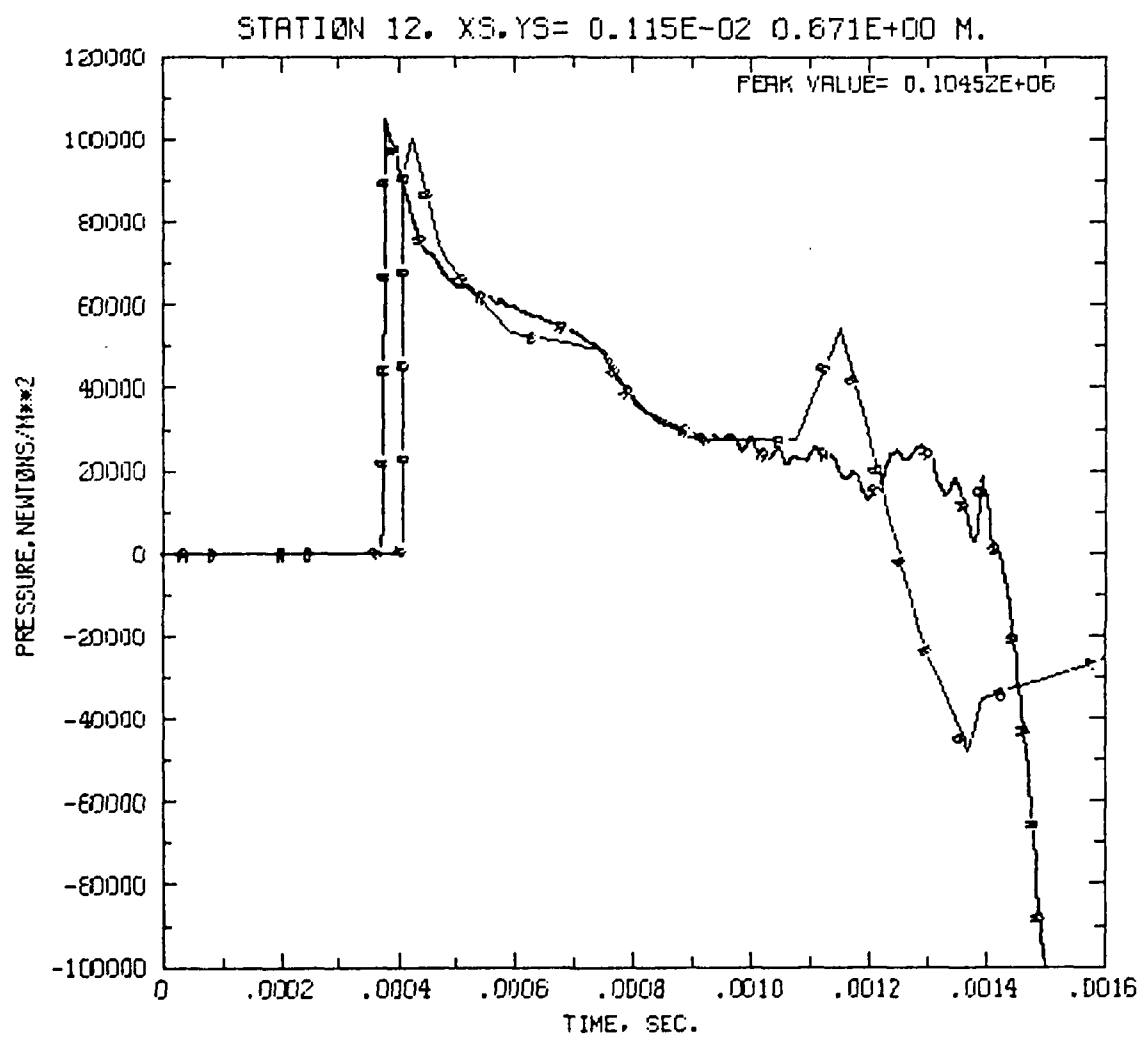
Figure 26



BLAST DIFFRACTION FROM SHOCK TUBE

7 DUMPS, LAST DUMP IS TUBB0006

Figure 27



BLAST DIFFRACTION FROM SHOCK TUBE

7 DUMPS. LAST DUMP IS TUBE0008

Figure 28

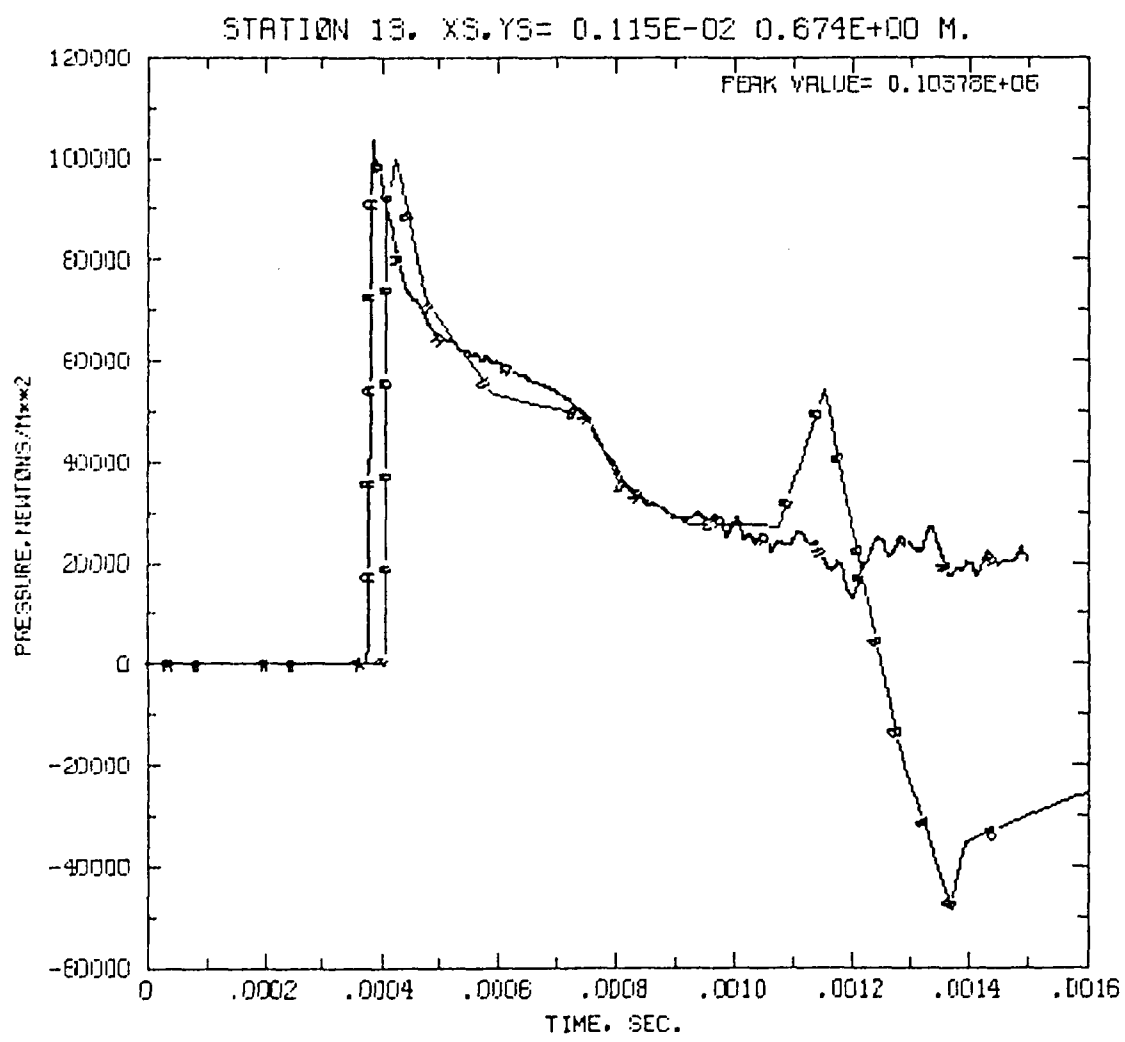


Figure 29

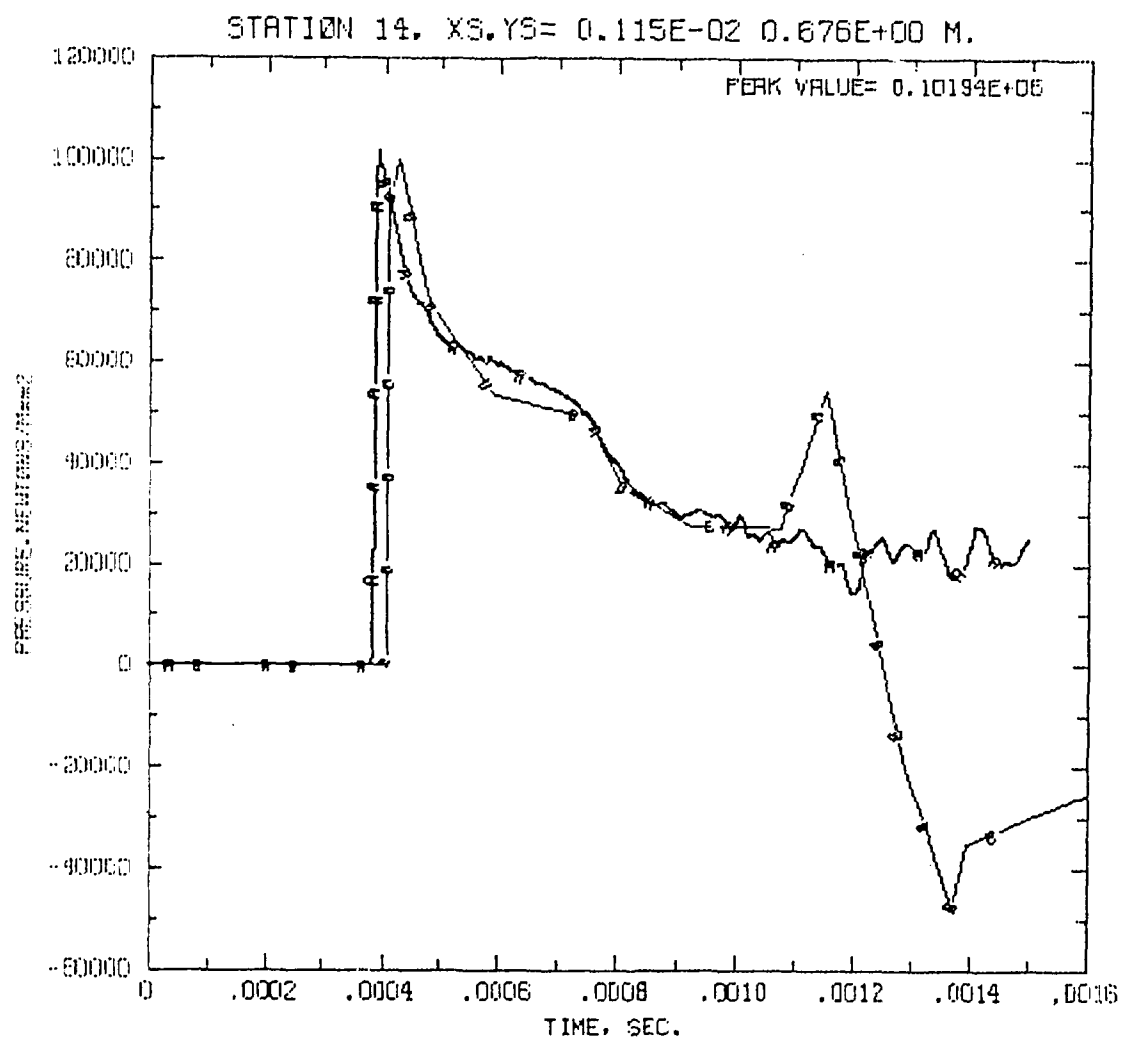
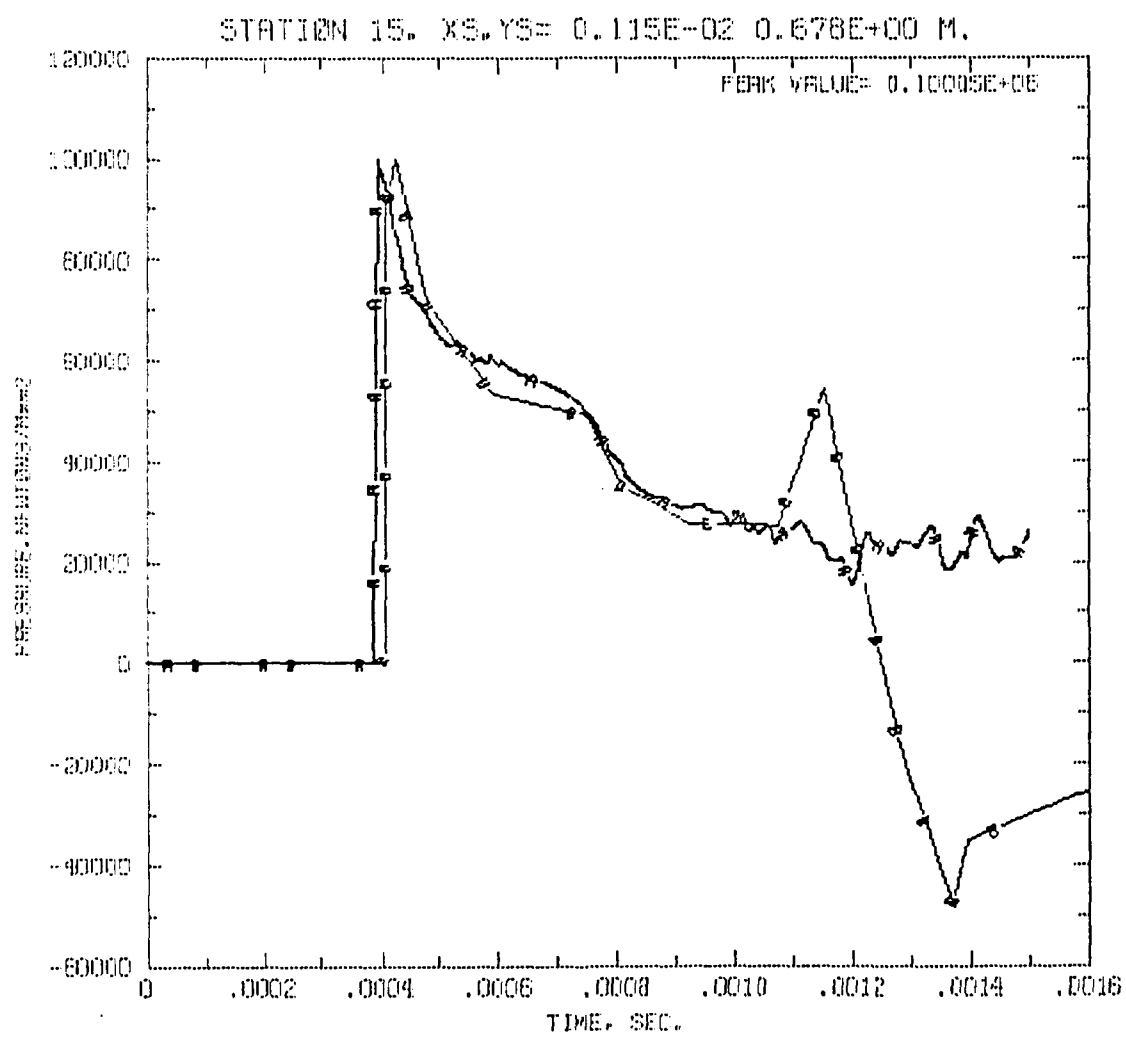
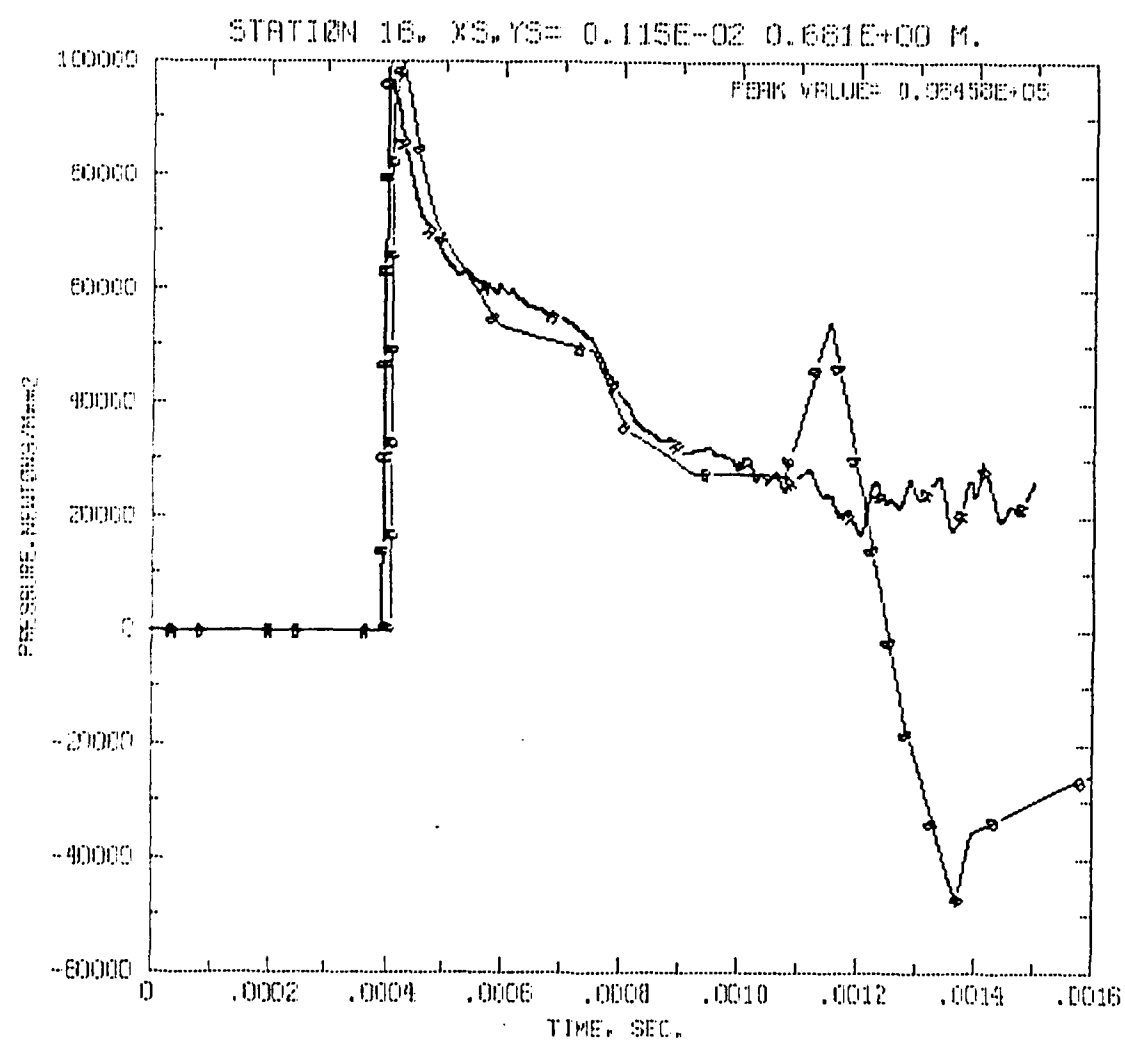


Figure 30



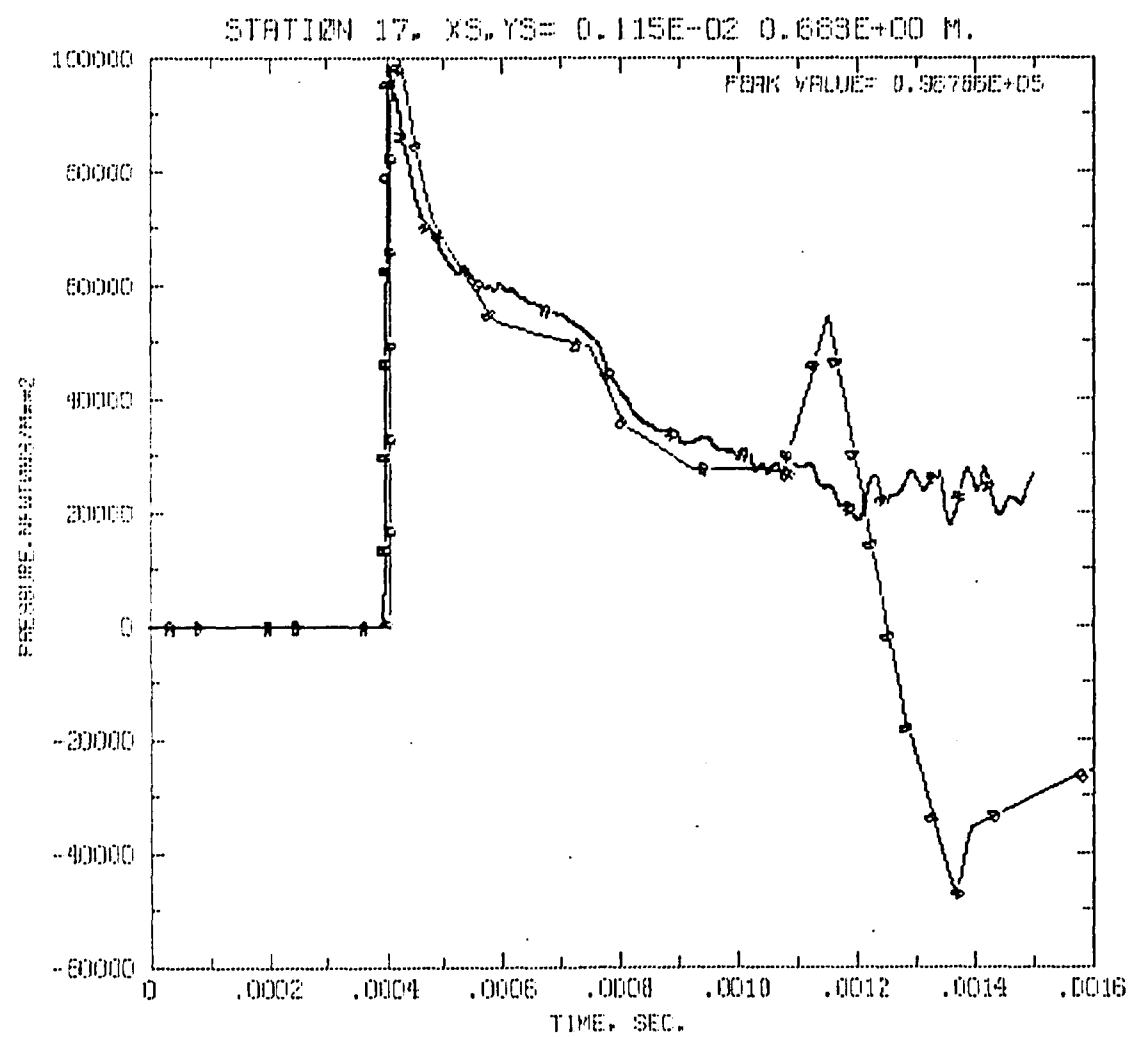
BLAST DIFFRACTION FROM SHOCK TUBE  
7 DUMPS, LAST DUMP 13 TUBB0008

Figure 31



BLAST DIFFRACTION FROM SHOCK TUBE  
7 DUMPS, LAST DUMP IS TUBB00008

Figure 32



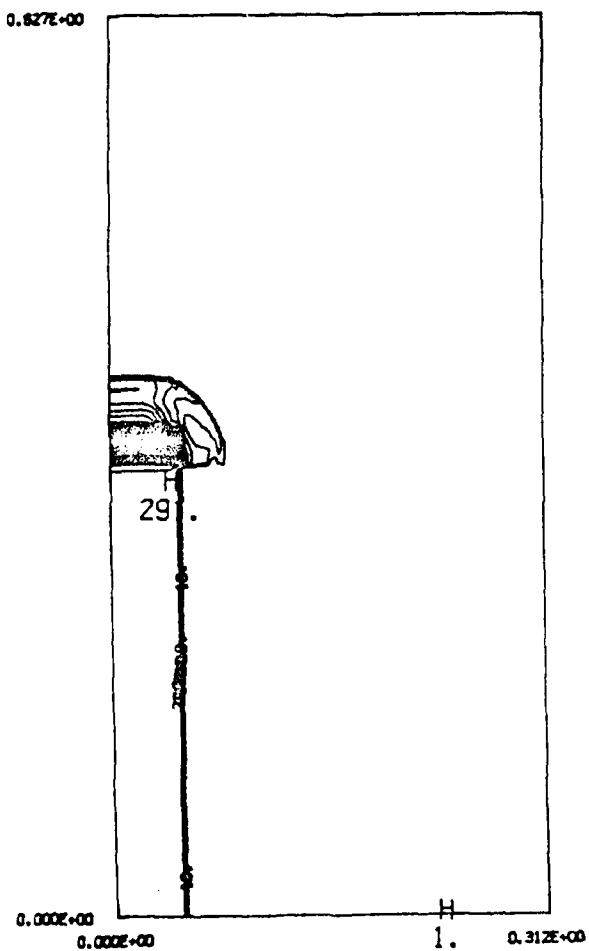
BLAST DIFFRACTION FROM SHOCK TUBE

7 DUMPS, LAST DUMP 13 TUBB0008

Figure 33

105 MM HOWITZER MUZZLE FLOW

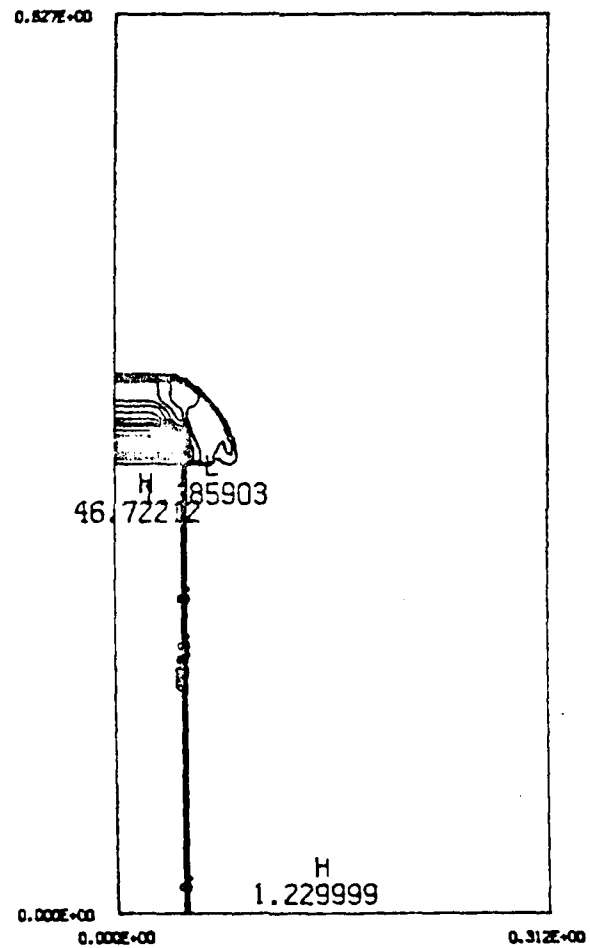
TIME= 0.25352E-04 SEC., STEP 89, DUMP HOW0001 PRESSURE, NEWTONS/M==2



CENTEUR FROM 0.00000 TO 0.28000E-03 CENTEUR INTERVAL OF 0.10000E-07 PT 12.346 0.28100E-03 UNITS ARE SCALLED BY 0.10000E-04

Figure 34a

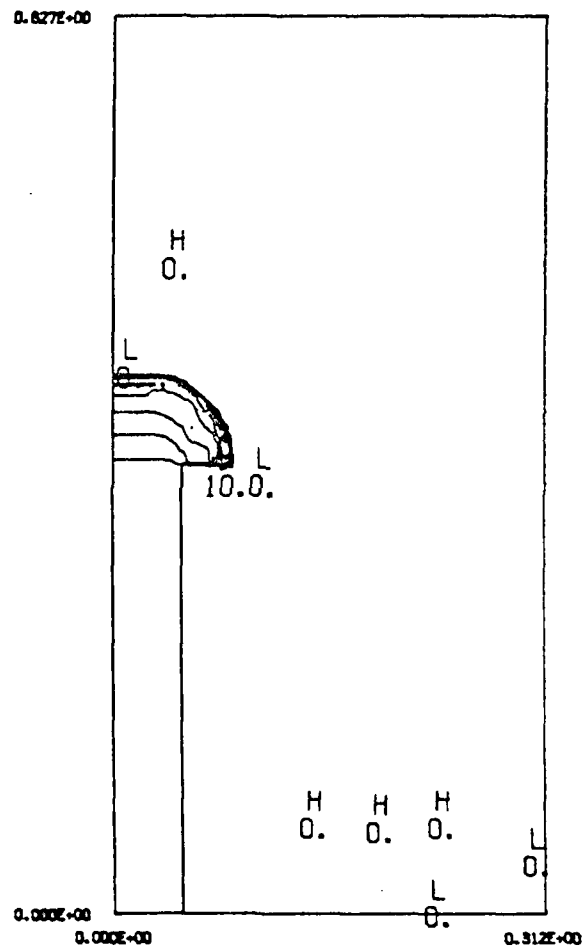
105 MM HOWITZER MUZZLE FLOW  
TIME= 0.25352E-04 SEC.. STEP 89. DUMP H2NZ0001 DENSITY 1. KG/M3



CONTOUR FROM 0.00000 TO 46.000 CONTOUR INTERVAL OF 2.0000 PT(3-3)= 46.722

Figure 34b

105 MM HOWITZER MUZZLE FLOW  
TIME= 0.25352E-04 SEC.. STEP 89. DUMP H0WZ0001 MACH NUMBER



CONTOUR PRTYP 0.00000 T8 8.0000 CONTOUR INTERVAL OF 0.60000 PT13-21= 1.1294

Figure 34c

105 MM HOWITZER MUZZLE FLOW  
TIME= 0.25352E-04 SEC.. STEP 69. DUMP H0WZ0001 VELOCITY. M/SEC

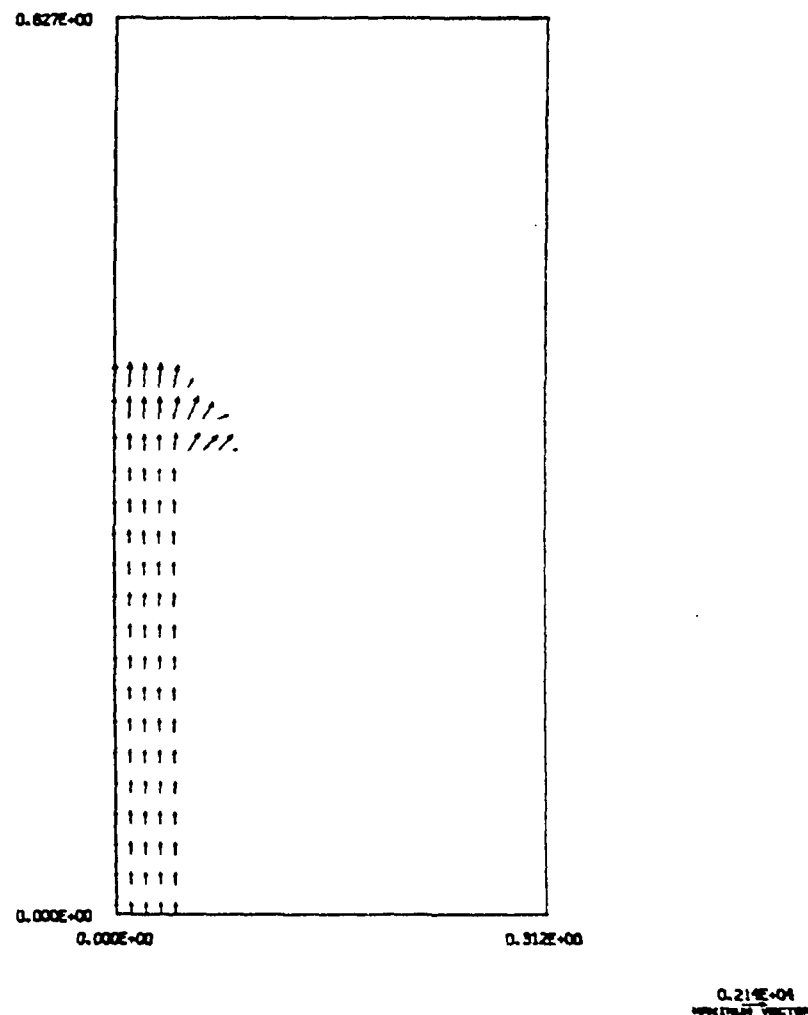
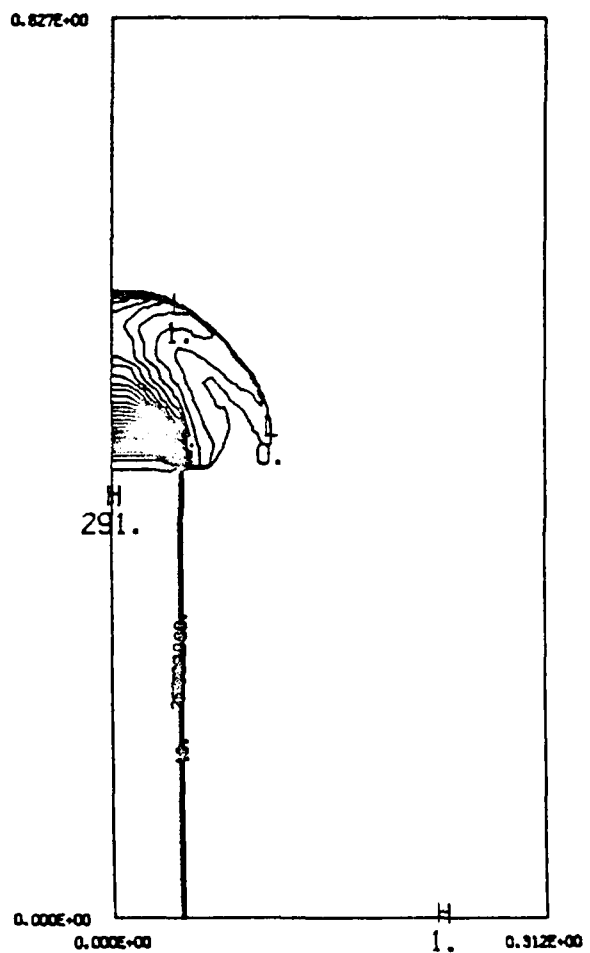


Figure 34d

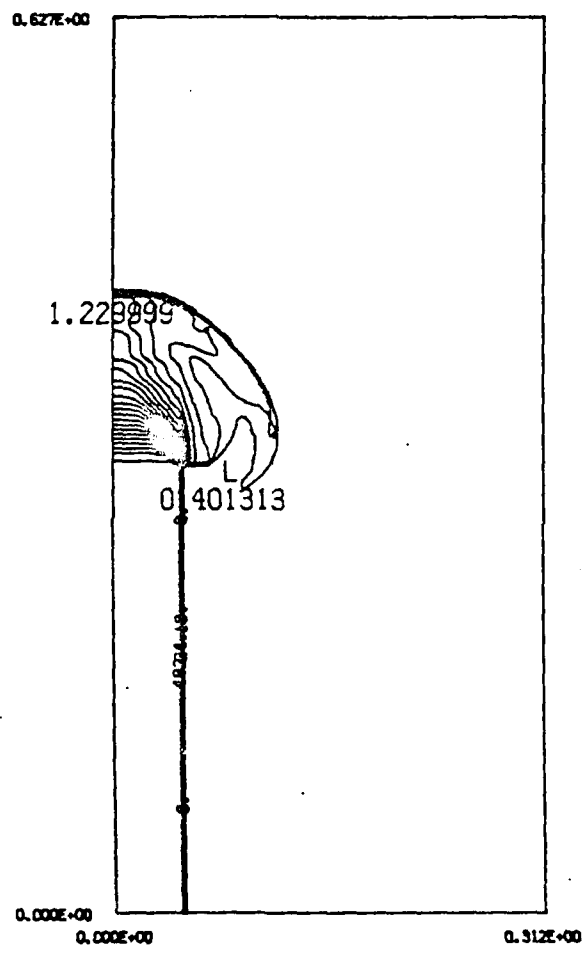
105 MM HOWITZER MUZZLE FLOW  
TIME= 0.50452E-04 SEC., STEP 143, DUMP HOWZ0002 PRESSURE, NEWTONS/M\*\*2



CONTOUR FROM 0.00000 TO 0.28000E-08 CONTOUR INTERVAL OF 0.10000E-07 PT13-S1= 0.28100E-08 LABELS SCALING BY 0.10000E-04

Figure 35a

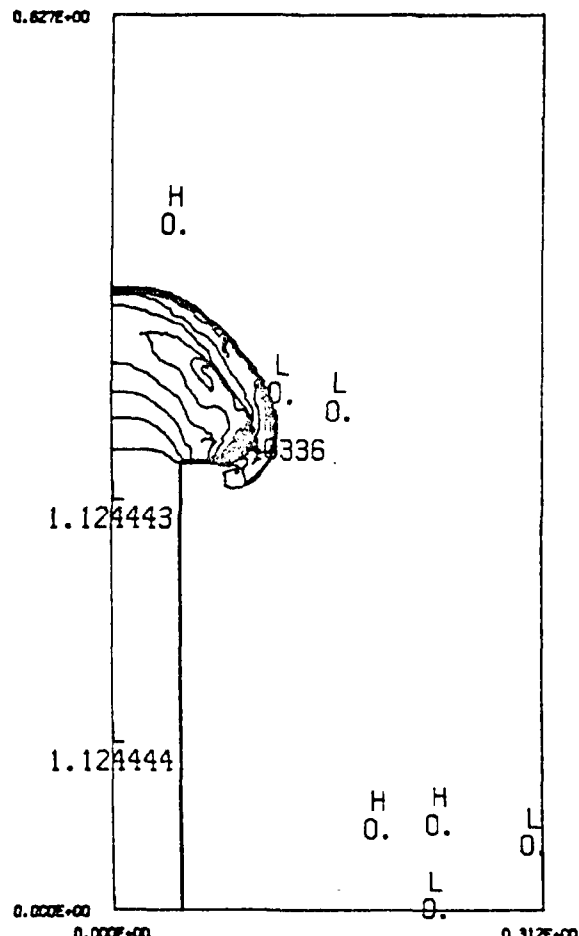
105 MM HOWITZER MUZZLE FLOW  
TIME= 0.50452E-04 SEC., STEP 143, DUMP HOWZ0002 DENSITY 1. KG/M3



CONTOUR FROM 0.0000 TO 06.000 CONTOUR INTERVAL OF 2.0000 PT/SL.3D= 06.722

Figure 35b

105 MM HOWITZER MUZZLE FLOW  
TIME= 0.50452E-04 SEC., STEP 143, DUMP HOWZ0002 MACH NUMBER

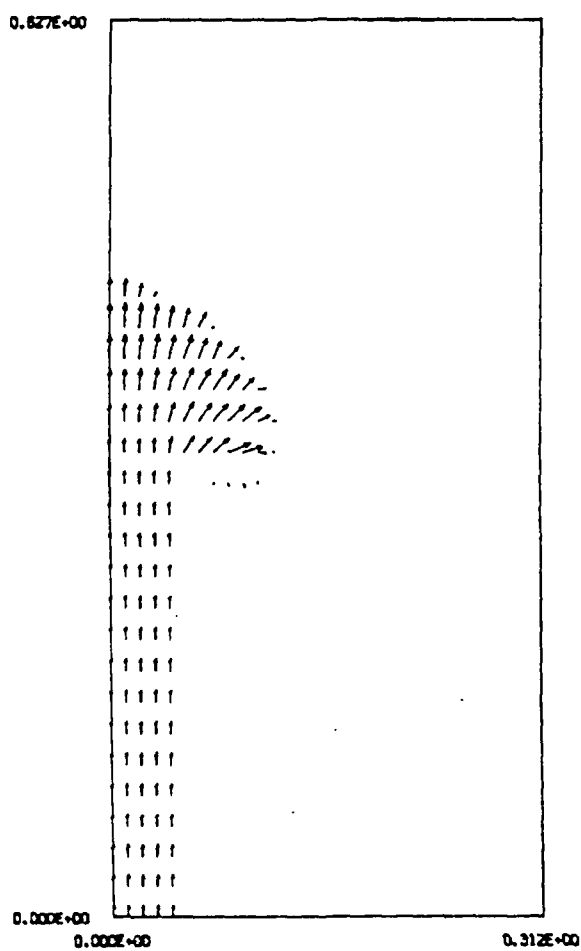


CONTOUR FROM 0.00000 TO 7.20000 CONTOUR INTERVAL OF 0.40000 PT(1,2)= 1.1244

Figure 35c

105 MM HOWITZER MUZZLE FLOW

TIME= 0.50452E-04 SEC., STEP 143, DUMP HOWZ0002 VELOCITY, M/SEC

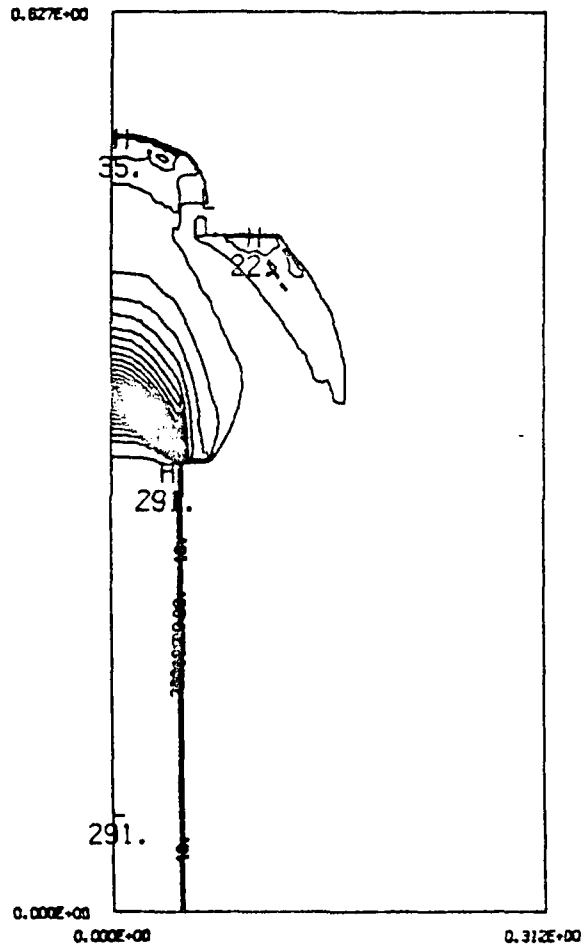


0.217E+04  
PERPENDICULAR VECTOR

Figure 35d

105 MM HOWITZER MUZZLE FLOW

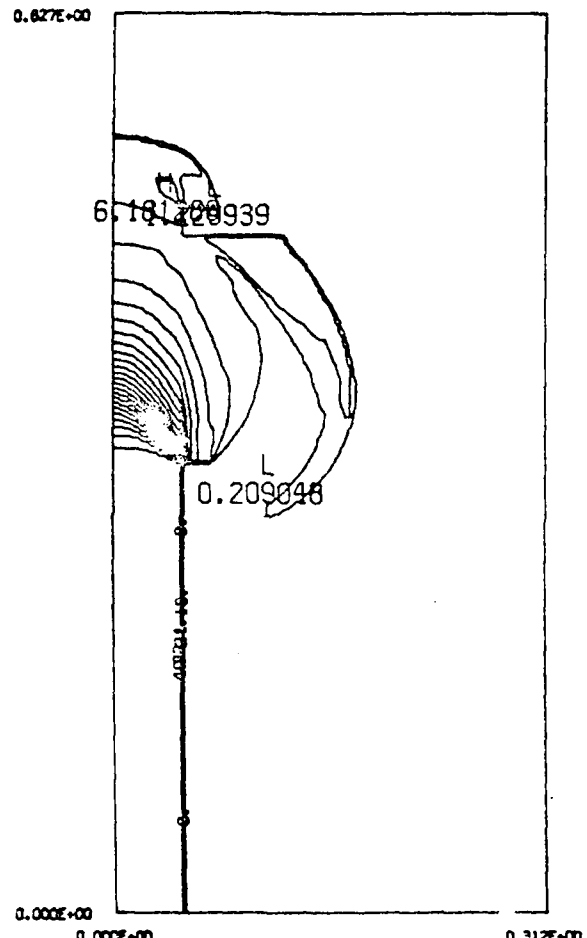
TIME= 0.10006E-03 SEC., STEP 253, DUMP HOWZ0003 PRESSURE, NEWTONS/M\*\*2



CENTEUR PRES 0.00000 T8 0.28100E-08 CENTEUR INTERVAL OF 0.10000E-07 PT(3,3)= 0.28100E-08 UNITLE3 SCALING BY 0.10000E-04

Figure 36a

105 MM HOWITZER MUZZLE FLOW  
TIME= 0.10006E-03 SEC., STEP 253, DUMP HOWZ0003 DENSITY 1, KG/M3



CONTOUR FROM 0.00000 THRU 48.000 CONTOUR INTERVAL OF 2.0000 PT(S, Z) = 48.722

Figure 36b

AD-A163 332

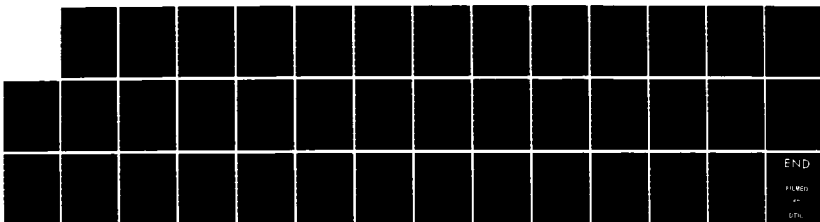
APPLICATION OF FLUX-CORRECTED TRANSPORT TO TTCP JOINT  
LAUNCH BLAST COMPUTATIONAL EFFORT(U) NAVAL RESEARCH LAB  
WASHINGTON DC P S KAMATH ET AL. 31 DEC 85 NRL-MR-5781

2/2

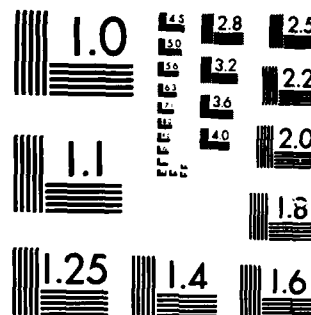
UNCLASSIFIED

F/G 19/4

NL

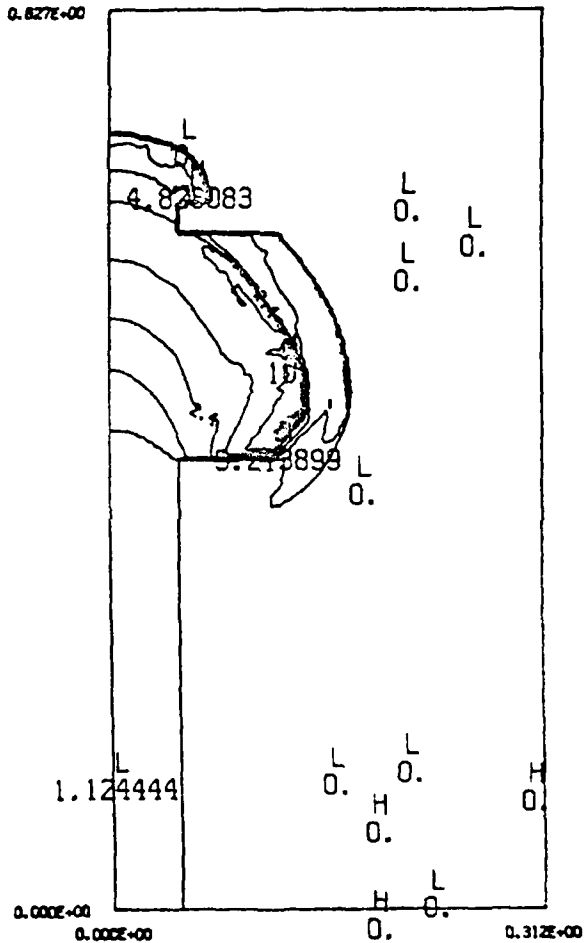


END  
FILED  
AT  
GPO



MICROCOPY RESOLUTION TEST CHART  
NATIONAL BUREAU OF STANDARDS 1963-A

105 MM HOWITZER MUZZLE FLOW  
TIME= 0.10006E-03 SEC., STEP 253. DUMP HOWZ0003 MACH NUMBER

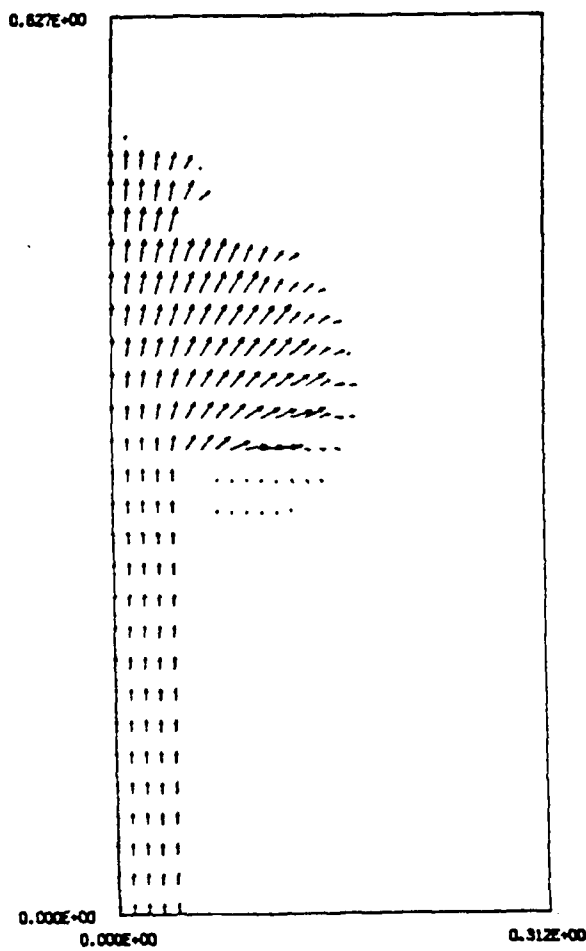


CONTOUR FROM 0.00000 TO 0.80000 CONTOUR INTERVAL OF 0.00000 PT(3,3)= 1.1244

Figure 36c

105 MM HOWITZER MUZZLE FLOW

TIME= 0.10006E-03 SEC., STEP 253, DUMP H0WZ0003 VELOCITY, M/SEC

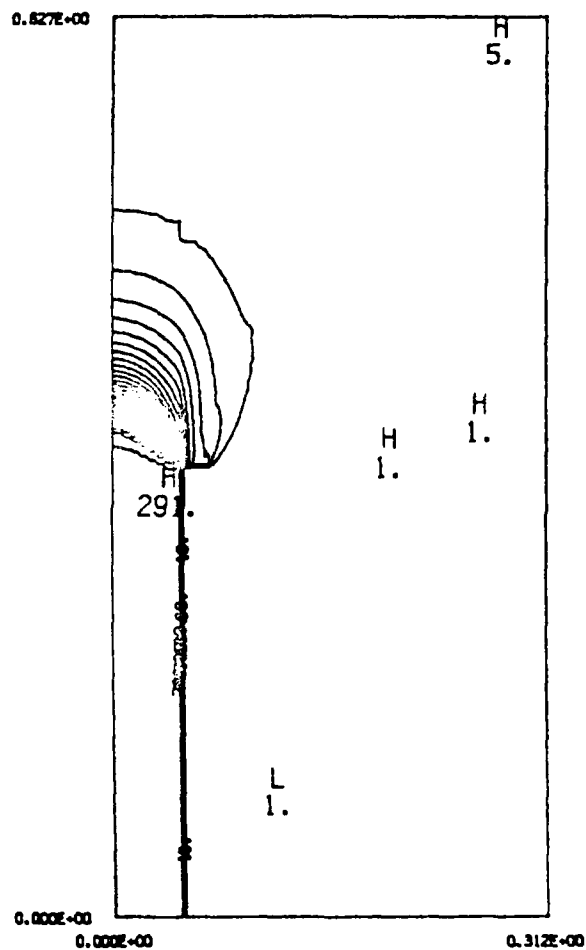


0.220E+01  
MAXIMUM VECTOR

Figure 36d

## 105 MM HOWITZER MUZZLE FLOW

TIME= 0.50000E-03 SEC.. STEP 1433. DUMP HOWZ0005 PRESSURE, NEWTONS/M<sup>2</sup>



CENTLAR PARM Q.00000 T8 Q.28000E-08 CENTLAR INTERVAL OF Q.10000E-07 PT(8.3) Q.38000E-08 LABELS SCALD BY Q.10000E-04

Figure 37a

105 MM HOWITZER MUZZLE FLOW

TIME= 0.50000E-03 SEC., STEP 1433, DUMP HOWZ0005 DENSITY 1. KG/M3

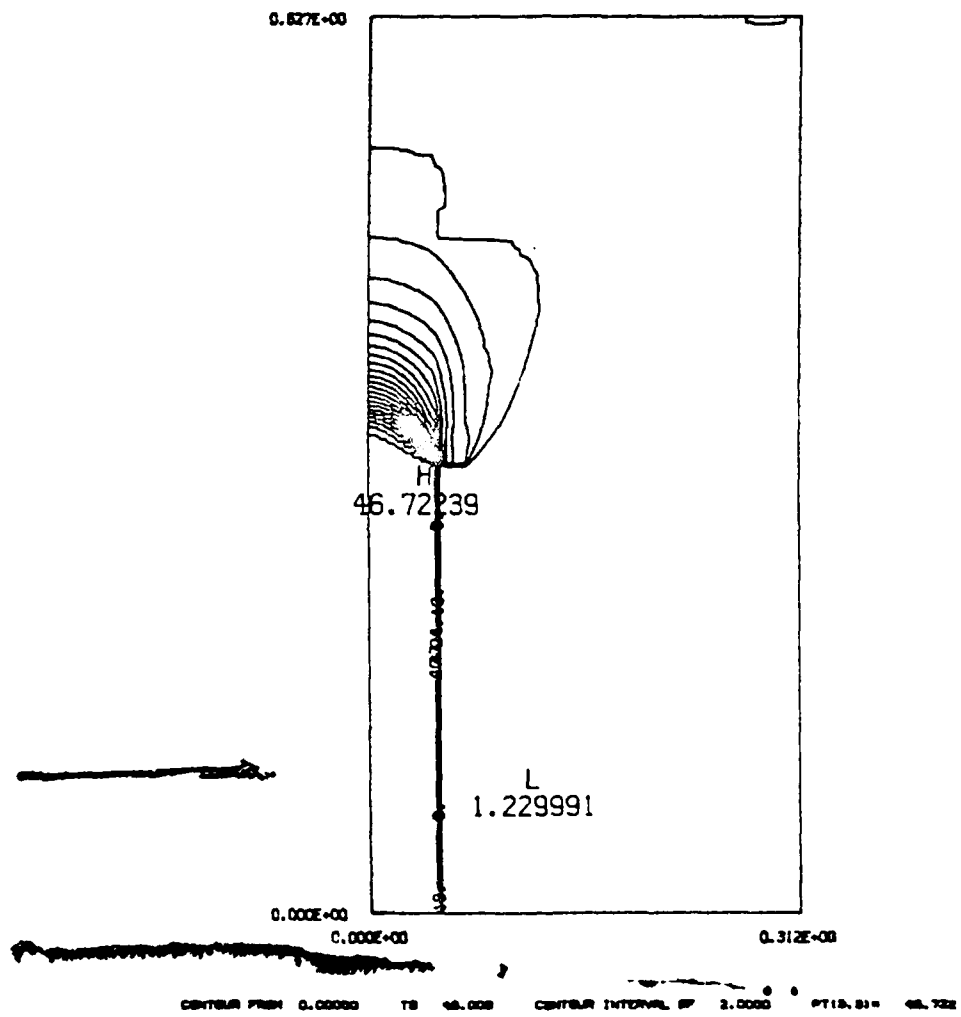


Figure 37b

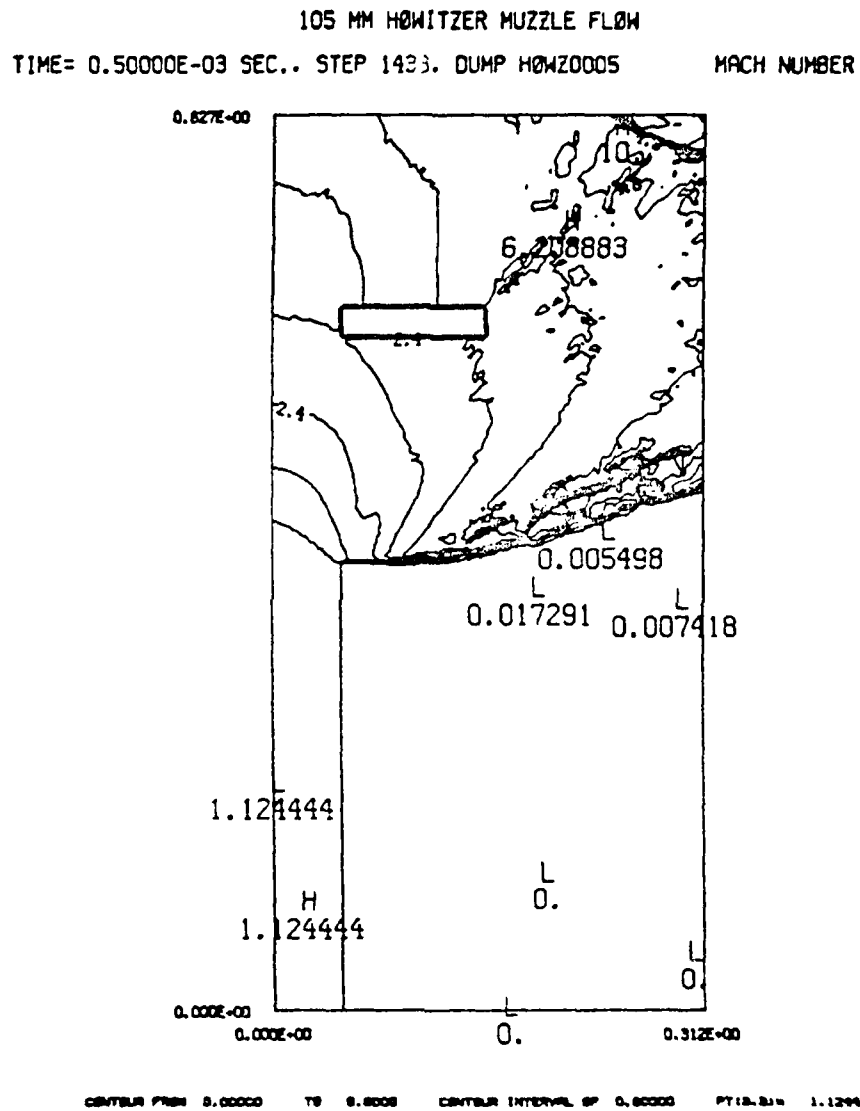
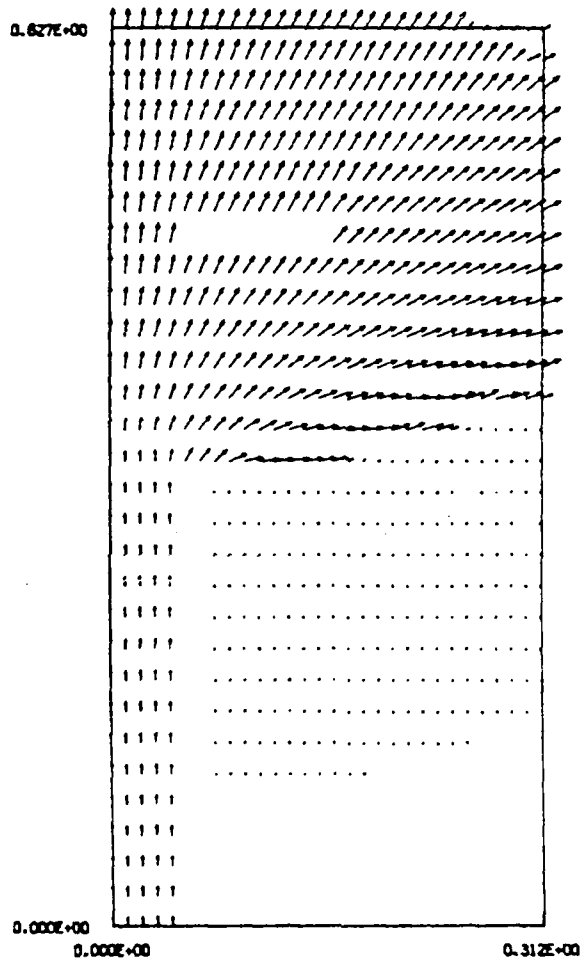


Figure 37c

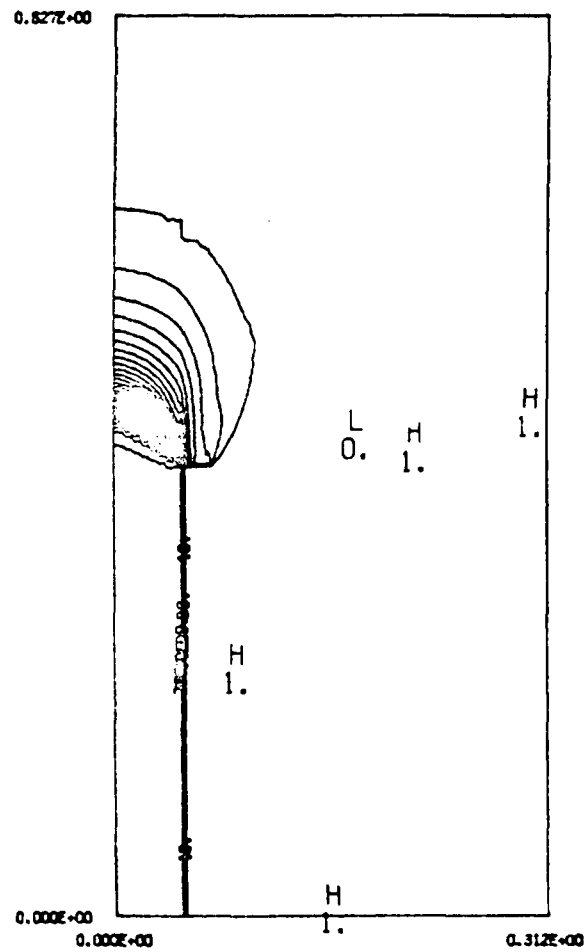
105 MM HOWITZER MUZZLE FLOW  
TIME= 0.5000E-03 SEC., STEP 1433, DUMP HOWZ0005      VELOCITY, M/SEC



0.262E+01  
MAGNITUDE VECTOR

Figure 37d

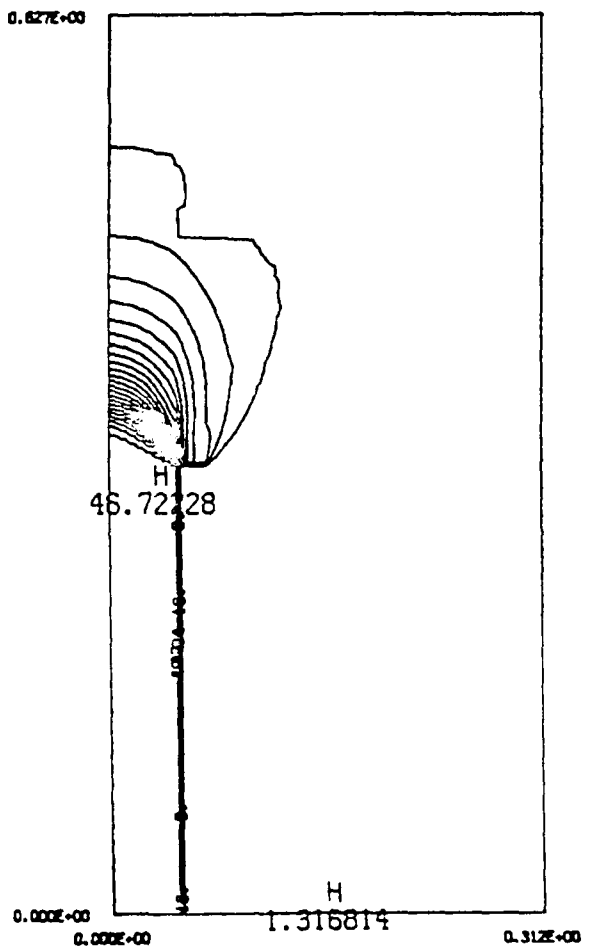
105 MM HOWITZER MUZZLE FLOW  
TIME= 0.10000E-02 SEC., STEP 2735, DUMP HOWZ0007 PRESSURE, NEWTONS/M\*\*2



CENTEUR PRES 0.0000 T0 0.28000E-03 CENTEUR INTERVAL OF 0.10000E-07 PT(S,S)= 0.28100E-03 LABELS SCALED BY 0.10000E-04

Figure 38a

105 MM HOWITZER MUZZLE FLOW  
TIME= 0.10000E-02 SEC.. STEP 2735. DUMP HOWZ0007 DENSITY 1. KG/M3



CENTRAL POINT 0.0000 T0 46.000 CENTRAL INTERVAL OF 2.0000 PT13.814 46.722

Figure 38b

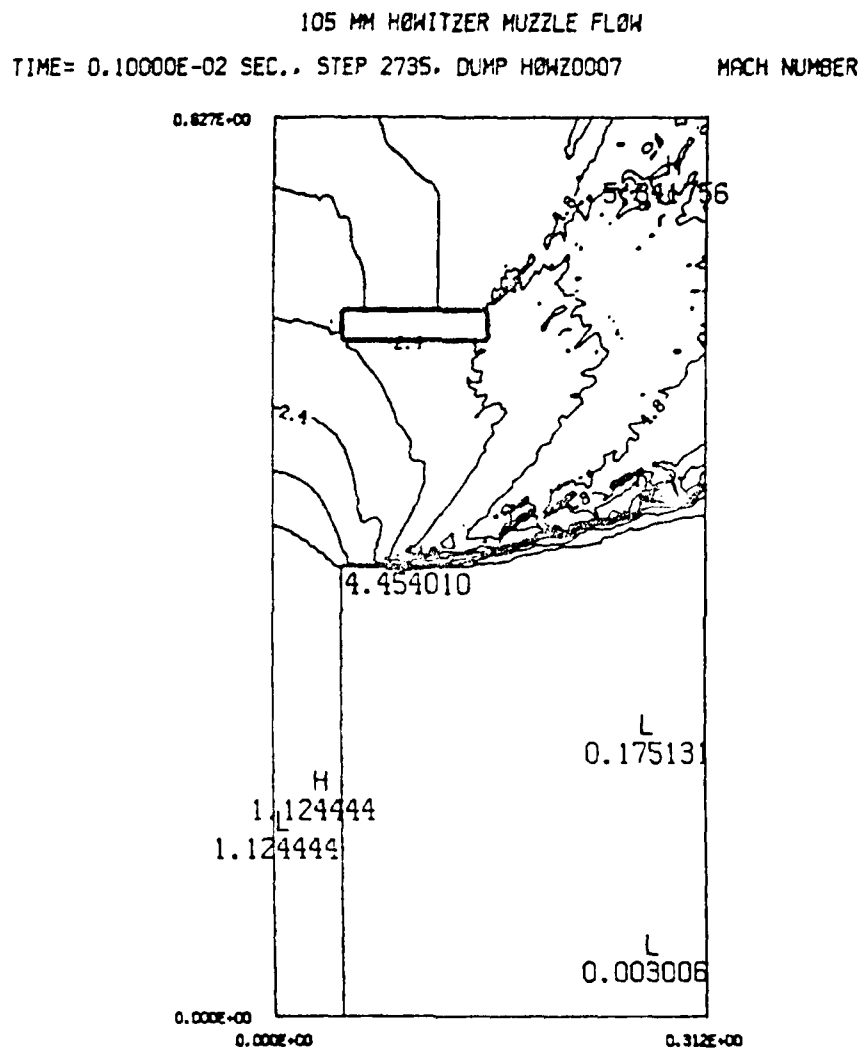


Figure 38c

105 MM HOWITZER MUZZLE FLOW  
TIME= 0.75002E-03 SEC., STEP 2073, DUMP HOWZ0006      VELOCITY, M/SEC

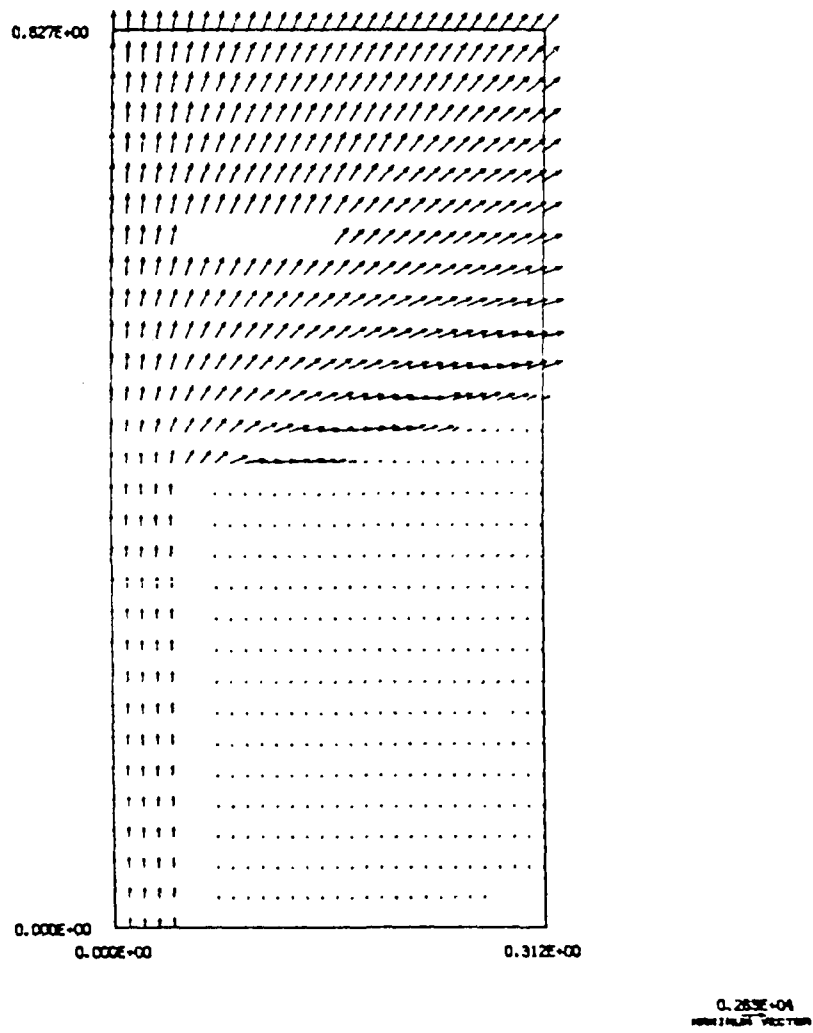
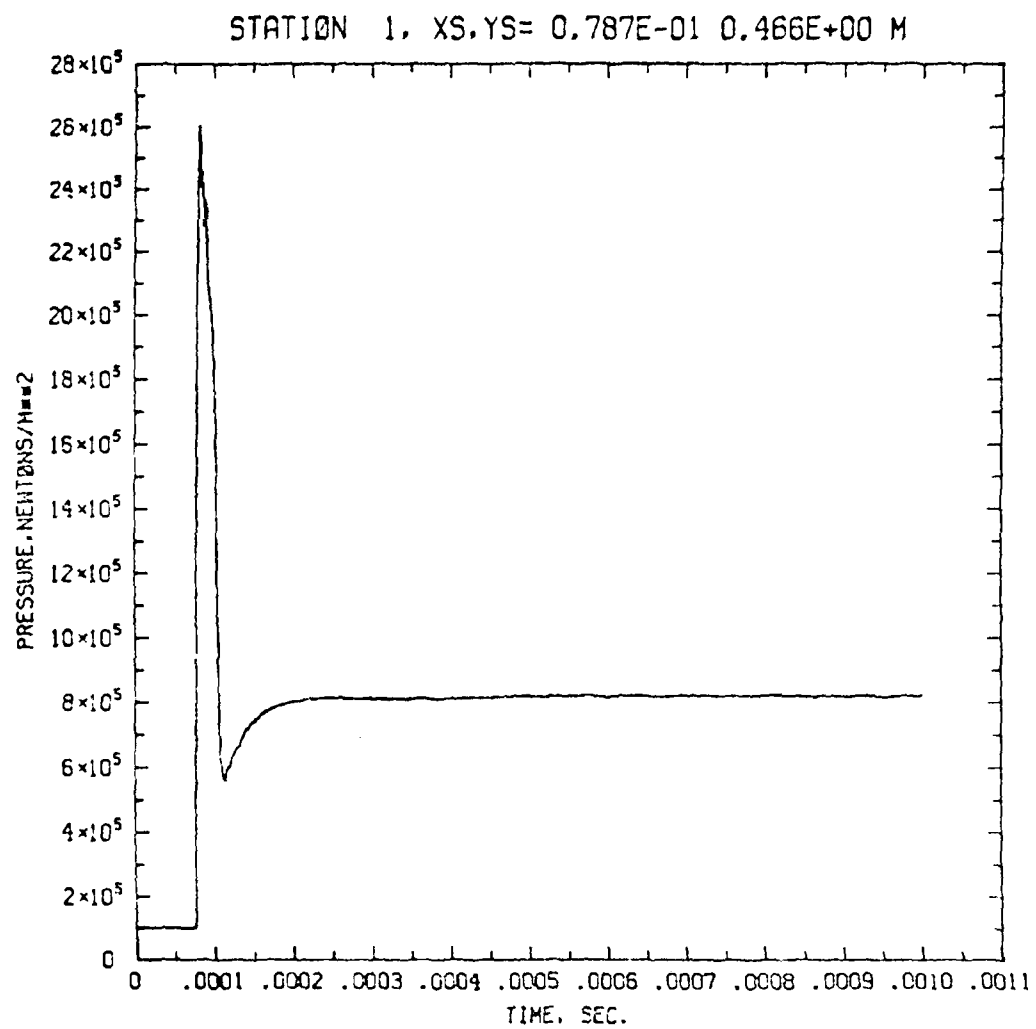


Figure 38d

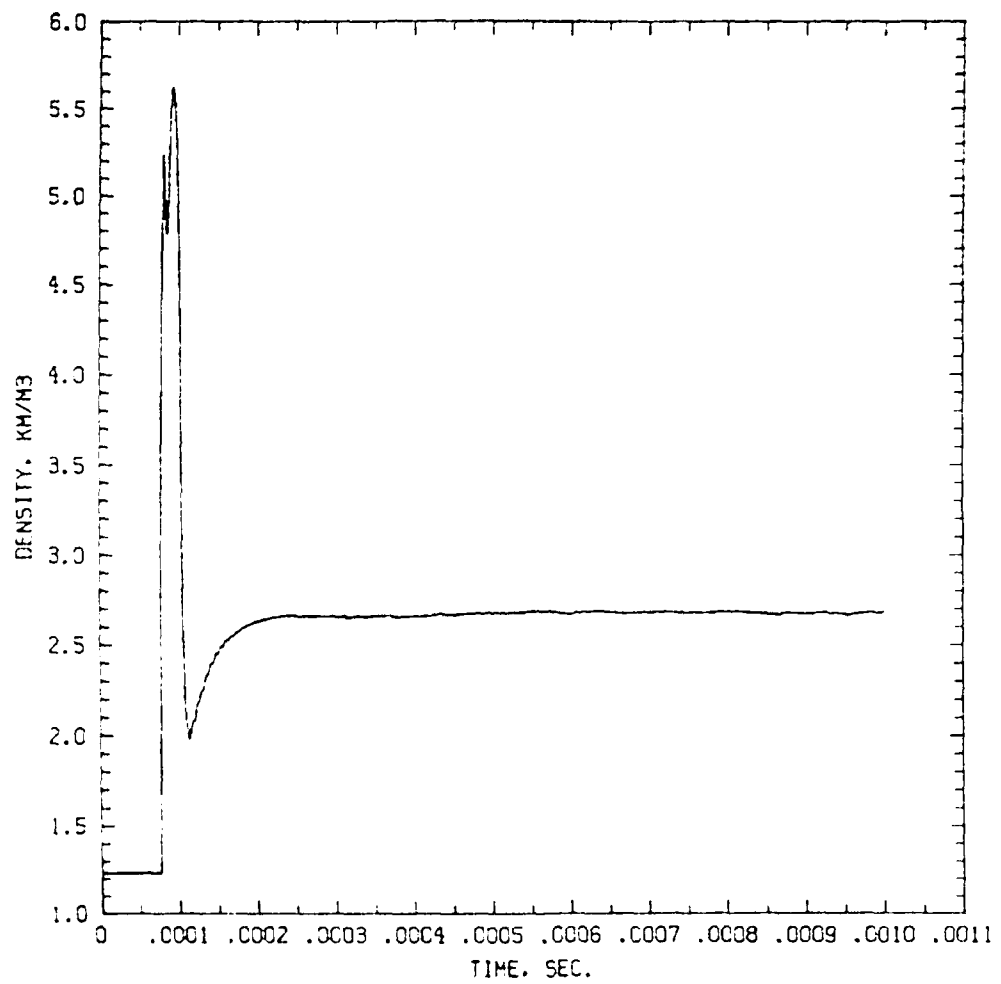


105 MM HOWITZER MUZZLE FLOW

8 DUMPS. LAST DUMP IS NON-ZERO

Figure 39a

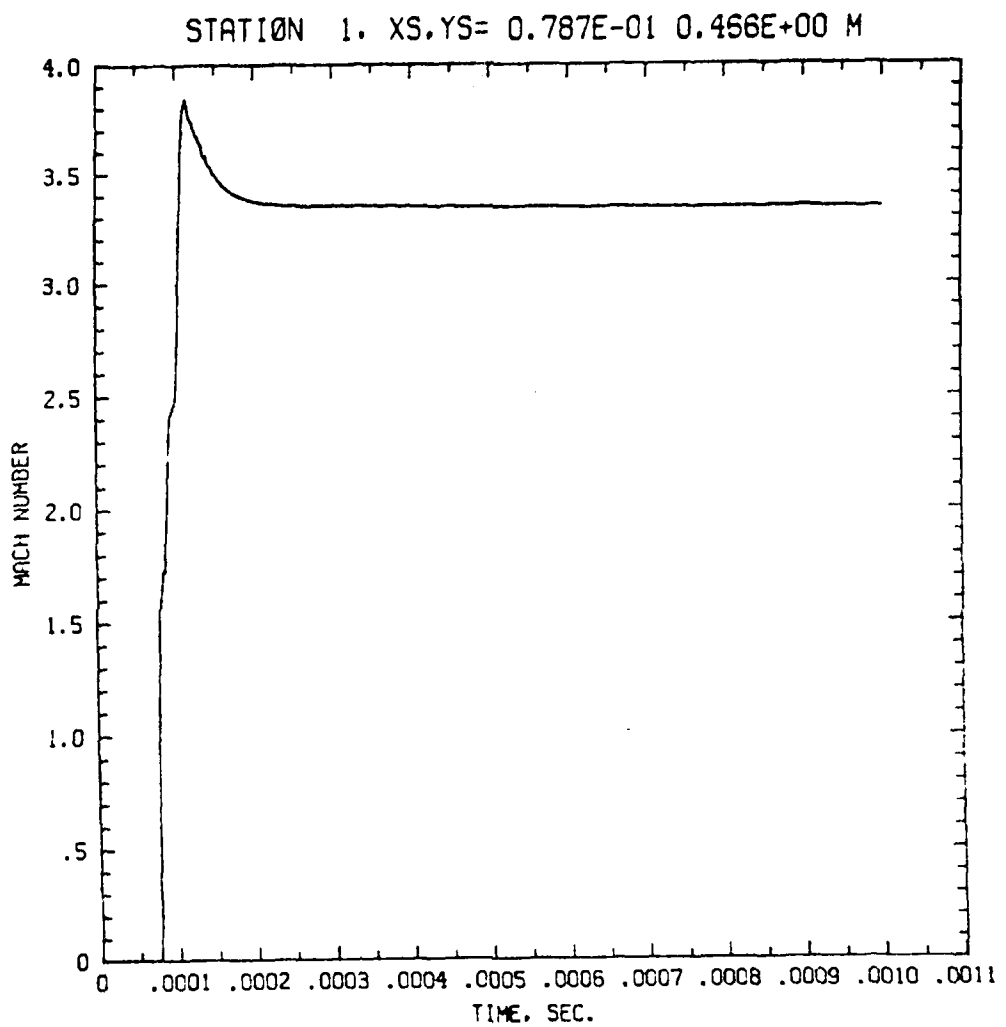
STATION 1, XS.YS= 0.787E-01 0.466E+00 M



105 MM HOWITZER MUZZLE FLOW

8 DUMPS. LAST DUMP IS HEMZ0000

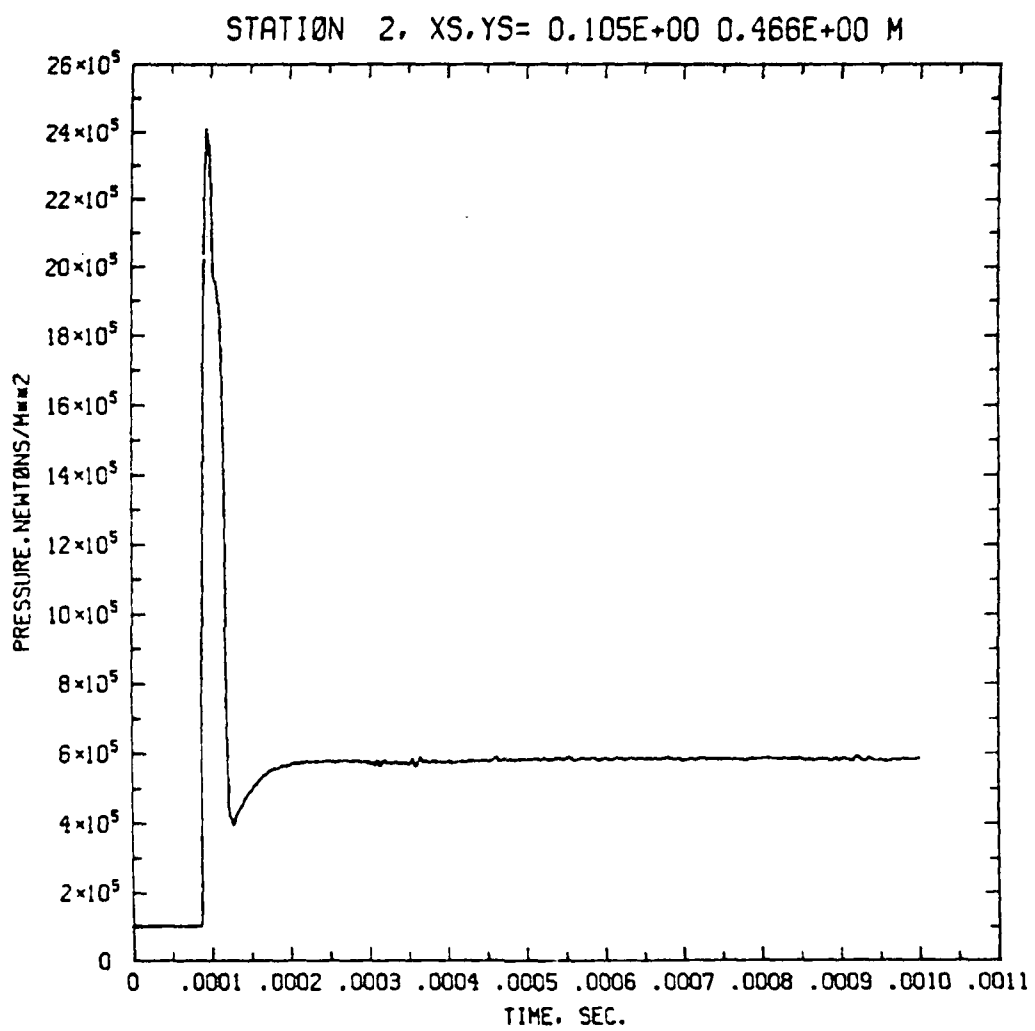
Figure 39b



105 MM HOWITZER MUZZLE FLOW

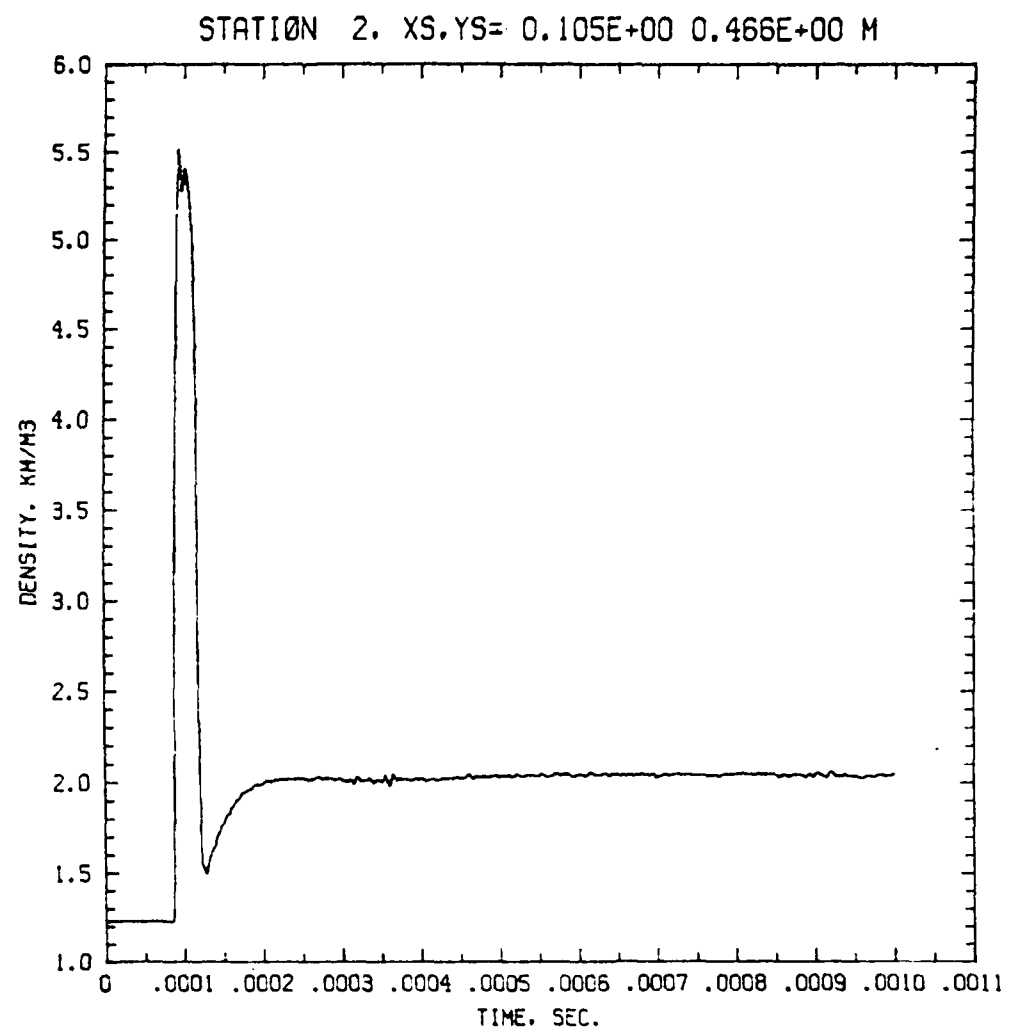
8 DUMPS. LAST DUMP IS 105E0009

Figure 39c



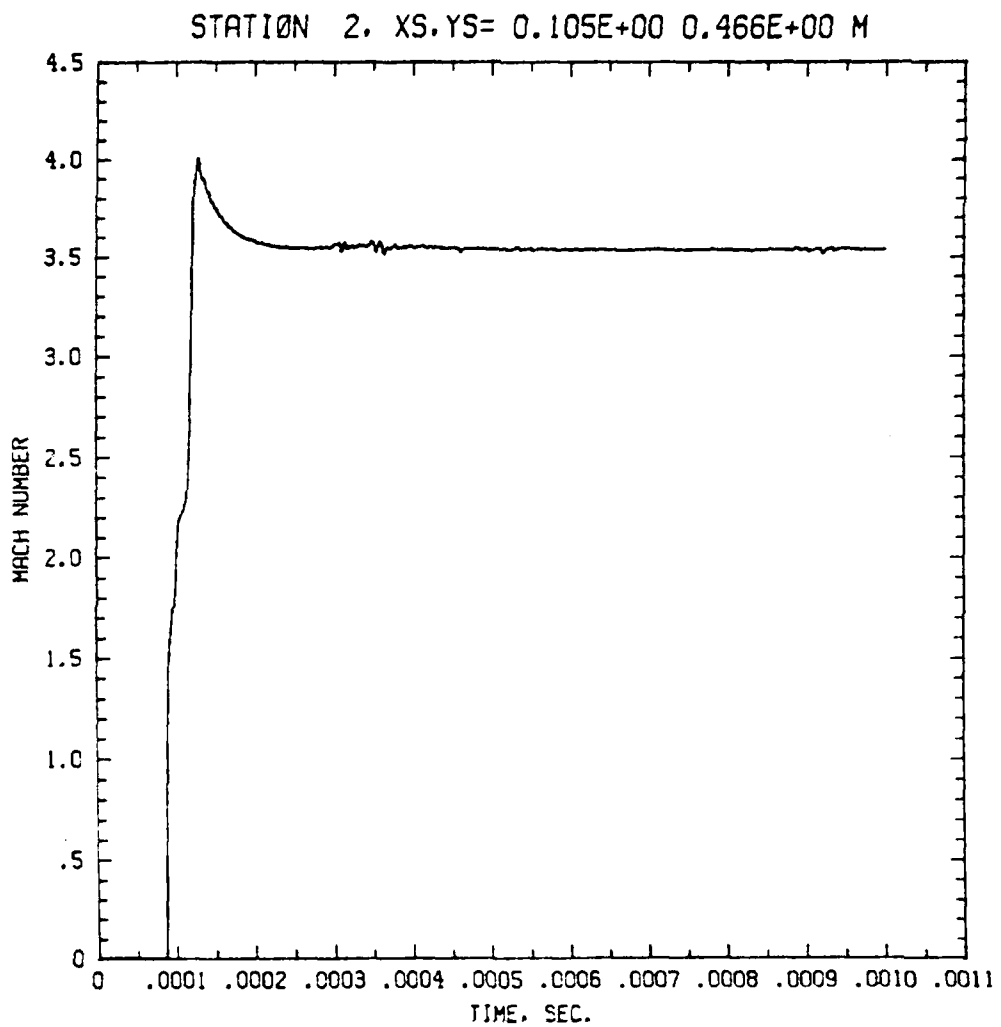
105 MM HOWITZER MUZZLE FLOW  
8 DUMPS. LAST DUMP IS NOW 20009

Figure 40a



105 MM HOWITZER MUZZLE FLOW  
8 DUMPS. LAST DUMP IS NOW 0008

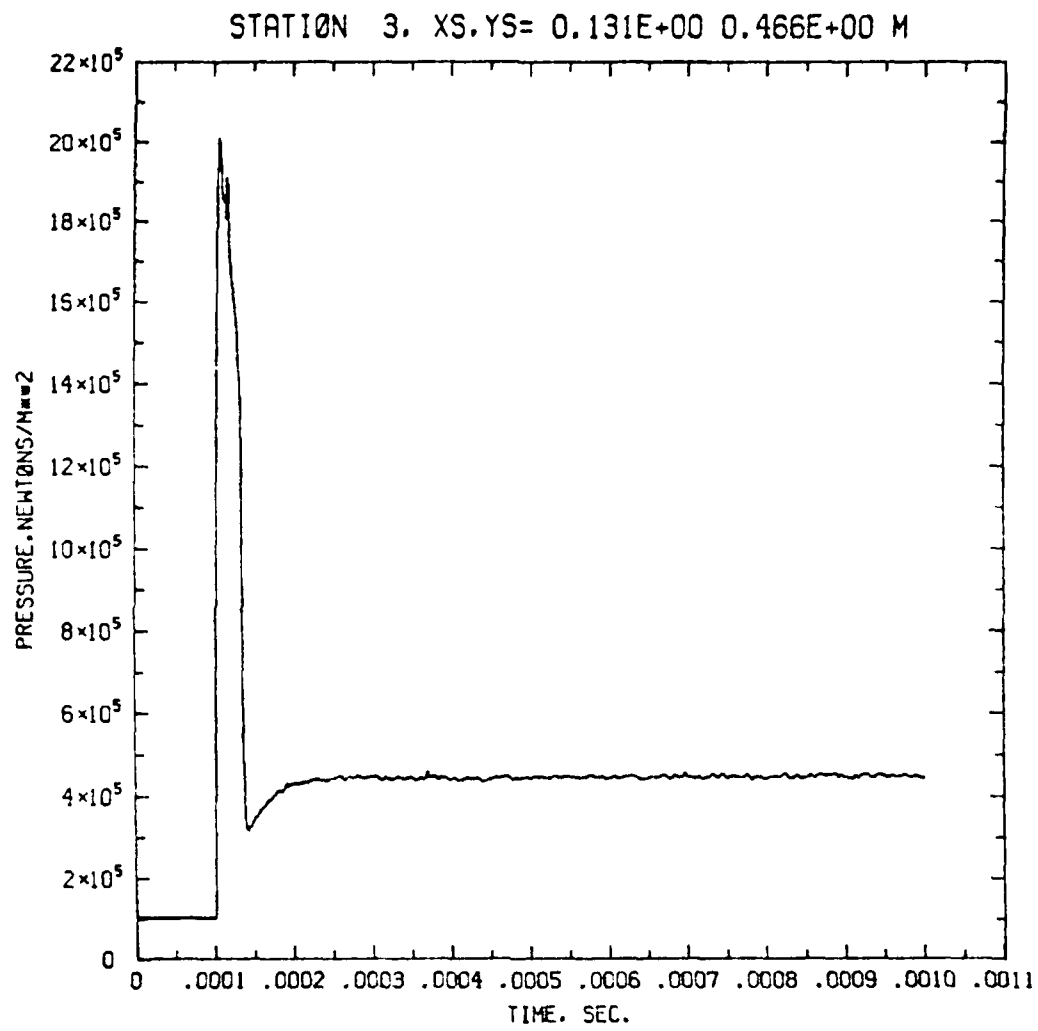
Figure 40b



105 MM HOWITZER MUZZLE FLOW

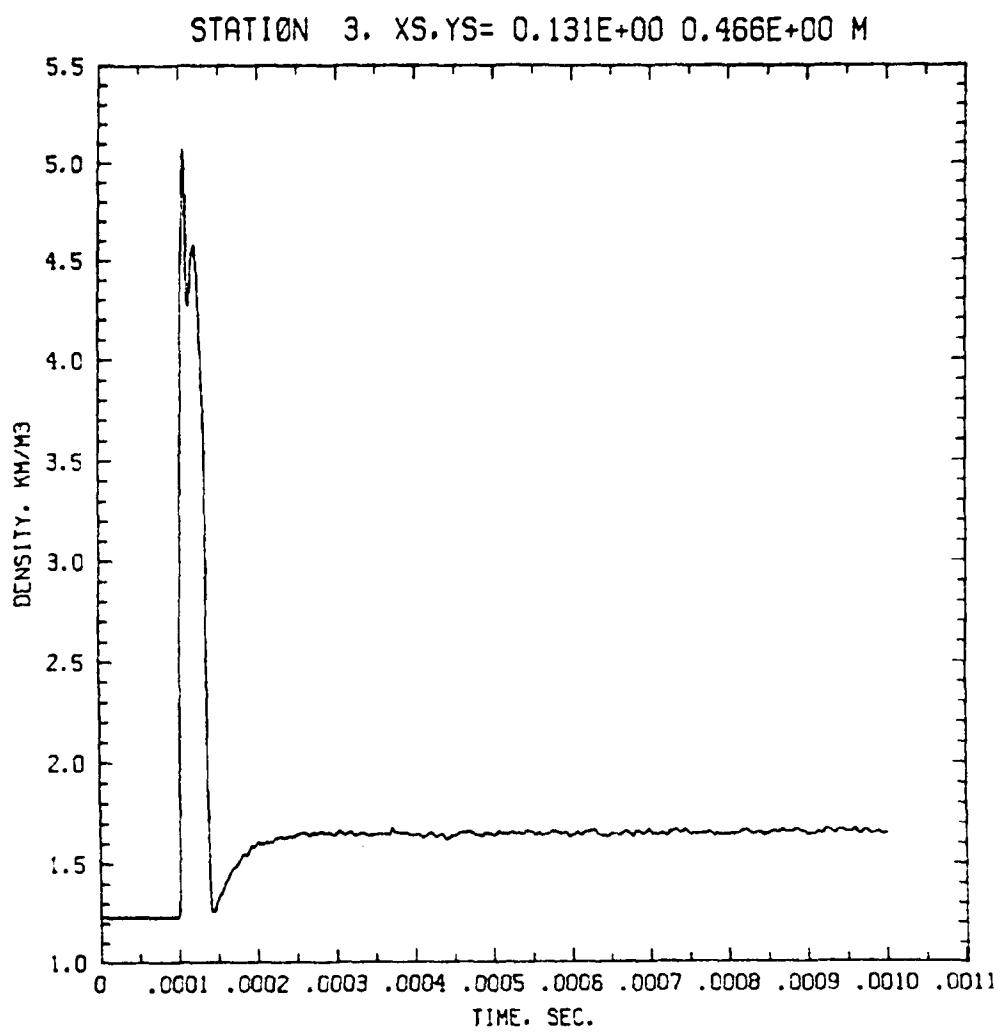
• DUMPS. LAST DUMP IS HSW20000

Figure 40c



105 MM HOWITZER MUZZLE FLOW  
9 DUMPS. LAST DUMP IS 1000000000

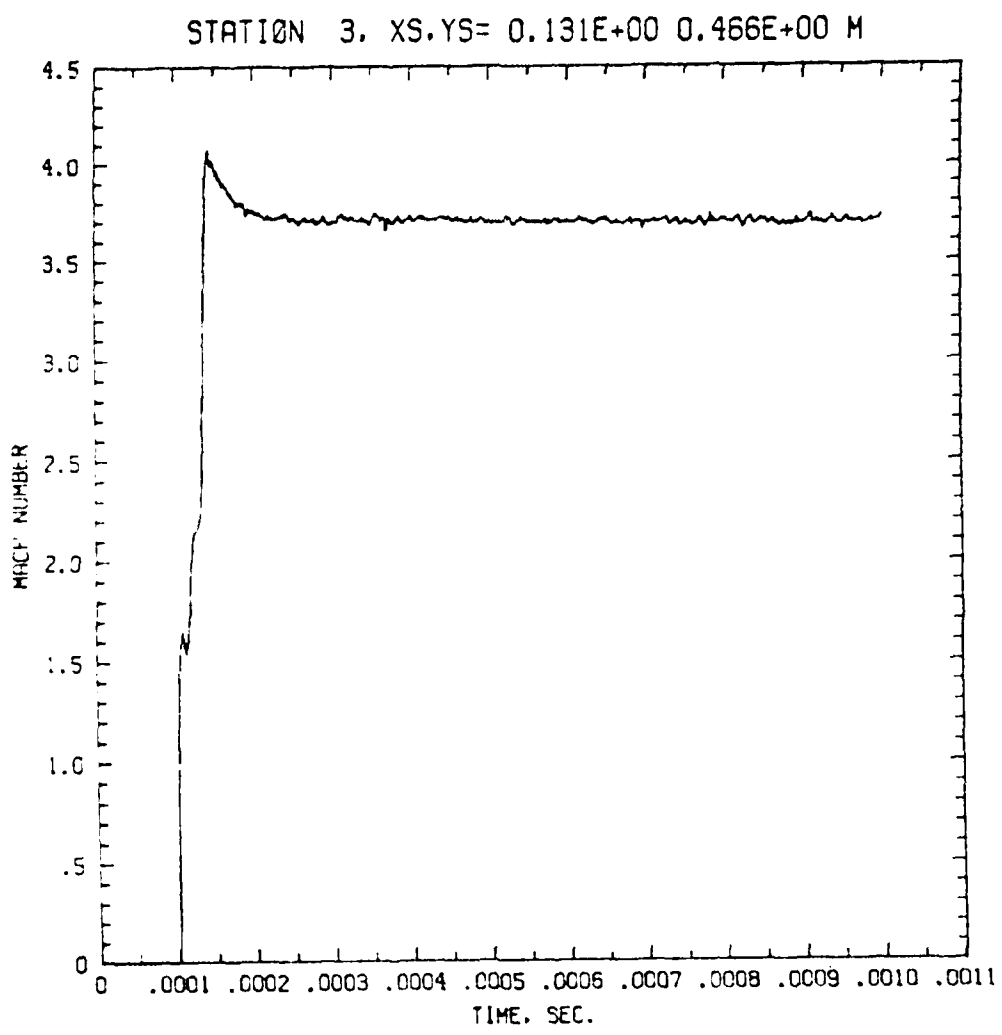
Figure 41a



105 MM HOWITZER MUZZLE FLOW

9 DUMPS. LAST DUMP IS 100K20009

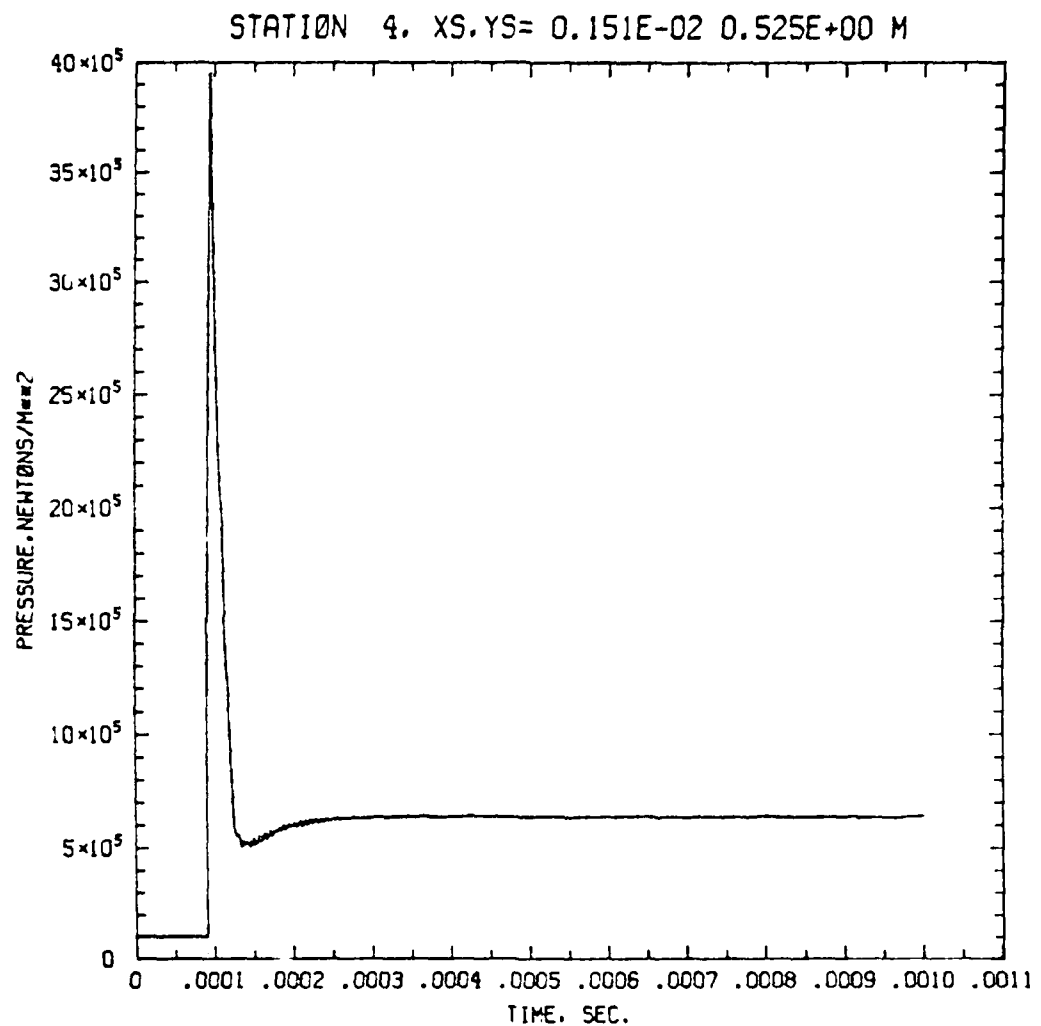
Figure 41b



105 MM HOWITZER MUZZLE FLOW

\* DUMPS. LAST DUMP IS 40HZ0009

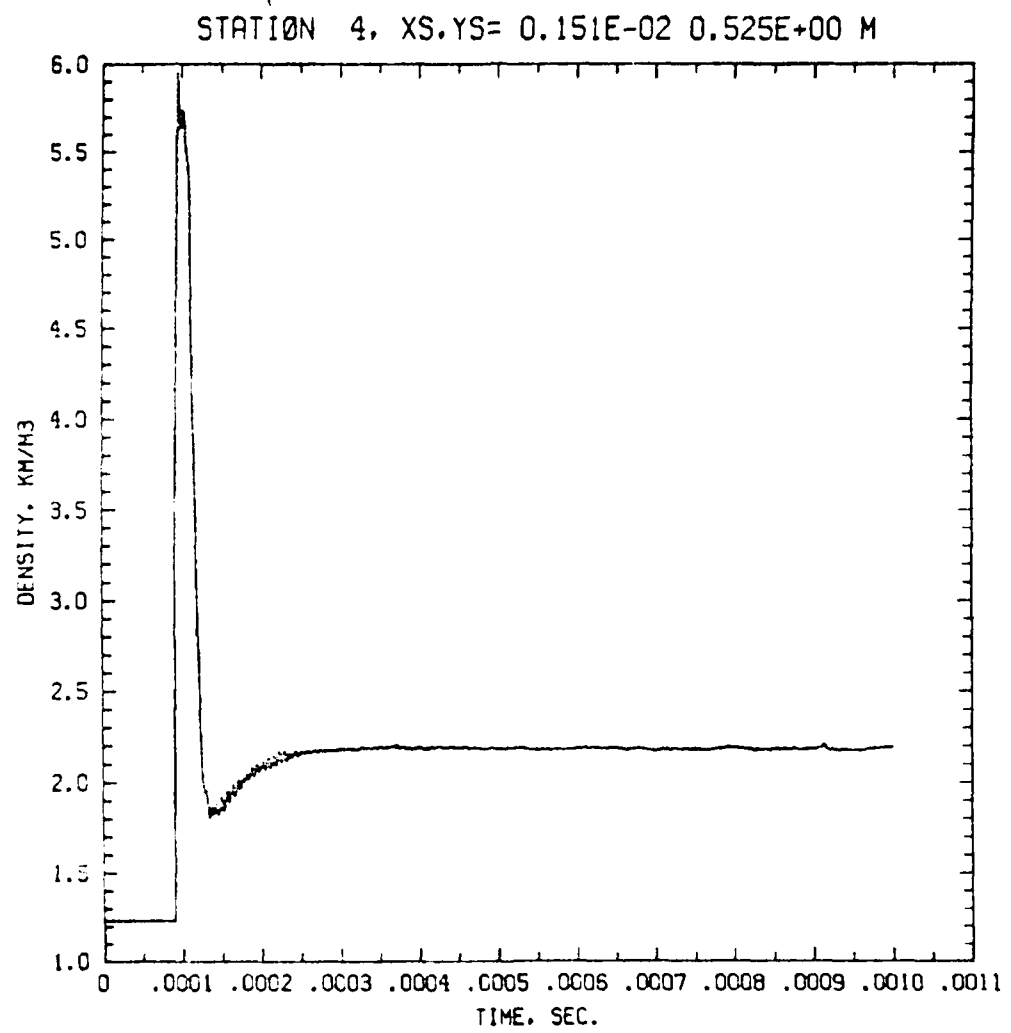
Figure 41c



105 MM HOWITZER MUZZLE FLOW

8 DUMPS. LAST DUMP IS 13 MSEC

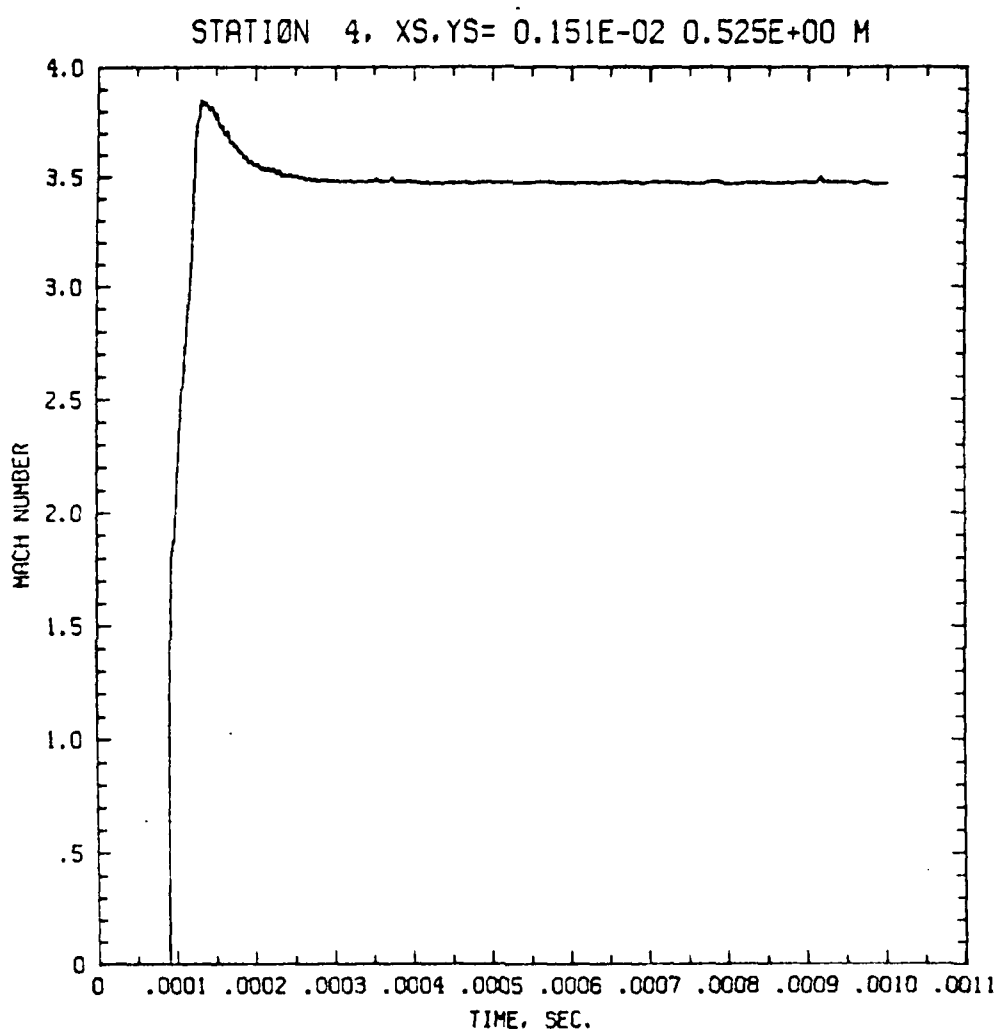
Figure 42a



## 105 MM HOWITZER MUZZLE FLOW

8 DUMPS. LAST DUMP IS H2H2CC009

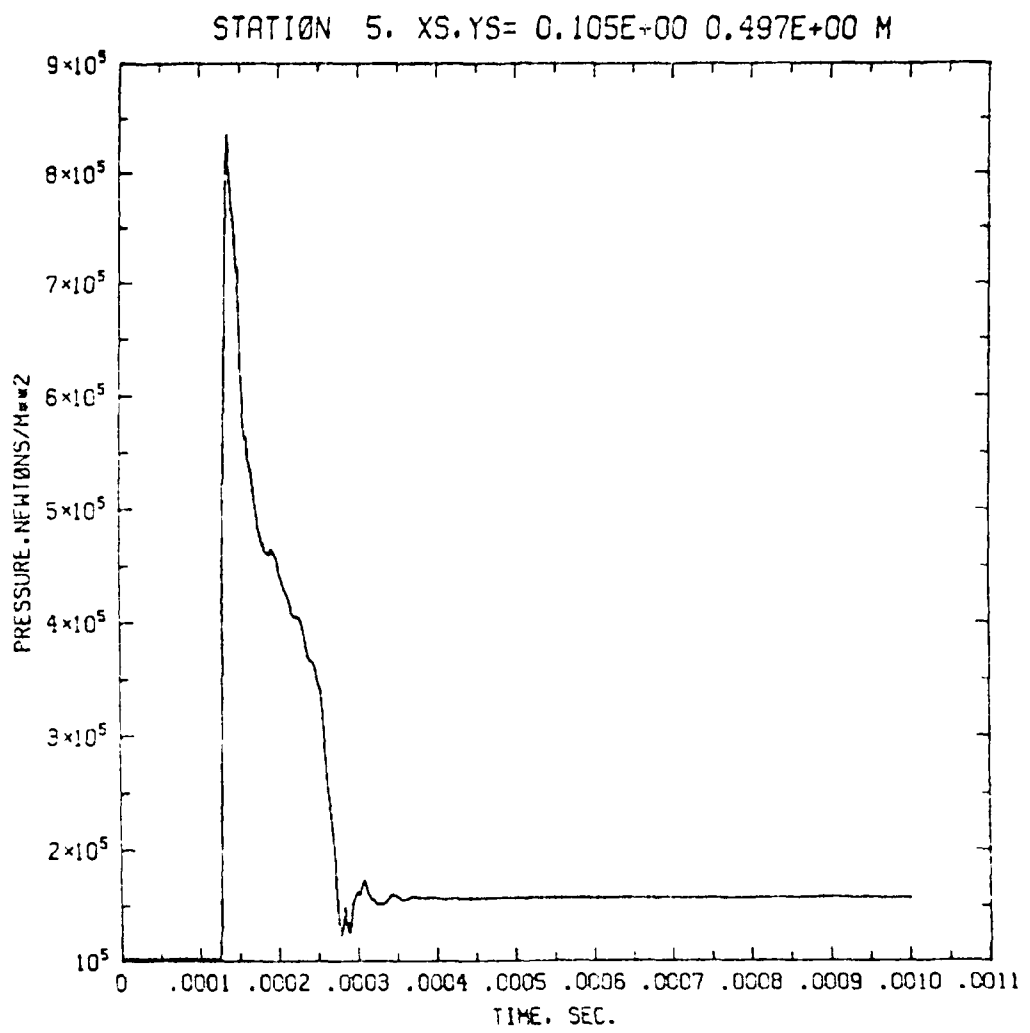
Figure 42b



105 MM HOWITZER MUZZLE FLOW

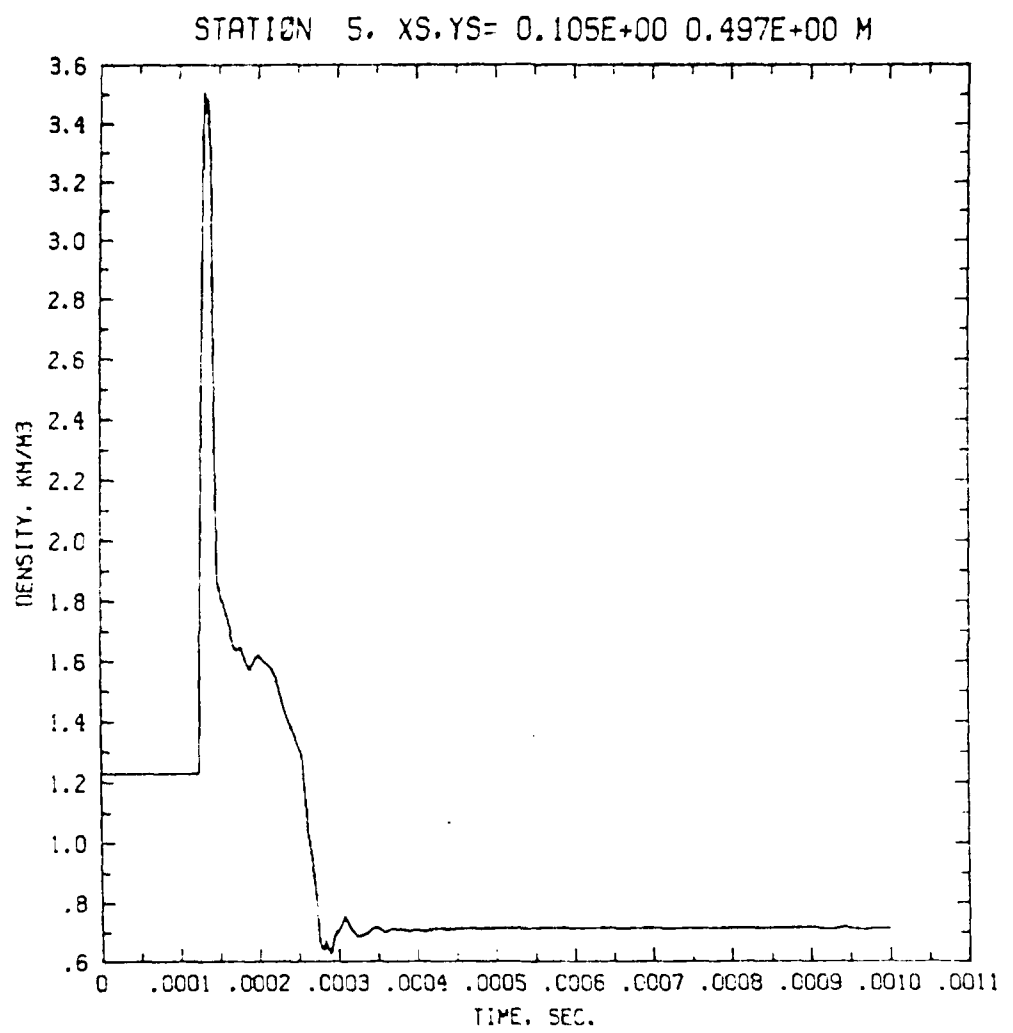
8 DUMPS. LAST DUMP IS H04Z0009

Figure 42c



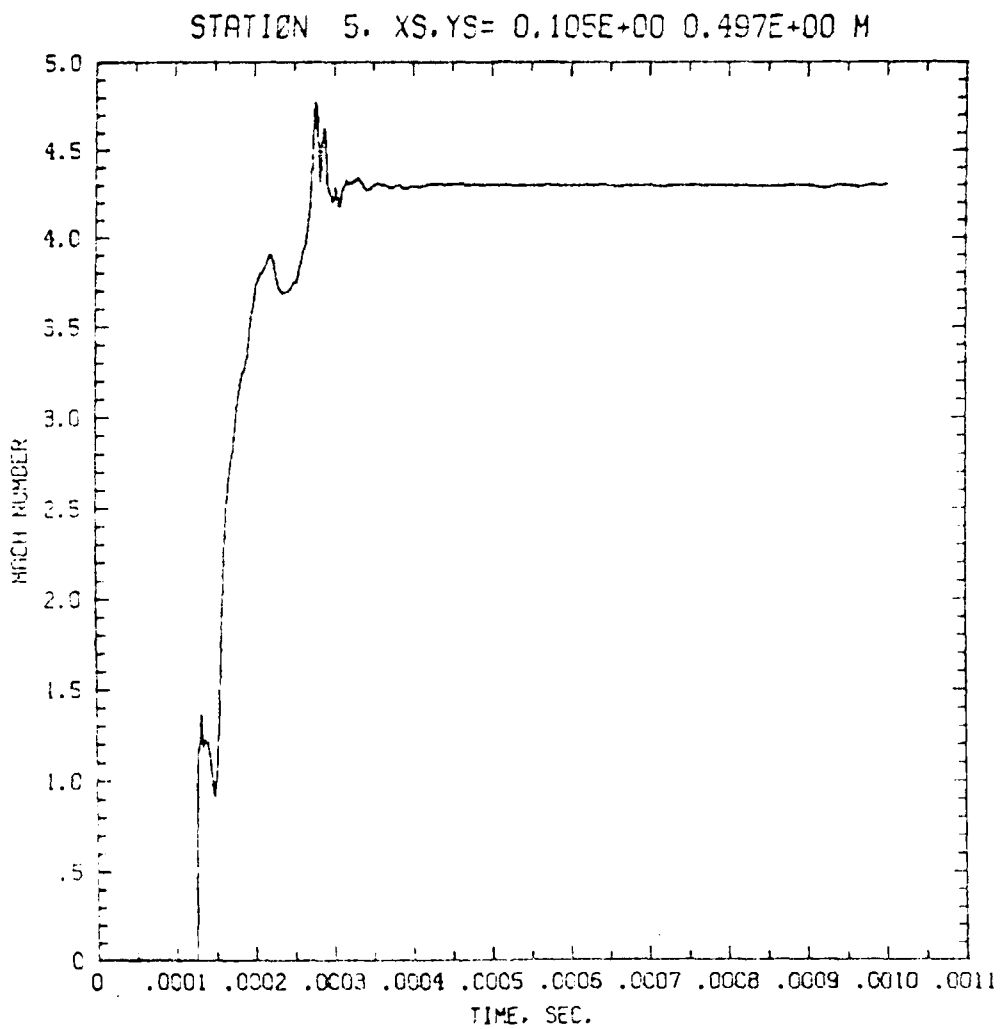
105 MM HOWITZER MUZZLE FLOW  
@ DUMPS. LAST DUMP IS HARMONIC

Figure 43a



105 MM HOWITZER MUZZLE FLOW  
8 DUMPS. LAST DUMP IS 100420009

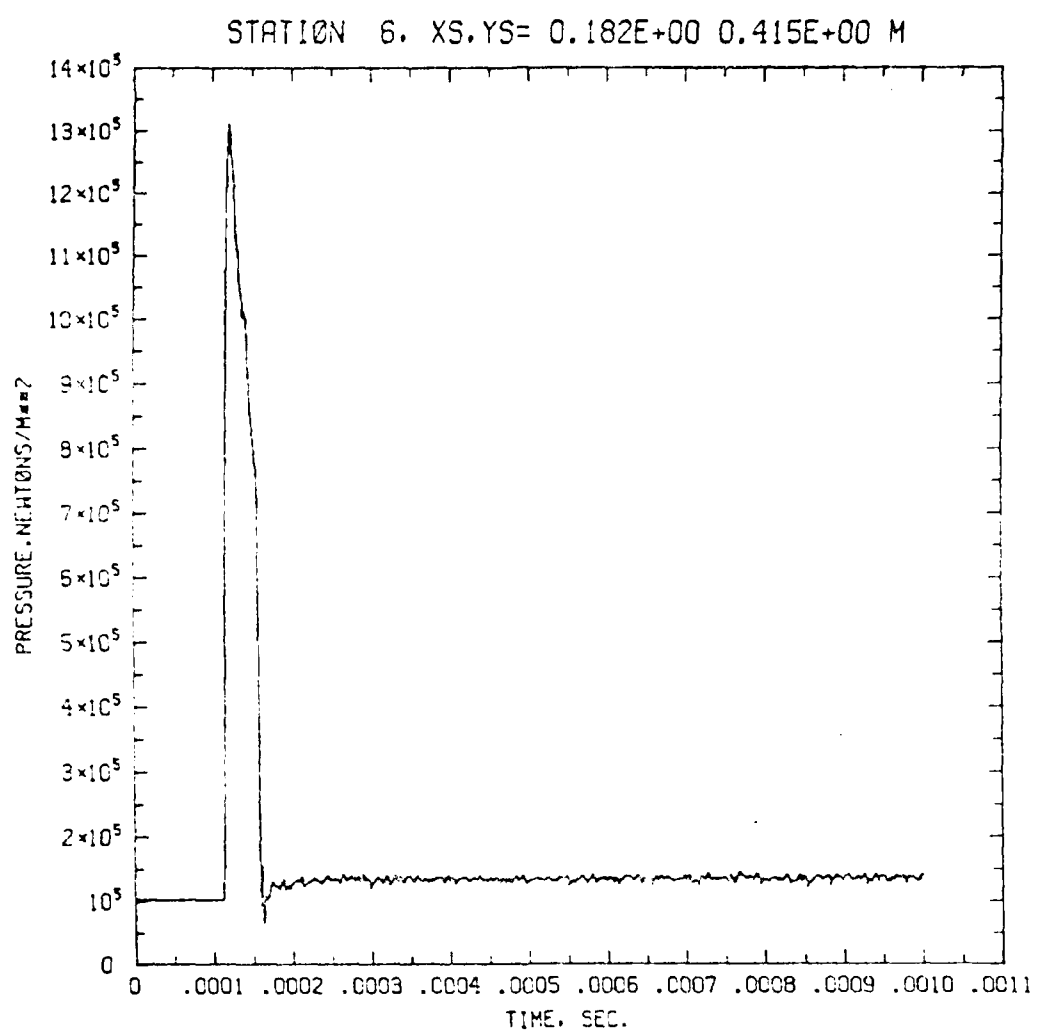
Figure 43b



105 MM HOWITZER MUZZLE FLOW

8 DUMPS. LAST DUMP IS 0.0020000

Figure 43c

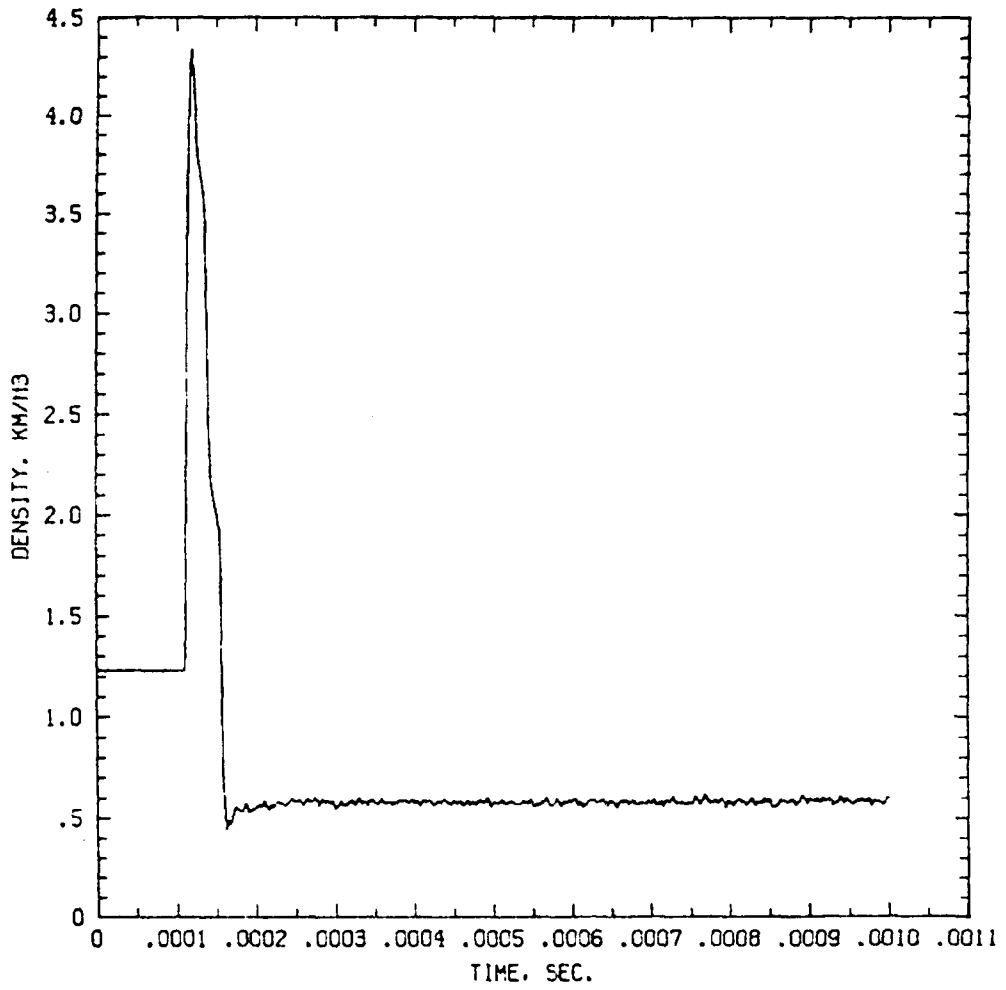


105 MM HOWITZER MUZZLE FLOW

0 DUMPS. LAST DUMP IS 100HZ0009

Figure 4-4a

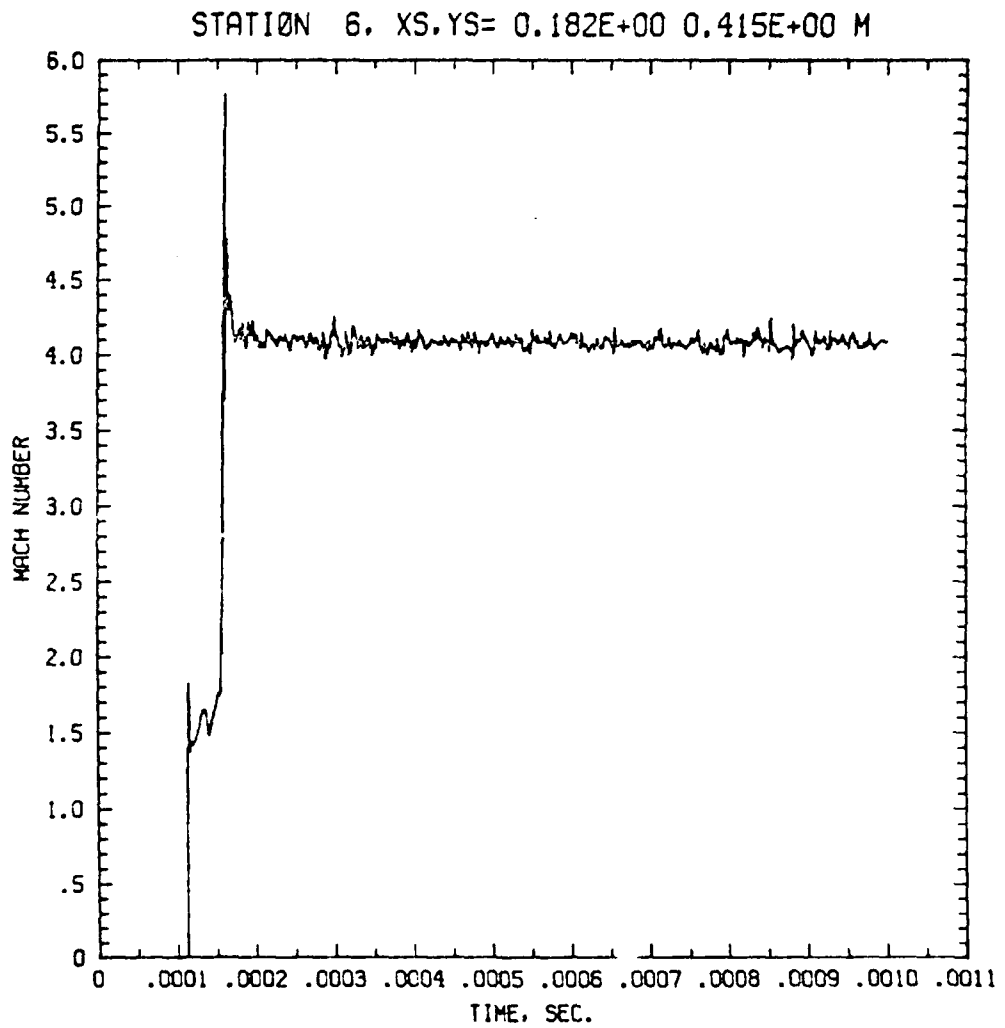
STATION 6. XS,YS= 0.182E+00 0.415E+00 M



105 MM HOWITZER MUZZLE FLOW

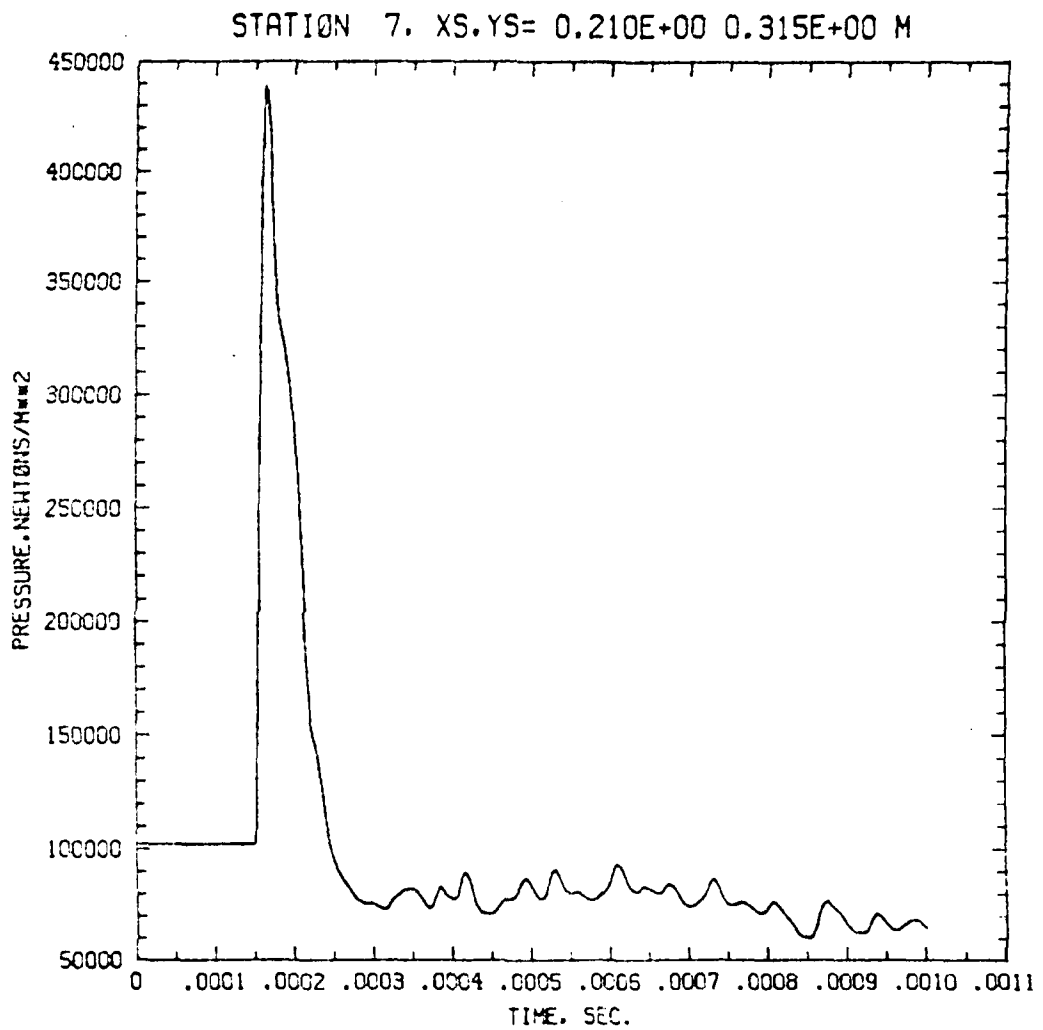
9 DUMPS. LAST DUMP IS HS4Z0009

Figure 44b



105 MM HOWITZER MUZZLE FLOW  
8 DUMPS. LAST DUMP IS 19 MB-20000

Figure 44c

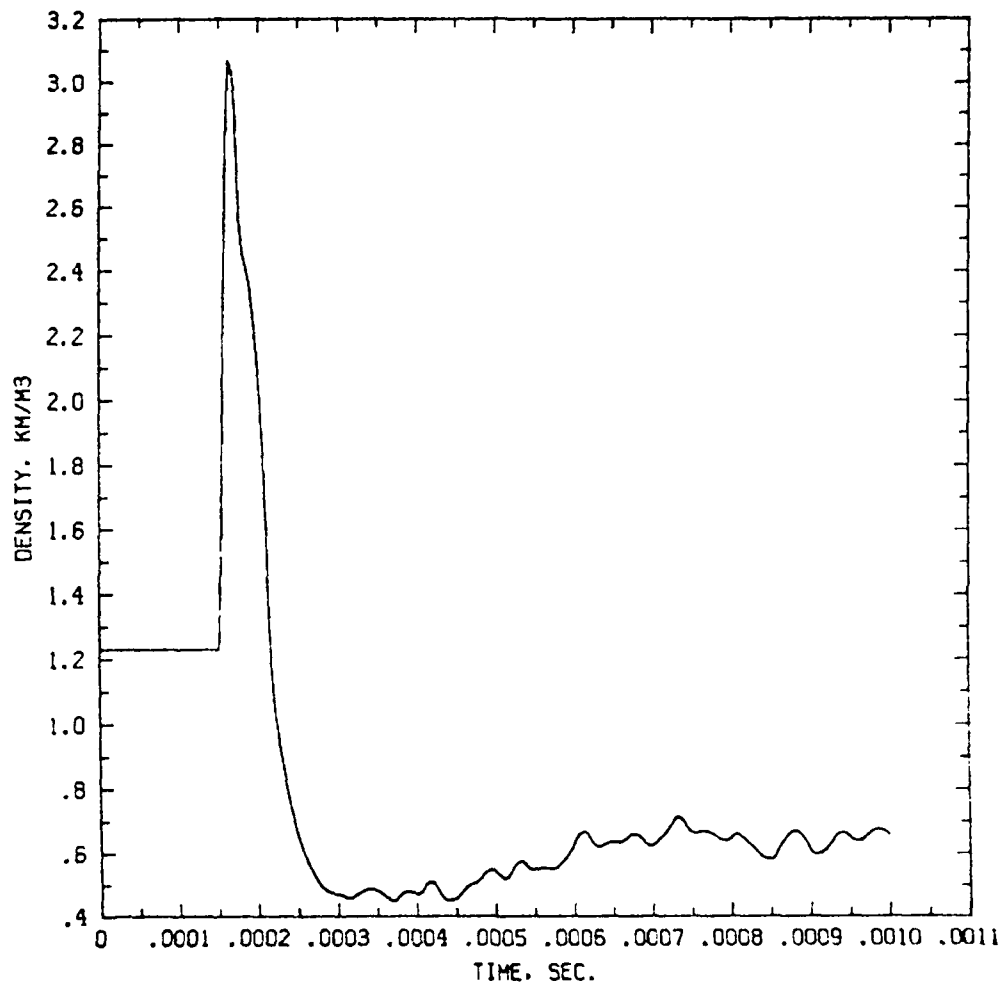


105 MM HOWITZER MUZZLE FLOW

9 DUMPS. LAST DUMP IS NOW 2009

Figure 45a

STATION 7, XS.YS= 0.210E+00 0.315E+00 M

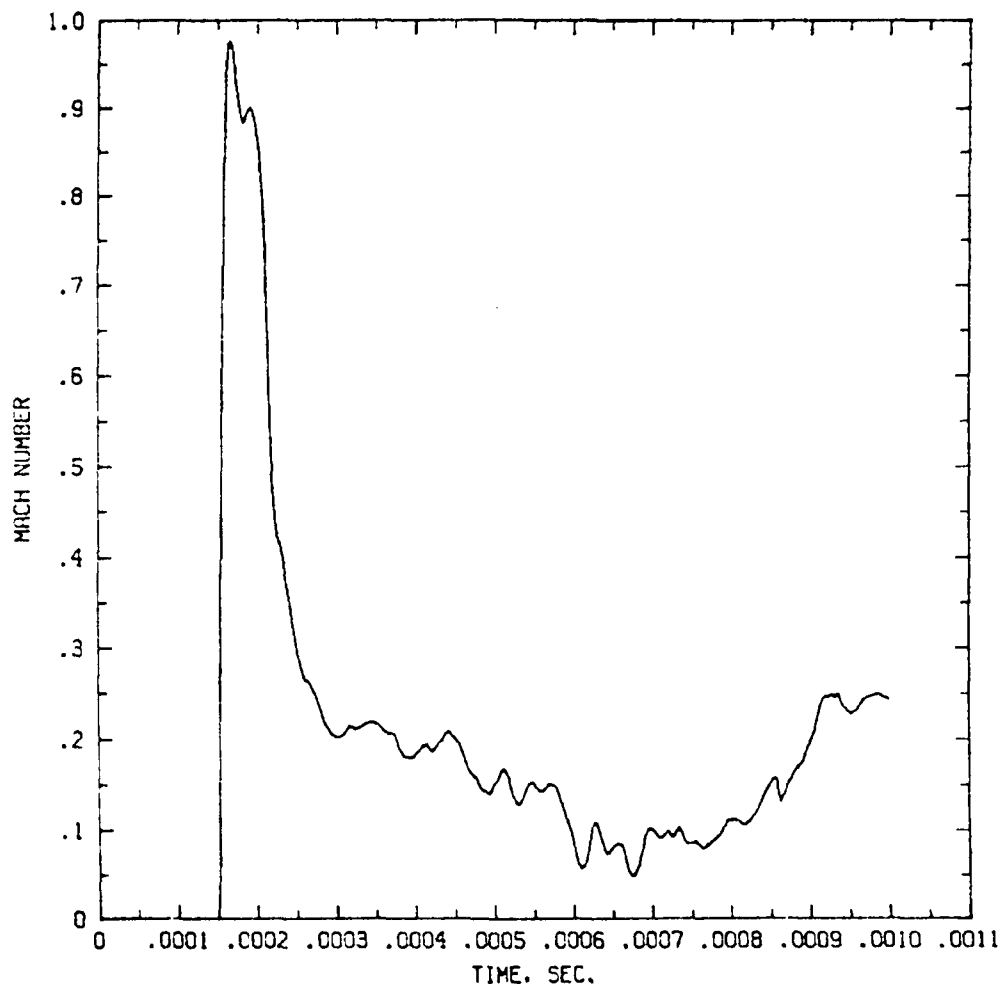


105 MM HOWITZER MUZZLE FLOW

8 DUMPS. LAST DUMP IS NOWZD008

Figure 45b

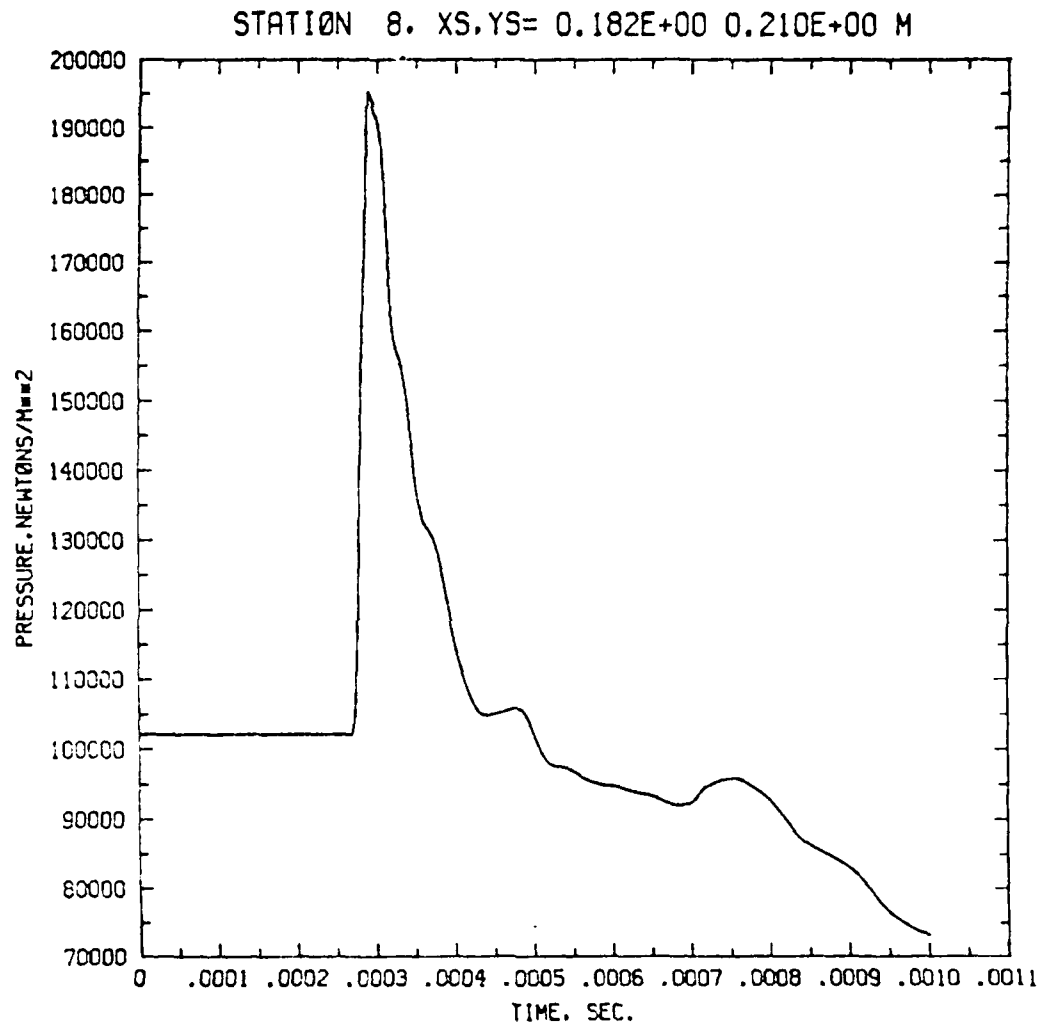
STATION 7. XS.YS= 0.210E+00 0.315E+00 M



105 MM HOWITZER MUZZLE FLOW

9 DUMPS. LAST DUMP IS 10420000

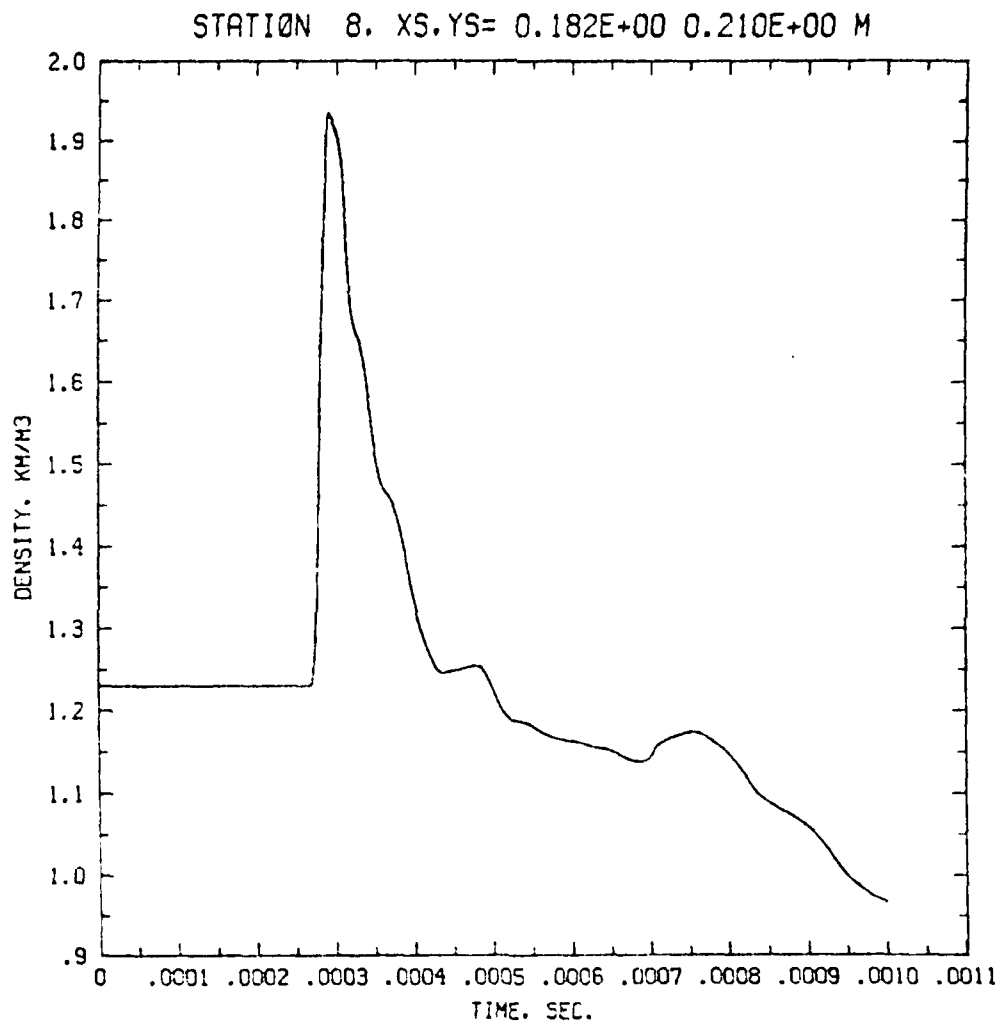
Figure 45c



105 MM HOWITZER MUZZLE FLOW

9 DUMPS. LAST DUMP IS MSH20009

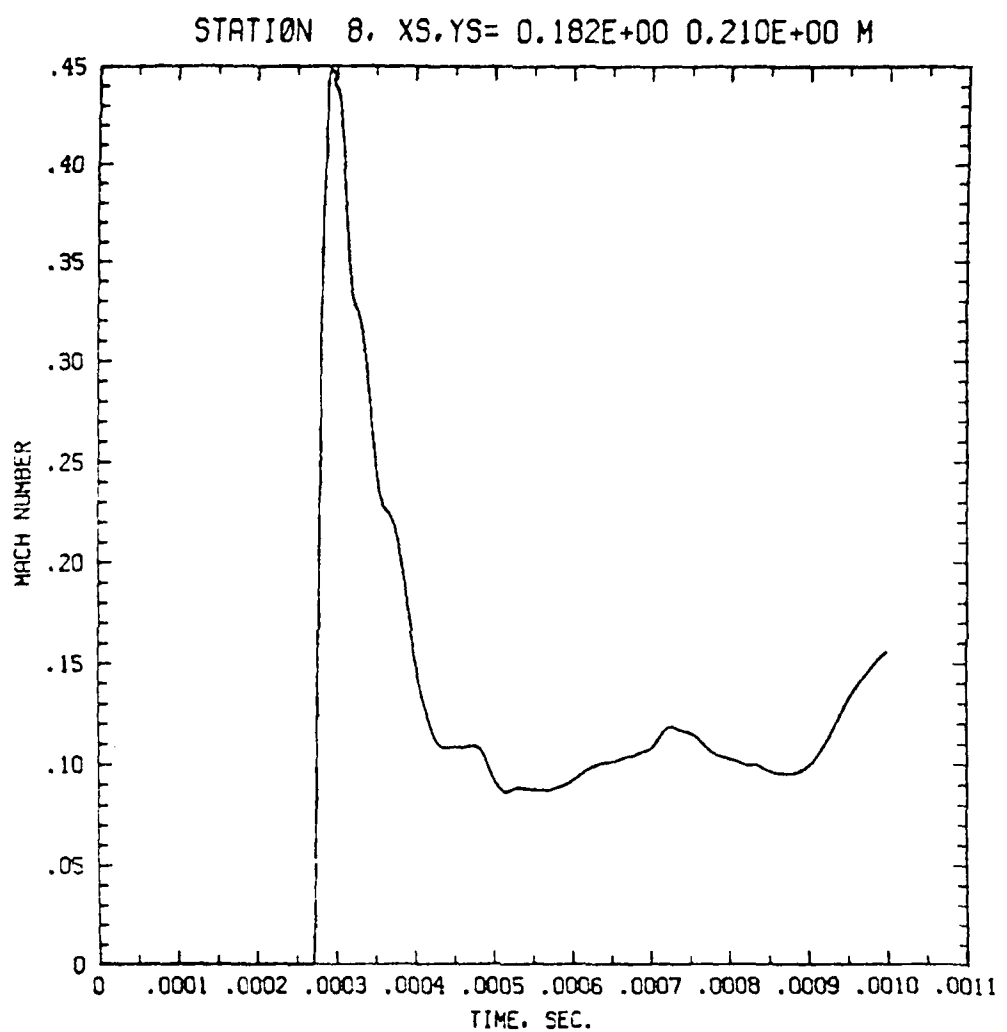
Figure 46a



105 MM HOWITZER MUZZLE FLOW

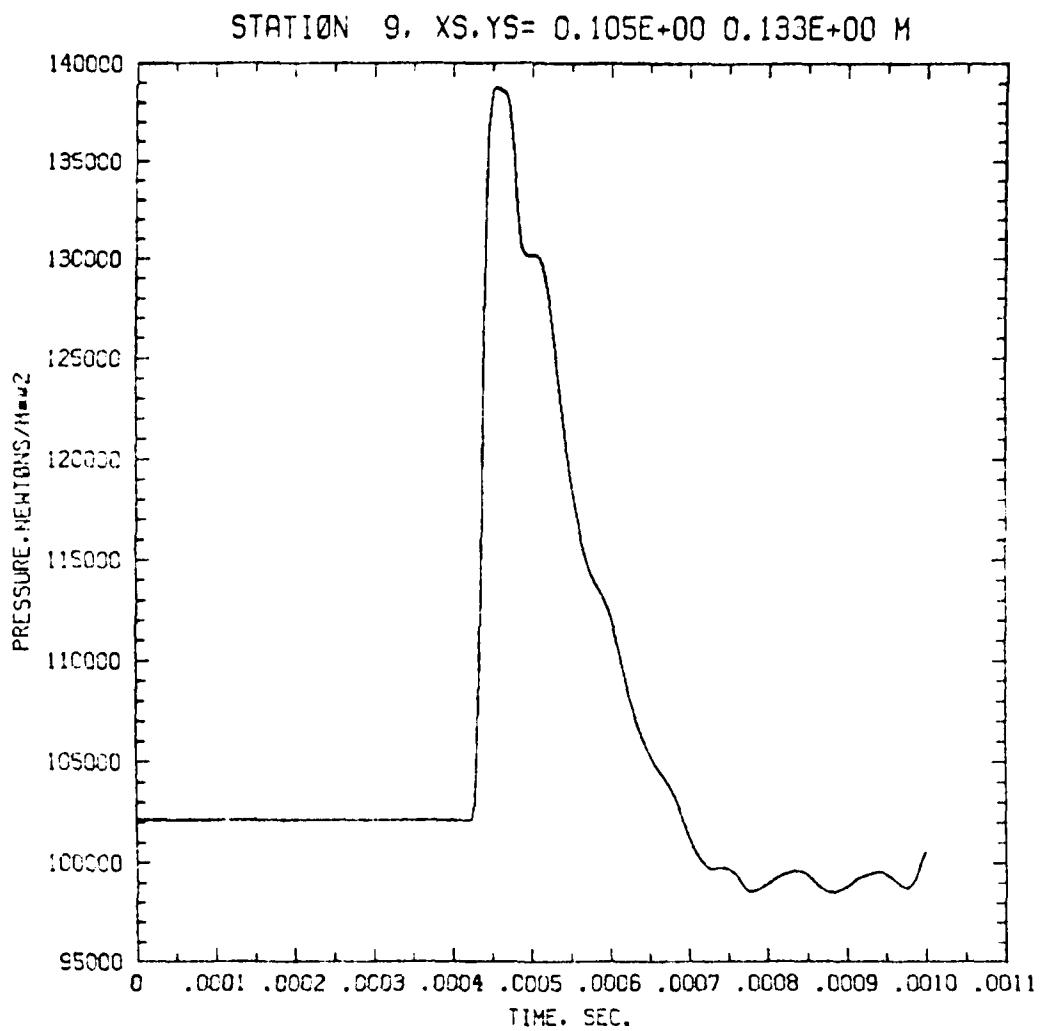
8 DUMPS. LAST DUMP IS NOWZ0000

Figure 46b



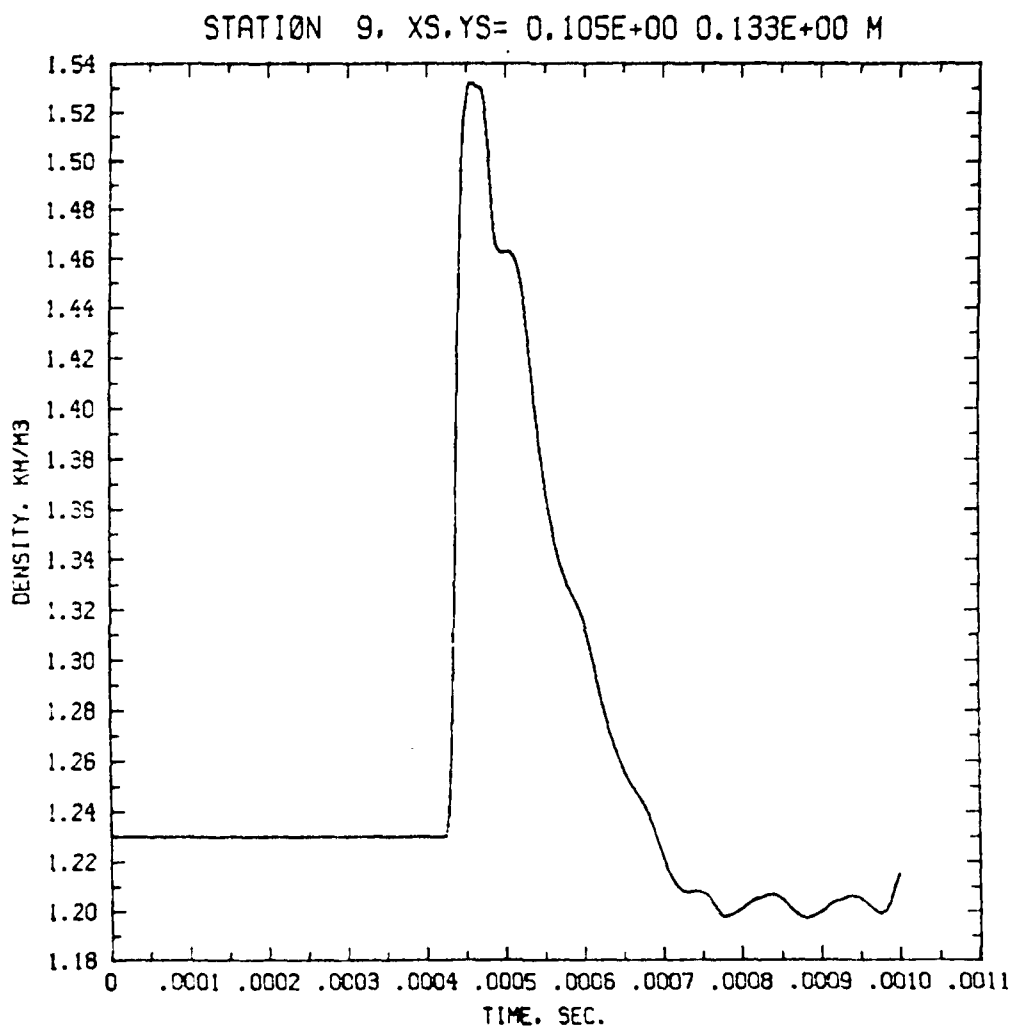
105 MM HOWITZER MUZZLE FLOW  
@ DUMPS. LAST DUMP IS NOWZ0009

Figure 46c



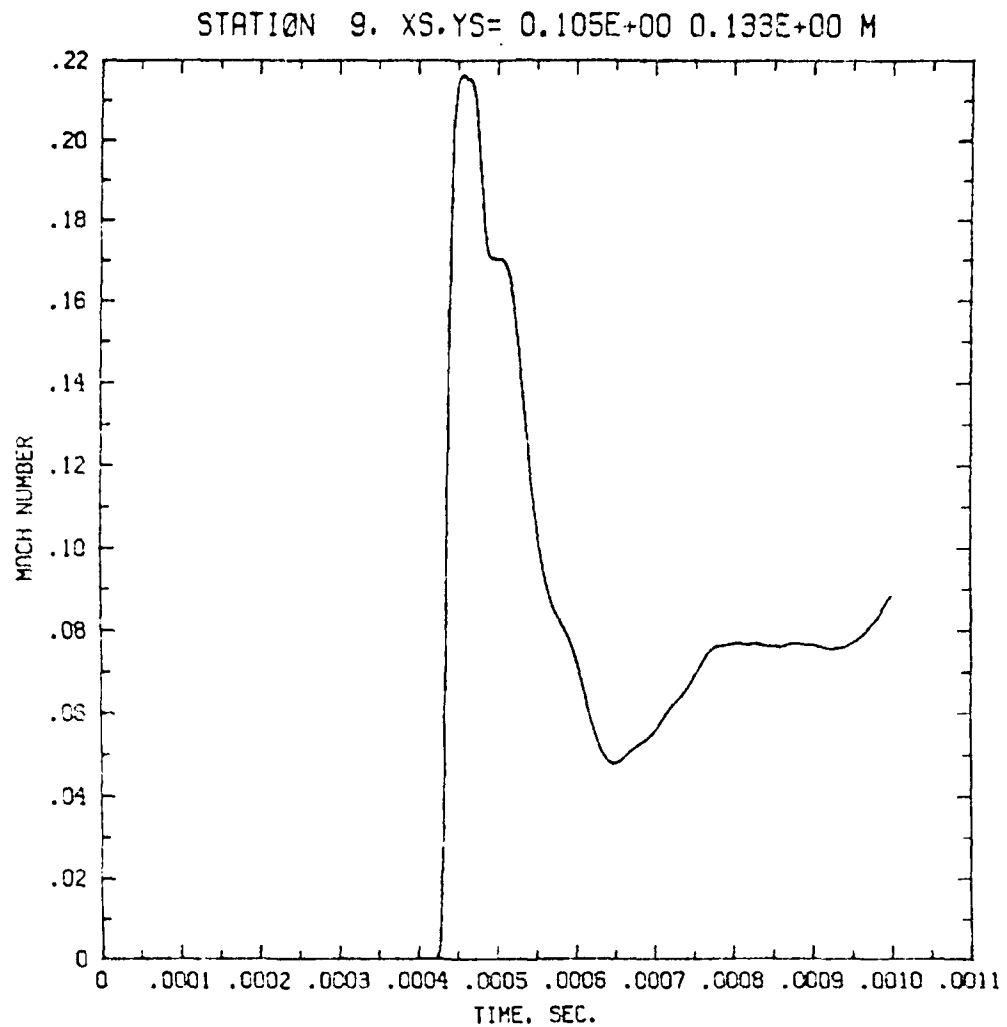
105 MM HOWITZER MUZZLE FLOW  
8 DUMPS. LAST DUMP IS NOWZ0009

Figure 47a



105 MM HOWITZER MUZZLE FLOW  
8 DUMPS. LAST DUMP IS 10000000

Figure 47b



105 MM HOWITZER MUZZLE FLOW

8 DUMPS. LAST DUMP IS HEX-ZERO

Figure 47c

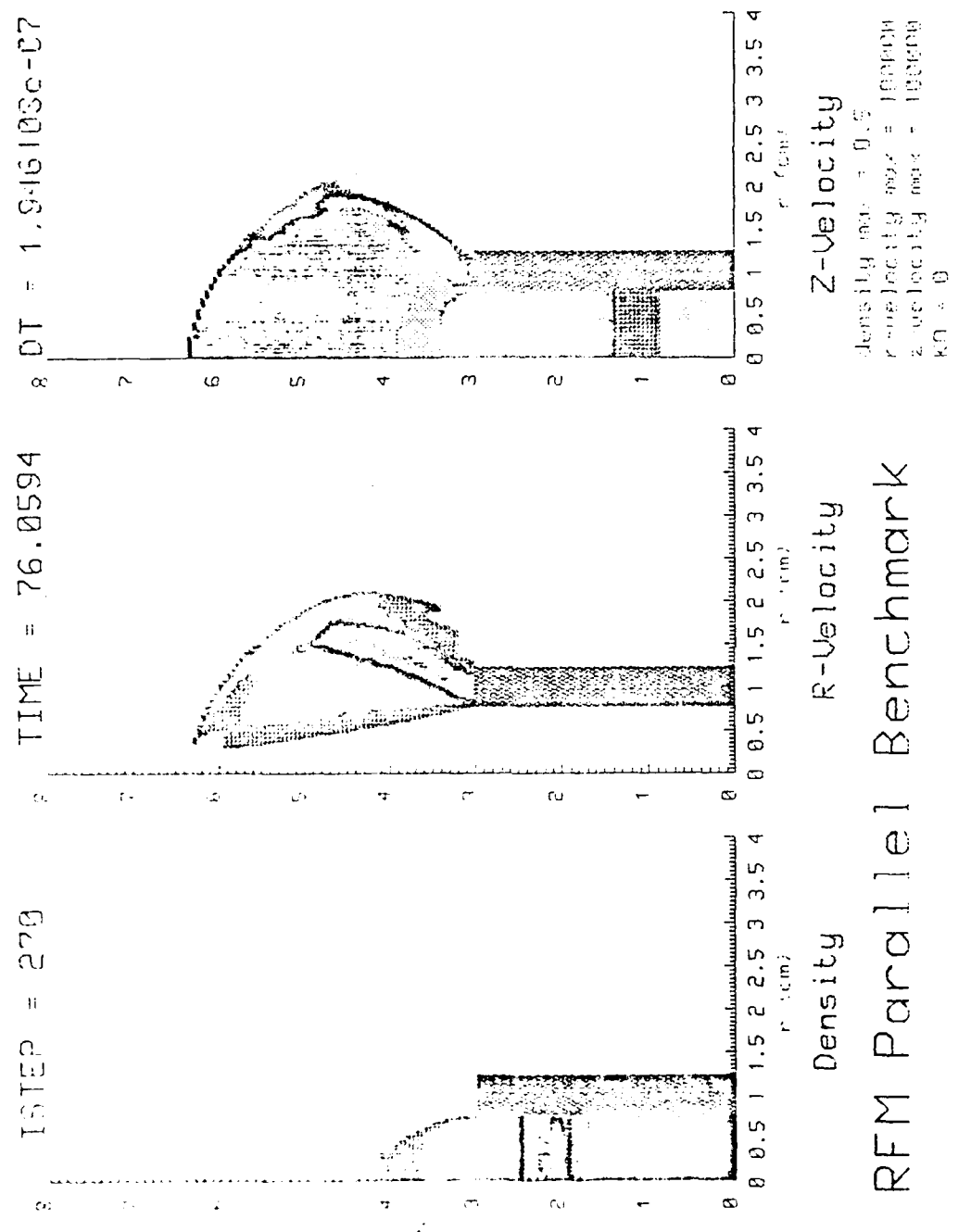


Figure 48

## RFM Parallel Benchmark

REFERENCES

1. Book, D.L., Boris, J.P., and Hain, K., "Flux-Corrected Transport: II. Generalizations of the Method," *J. Comp. Phys.* 18, 248 (1975).
2. Boris, J.P., "Flux-Corrected Transport Methods for Solving Generalized Continuity Equations," NRL Memo Report No. 3237 (1976). ADA023891
3. Boris, J.P., and Book, D.L., "Flux-Corrected Transport: I. SHASTA, A Fluid Transport Algorithm that Works," *J. Comp. Phys.*, 11, 38-69 (1973).
4. Boris, J.P., and Book, D.L. "Flux-Corrected Transport III. Minimal-Error FCT Algorithms," *J. Comp. Phys.* 20, 397-431 (1976).
5. Colella, P., and Woodward, P.R., *J. Comp. Phys.* 54, 174 (1984); see also Woodward, P.R., an Colella, P., "High Resolution Difference Schemes for Compressible Gas Dynamics" in Proc. Seventh Inter. Conf. Num. Methods in Fluid Dynamics, Springer-Verlag, New York (1981), p. 434.
6. Harten, A., *Math. Comput.* 32, 363 (1978).
7. Scammon, F.M., Specifications of Joint Computation of Weapon Blast Overpressures (personal communication Jan. 4, 1985).
8. Townsend, L.H., and Edwards, D.G., "Numerical Simulation of Blast," TICP 402, Dover, NJ, May 25, 1962.
9. Van Leer, B., *J. Comp. Phys.* 32, 101 (1979).
10. Zalesak, S.T., "Fully Multidimensional Flux-Corrected Transport Algorithms for Fluids," *J. Comp. Phys.* 31, 335-362 (1979).

**END**

**FILMED**

**2-86**

**DTIC**